

1 PRENOLIN: international benchmark on

2 1D nonlinear site response analysis –

3 Validation phase exercise

4 Julie Régnier*

5 Luis-Fabian Bonilla IFSTTAR, Paris, France

6 Pierre-Yves Bard IFSTTAR/ISterre, Paris-Grenoble, France

7 Etienne Bertrand, CEREMA, Nice, France

8 Fabrice Hollender, CEA, Cadarache, France

9 Hiroshi Kawase, DPRI, Kyoto, Japan

10 Deborah Sicilia, EDF, Aix-en-provence, France

11 Pedro Arduino, University of Washington, US

12 Angelo Amorosi, Sapienza University of Rome, Italy

13 Dominiki Asimaki, Caltech, Pasadena, US

14 Daniela Boldini, University of Bologna, Italy

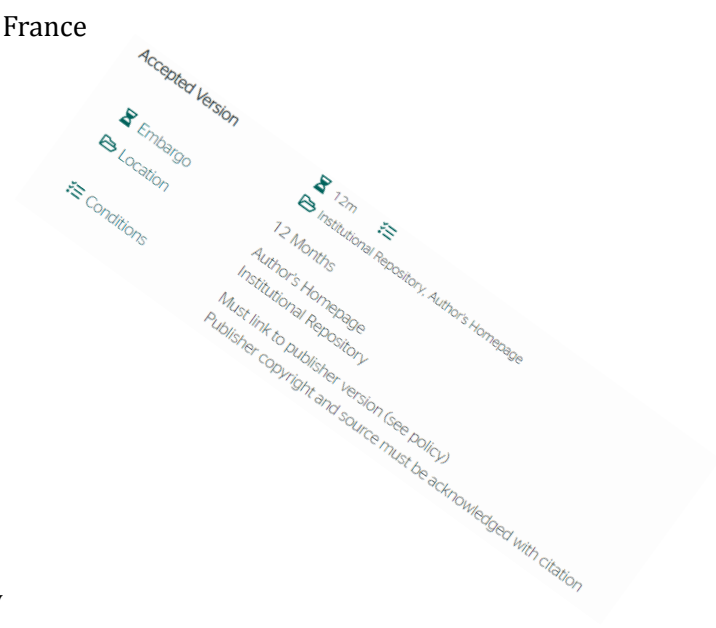
Accepted version

Licence

Please cite as:

Regnier J. et al. (2018). International benchmark 1D nonlinear site-response analysis validation phase exercise. *Bulletin of the Seismological Society of America*, 108(2): 876-900

<https://doi.org/10.1785/0120170210>



* *Julie.regnier@cerema.fr*; Cerema, Equipe-Projet MOUVGS, 500 routes des Lucioles, Sophia-Antipolis, F-06903, France

- 15 Long Chen, Univ. Washington, Seattle, US
- 16 Anna Chiaradonna, Univ. Napoli, Italy
- 17 Florent DeMartin, BRGM, Orléans, France
- 18 Ahmed Elgamal, UC, San Diego, La Jolla, CA, US
- 19 Gaetano Falcone, Politecnico of Bari, Italy
- 20 Evelyne Foerster, CEA, Saclay, France
- 21 Sebastiano Foti, Politecnico di Torino, Torino, Italy
- 22 Evangelia Garini, NTUA, Athena, Greece
- 23 George Gazetas, NTUA, Athena, Greece
- 24 Céline Gélis, IRSN, Fontenay-aux-roses, France
- 25 Alborz Ghofrani, Univ. Washington, Seattle, US
- 26 Amalia Giannakou, Fugro, Greece
- 27 Jim Gingery, Hayward Baker Inc, El Cajon,, US
- 28 Nathalie Glinsky, CEREMA, Nice, France
- 29 Joseph Harmon, Univ. Illinois at Urbana-Champaign, US
- 30 Youssef Hashash, Univ. Illinois at Urbana-Champaign, US
- 31 Susumu Iai, FLIP consortium, Kyoto
- 32 Steve Kramer, Univ. of Washington, US
- 33 Stavroula Kontoe, Imperial College, London, England

- 34 Jozef Kristek, CUB, Bratislava, Slovakia
- 35 Giuseppe Lanzo, Univ. Rome, Rome, Italy
- 36 Annamaria di Lernia, Politecnico of Bari, Italy
- 37 Fernando Lopez-Caballero, Centrale Supélec Paris, France
- 38 Marianne Marot, CEREMA, Nice, France
- 39 Graeme McAllister, University of British Columbia, Canada
- 40 E.Diego Mercerat, CEREMA, Nice, France
- 41 Peter Moczo, CUB, Bratislava, Slovakia
- 42 Silvana Montoya-Noguera, Centrale Supélec, France
- 43 Michael Musgrove, Univ. Illinois, US
- 44 Alex Nieto-Ferro, EDF Lab Paris Saclay, France
- 45 Alessandro Pagliaroli, CNR-IGAG, Rome, Italy
- 46 Federico Passeri, Politecnico di Torino, Torino, Italy
- 47 Aneta Richterova, CUB, Bratislava, Slovakia
- 48 Suwal Sajana, Univ. Rome, Rome, Italy
- 49 Maria Paola Santisi d'Avila, UNS, Nice, France
- 50 Jian Shi, Caltech, Pasadena, US
- 51 Francesco Silvestri, Univ. Napoli, Napoli, Italy
- 52 Mahdi Taiebat, University of British Columbia, Canada

- 53 Giuseppe Tropeano, Univ. Cagliari, Cagliari, Italy
- 54 Didrik Vandeputte, EDF, Aix-en-Provence, France
- 55 Luca Verrucci, Univ. Rome, Rome, Italy.*
- 56

* The author's list involves first the seven organizers of the PRENOLIN project followed by the participants in an alphabetic order.

57 **Abstract**

58 This article presents the main results of the validation phase of the PRENOLIN project.
59 PRENOLIN is an international benchmark on 1-D non-linear site response analysis. This
60 project involved 19 teams with 23 different codes tested. It was divided into two phases;
61 with the first phase verifying the numerical solution of these codes on idealized soil
62 profiles using simple signals and real seismic records. The second phase described in
63 this paper referred to code validation for the analysis of real instrumented sites.

64 This validation phase was performed on two sites (KSRH10 and Sendai) of the Japanese
65 strong-motion networks KiK-net and PARI, respectively, with a pair of accelerometers at
66 surface and depth. Extensive additional site characterizations were performed at both
67 sites involving in-situ and laboratory measurements of the soil properties. At each site,
68 sets of input motions were selected to represent different PGA and frequency content. It
69 was found that the code-to-code variability given by the standard deviation of the
70 computed surface response spectra is around 0.1 (in log₁₀ scale) regardless of the site
71 and input motions. This indicates a quite large influence of the numerical methods on
72 site effect assessment and more generally on seismic hazard. Besides, it was observed
73 that site-specific measurements are of primary importance for defining the input data in
74 site response analysis. The non-linear parameters obtain from the laboratory
75 measurements should be compared with curves coming from the literature. Finally, the
76 lessons learned from this exercise are synthetized, resulting also in a few
77 recommendations for future benchmarking studies, and the use of 1D NL, total stress
78 site response analysis.

79 **Introduction**

80 In seismology and earthquake engineering, site effects are widely recognized as an
81 important factor for (mainly) amplifying the resulting surface ground motion. Those site
82 effects are spatially variable depending on the local geomorphology and mechanical
83 properties of the soil; they may vary from one event to the other as the site response to
84 seismic loading is non-linear during strong ground motion (e.g. Amorosi et al., 2016;
85 Bonilla et al., 2005; Gunturi et al., 1998; Zeghal et al., 1995; Ishibashi and Zhang, 1993;
86 Yu et al., 1993; Elgamal et al., 1995; Vucetic and Dobry, 1991; Seed, 1969).

87 Site-specific analysis of the site response involving its non-linear soil behavior is still
88 very challenging. In low seismicity areas, the lack of strong ground motion recordings
89 limits empirical evaluations. To overcome this limitation, numerical simulations are of
90 primary interest since they allow for simulating strong ground motions beyond the
91 available recordings. In engineering practice, those analyses would, in most of the cases,
92 be limited to methods involving the use of linear or equivalent linear methods in a 1-D
93 site configuration.

94 As mentioned in the preceding companion paper (Régner et al., 2016a), previous
95 comparative tests were performed to study 1-D non-linear site response. The first blind
96 tests performed in the late 80's/early 90's, on the Ashigara Valley (Japan) and Turkey
97 Flat (California) sites were very instructive in the linear domain, because of the lack of
98 strong motion recordings at that time. The 2004 Parkfield earthquake, which produced
99 0.3 g at Turkey Flat site, was the opportunity to launch a new benchmarking exercise for
100 1D non-linear codes. This also considered a few other sites with vertical array data and
101 large enough ground motion (La Cienega, California; the KGWH02 KiK-net site, Japan;

102 and a site in Lotung, Taiwan). The results reported in Stewart et al. (2008), Kwok et al.
103 (2008), and Stewart and Kwok (2008, 2009) emphasized the importance of the needed
104 in-situ measurements and of the actual way these codes are used. The origin of the
105 significant mismatch between records and predictions has been attributed to incorrect
106 velocity profiles (despite the redundant borehole measurements), to deviations from 1D
107 geometry (non-horizontal soil layers), and deficiencies in the constitutive models
108 (unsatisfactory match to the actual degradation curves). The 1D codes used for these
109 tests remain, however, extensively used in routine engineering practice for site response
110 estimates, and various developments have been carried out to implement new, or
111 updated, constitutive models, It is therefore needed to repeat such benchmarking
112 activities, notably in other parts of the world which may have different engineering
113 practice, and which were not involved in the previous comparison exercises (which are
114 always good also for young scientists and engineers who never had such a benchmarking
115 experience).

116 The objective of this two-phase (verification and validation) PRENOLIN exercise is to
117 understand the variability associated to the implementation of the non-linear soil
118 behavior in numerical simulations, and to assess the resulting uncertainties. It was
119 decided to devote the calculations on simple cases focusing on the numerical
120 implementation of the non-linear soil behavior (rheology and soil parameters) to be as
121 close as possible to the standard engineering practice.

122 In this work we evaluate 1-D wave propagation of SH waves (only one component of
123 motion) having vertical incidence and assuming no pore pressure effects (total stress
124 analysis). These three assumptions mentioned above are not a sensitive issue when
125 dealing with the verification case (although realistic cases were selected to be close to

126 the true physical processes). However, when dealing with validation and comparison
127 with real data, they may have very strong impacts and for most sites and input motions
128 they might be violated to various degrees.

129 We choose our sites for the validation to minimize the impact of those assumptions.

130 The verification phase helped to create a synergy between the participants and the
131 organizing teams. We defined a common vocabulary for the implementation of the
132 calculations (as the Non-Linear (NL) communities from different areas of the world may
133 have different practice and a different understanding of the same words). By analyzing
134 the whole set of NL simulations, we found that the code-to-code variability increases
135 with the shear strain level. However, even in the worst case corresponding to large
136 loading and strain levels exceeding 1%, it remained lower than the single-station,
137 random variability of GMPE σ values for PGA. Given the scatter in the nonlinear results,
138 we thus concluded that a realistic analysis should use more than one constitutive model
139 to incorporate at least partially the epistemic uncertainty in site response computations.
140 It was also found that, in order to reduce the epistemic uncertainty, which is partially
141 accounted for by the code-to-code variability, one may need to precisely describe specific
142 input parameters, especially the soil shear strength profile. In addition, the variability
143 between code is considerably reduced when they all used the same loading and
144 unloading process (Masing rules or non-Masing rules, referred to as damping control
145 models) (Régnier et al., 2016a)

146 To keep this exercise relatively simple, it was decided from the beginning not to deal
147 with the problem of pore pressure effects (e.g. Elgamal et al., 1996; Zeghal et al., 1995).
148 We acknowledge that this hypothesis might not be realistic in saturated soils subjected

149 to strong-motion cyclic loads. One of the chosen PARI sites (Onahama) may have
150 experienced cyclic mobility during the Tohoku-Oki, Mw 9 March 11th, 2011 earthquake
151 (Roten et al., 2013). However, dealing with nonlinear site response increases the number
152 of soil parameters to consider, not only with respect to traditional linear estimates, but
153 also in relation to the complexity of the constitutive model used to describe the soil non-
154 linear behavior. Since soil nonlinear behavior, even in the absence of pore pressure
155 effects, remains a challenge, the main effort of the validation exercise was focused on
156 total stress analysis only, disregarding the simulation of excess pore pressure generation.
157 To verify effects of water pressure build-up on the recordings acceleration time history,
158 some teams used site response analyses with excess pore water pressure generation to
159 compare with the total stress cases and are shown in the electronic supplement (Figure
160 S6 and S7). The recommendations of this report are only for total stress site response
161 analyses.

162 A detailed presentation of the organization of the project and the participant teams was
163 done in the previous paper related to the verification phase (Régnier et al., 2016a). The
164 table of the participants with description of the methods is thus provided here only in
165 the electronic supplement (Table S1).

166 The objectives of this paper are to share the experiences on the validation exercise
167 concerning (i) the analysis of data from laboratory and in-situ tests data to define the
168 input soil parameters for the simulations, (ii) the processing and selection of the seismic
169 input motions, (iii) the calculations of the non-linear site response and finally (iv) to
170 quantify the epistemic uncertainty for 1-D nonlinear site response analysis on real sites,
171 both in terms of code-to-code variability and code-to-data distance.

172 **Target sites**

173 **Selection criteria**

174 The selection of sites was performed on strong-motion databases involving vertical
175 arrays so that the empirical soil column response (often called transfer function) can be
176 calculated. Considering the hypothesis of the numerical methods and the objective to
177 implement non-linear soil behavior, the sites were selected on the basis of the following
178 requirements:

179 (1) Availability of both strong and weak motion recordings,

180 (2) Plausibility of 1-D geometrical soil configuration, i.e. satisfactory agreement between
181 numerical and empirical site responses in the linear / weak-motion range,

182 (3) The depth of downhole sensor must be less than 300 m.

183 (4) the possibility to perform complementary investigations in the immediate proximity
184 of the site

185 To fulfill the first and second criteria, sites that recorded at least two earthquakes with
186 PGAs higher than 50 cm/s^2 at the downhole sensor were selected. Only the KiK-net site
187 configurations identified as fulfilling the 1D criteria proposed by Thompson et al. (2012)
188 and Régnier et al. (2014) were considered. In addition, a visual comparison between the
189 numerical and empirical site response curves was performed and a special attention was
190 given to the matching of fundamental resonance frequency.

191 The fourth criterion also constrained the site selection, as the nearby urbanization may
192 prevent the drilling of new boreholes or the ability to perform new surface
193 measurements.

194

195 **Dataset**

196 *Presentation*

197 The sites selection was done on the KiK-net and PARI (Port and Airport Research
198 Institute) networks. KiK-net is composed of 688 stations, with high-quality surface and
199 downhole digital 3-component accelerometers. Among the KiK-net sites, 668 are
200 characterized with shear and compressive wave-velocity profiles. These velocity profiles
201 were obtained from downhole or PS logging measurements (depending on the site).
202 Most of the borehole sensors are located between 100 m and 200 m depth. Two thirds of
203 the sites have a $V_{s30} < 550$ m/s. In the NEHRP and Eurocode 8 regulation, sites with
204 $V_{s30} < 800$ m/s are classified as sites prone to site effects, which confirms that the KiK-
205 net database is very interesting for the analysis of these phenomena. The PARI sites are
206 much shallower than the KiK-net sites: the down-hole sensor depth is around 10 m and
207 the corresponding V_s profile is also available.

208 *Data processing*

209 More than 46,000 (six component) recordings were analyzed beforehand (Régnier et al.,
210 2013) to derive the empirical site response (i.e., the transfer function from downhole to
211 surface) at the 688 sites. In addition, on 668 sites with available V_s profiles, the
212 numerical linear site response was also calculated on the basis of the velocity profile
213 provided in the KiK-net data base (see Data and resource section). On the PARI network,
214 only two sites were analyzed: Sendai (30 earthquake recordings), and Onahama (42
215 earthquake recordings).

216 The empirical site response is usually evaluated by using a spectral ratio between
217 simultaneous recordings on sediments and on a nearby rock site (the so-called reference

218 site). When this technique is applied, the main issue to overcome is the selection of a
219 reliable reference site. The reference site should not amplify seismic waves, and should
220 be close enough to the studied site so that the travel path from the seismic source
221 remains equivalent for both sites.

222 Vertical arrays of accelerometers overcome the reference-site issue. Indeed, the down-
223 hole station located at depth represents the reference station. Thus, for each KiK-net
224 (and PARI) sites and each earthquake recording, the Borehole Fourier Spectral Ratio
225 (*BFSR*) were calculated. *BFSR* is the ratio between the Fourier spectra of the horizontal
226 components recorded at the surface and the corresponding ones at depth. Yet we
227 acknowledge that the use of downhole records introduces an additional difficulty in
228 numerical modeling due to the contamination of the control motion by the downgoing
229 wavefield, which is sensitive both to the details of velocity and damping soil profile, and
230 to the complexity of the incoming wavefield (various types of body waves with multiple
231 incidence angles, together with possibility of surface waves, see Bonilla et al., 2002;
232 Régnier et al., 2014).

233 Before evaluating the *BFSR* a specific data processing procedure was applied that
234 consisted in removing the mean, applying a tapering Hanning window on 2% of the
235 signal, non-causal filtering between 0.1 and 40 Hz, FFT calculation and a Konno-Omachi
236 smoothing (with $b = 40$) before performing the surface to down-hole spectral ratio. The
237 linear site response was obtained by calculating the geometric average of all recordings
238 with a PGA at the surface below 25 cm/s^2 .

239 The empirical site response curves were compared to the equivalent numerical ones
240 (*BFSR_{num}*). The numerical site responses (*BFSR_{num}* and *OFSR_{num}*, indicating respectively

241 the transfer functions having the reference at the down-hole and at the rock outcrop,
242 respectively) were computed using a Haskell-Thomson 1-D linear method (Haskell,
243 1953; Thomson, 1950). For the calculation of the transfer function, we also added a
244 Konno-Ohmachi smoothing ($b = 40$) that was applied directly to the transfer function
245 curve (since it is the direct result from the Haskell-Thomson method) and the same
246 frequency sampling as the one dealing with the analysis of earthquake recordings was
247 used.

248 The soil parameters that are required to compute the numerical transfer functions are
249 the shear wave velocity profile V_s , the density profile and the quality factor profile. In the
250 KiK-net (and PARI) database, only the V_s profiles are available. For the density, a
251 constant value along the profile equal to 2000 Kg/m^3 was used. The quality factor (Q)
252 was directly derived from the V_s value following the rule of thumb scaling : $Q = V_s/10$
253 (Olsen et al., 2003) used by many authors when no measurement is available from
254 laboratory data measurements (see section "*From in-situ and lab data to input*
255 *parameters*"). Others models for the low strain attenuation could have been used as well
256 such as proposed in (Darendeli, 2001; Menq, 2003).

257 **Selected sites**

258 5 KiK-net sites (FKSH14, IBRH13, IWTH04, KSRH10 and NIGH13) passed the selection
259 criteria, together with the 2 PARI sites that were initially chosen. Four KiK-net sites were
260 removed for various reasons: liquefaction susceptibility (FKSH14), rocky geology
261 (IBRH13), mountainous environment (IWTH04) and insufficient nonlinearity (NIGH13).
262 A detailed study on the effects of the topography and non-horizontal layering on
263 waveforms and transfer functions of KiK-net sites can be found in De Martin et al., (
264 2013).

265 The three remaining sites, i.e., KSRH10, Onahama and Sendai sites were therefore
266 selected for further in-situ investigations for the purpose of the validation phase. Later
267 on, for the Onahama site, it was found that the soil was susceptible to liquefaction (Roten
268 et al., 2013) and clearly show 2D/3D site configuration. Consequently, the calculations
269 performed on this site will not be presented in the present paper, although they were
270 part of the validation phase.

271 The locations of KSRH10 (Hokkaido region) and Sendai (Tohoku region) are illustrated
272 in Figure 1.

273 *Figure 1*

274 According to the initial available geotechnical data, KSRH10 is mainly composed of
275 clayey soil while Sendai site is composed of sandy soil. KSRH10 site is a deep
276 sedimentary site with 40m of low velocity soil layers; the down-hole sensor is located at
277 a depth of 255m (plot (a) of Figure 2). The site is located on the lower plateaus with
278 about 30m in elevation along the right bank (southern) side of the upper Anebetsu River.
279 The soil column consists of recent Younger Volcanic Ash deposits until 5m at depth,
280 followed by volcanic and Tuffaceous sand until 40m and underlie by an alternation of
281 sandstone and shale.

282 The Sendai site is a shallow site with 7 m of soft soil deposits and with the down-hole
283 sensor located at 10.4m at depth. According to the Shogama 1:50 000 geological map,
284 the site is in a large flat valley covered by beach ridge deposits (Holocene) consisting of
285 gravel and sand. These surface deposits are underlain by the Pliocene, Geba Formation,
286 forming the northern and eastern hills and consist of gravel stone, sandstone, tuff,
287 tuffaceous siltstone, and lignite.

288 As illustrated in Figure 2 (plots b and e), empirical weak motion BFSR (surface PGA
289 lower than 25 cm/s²) and the linear numerical 1-D site response (dotted black line)
290 exhibit a satisfactory similarity, especially for Sendai site. The shallow Sendai site is
291 characterized by a high resonance frequency around 8.2 Hz, while the thicker KSRH10
292 site is characterized by a lower fundamental resonance frequency of 1.7 Hz; slight
293 differences can be seen however between observations and simulations as to the
294 frequencies of the first two peaks. The numerical simulations (dotted lines) provide site
295 response amplitude much higher at the first two frequency peaks and above 15Hz while
296 it is lower for the third and fourth peaks. This first comparison shows that the sites are
297 close to a 1-D site configuration, but exhibit a more complex behavior than those
298 predicted for a simple soil column subjected to pure vertically incident plane S waves.

299 When the sites were selected for the validation, one of the requirements was that the
300 sites exhibit some non-linear soil behavior for one or several recordings. In Figure 2
301 (plots c and f) the BFSR for weak motion is compared to the BFSR calculated from
302 motions with large PGA at the surface. For KSRH10, non-linear soil behavior is
303 significant for the input motions with PGA greater than 47 cm/s² at the down-hole
304 station (outside the average \pm standard deviation area) and it is even greater for the
305 strongest events (KSRH100411290332 with PGA equal to 81 cm/s² and
306 KSRH100309260450 with PGA equal to 110 cm/s² – table 1). For Sendai, non-linear soil
307 behavior is significant when the downhole PGA exceeds 46 cm/s² (outside the average \pm
308 standard deviation area) and it is even greater for the strongest event (F-2958 with PGA
309 equal to 252 cm/s²).

310

Figure 2

311 **Selection of the input motions**

312 A selection of 10 and 9 input motions for KSRH10 and Sendai, respectively was
313 performed among the available earthquake recordings. Their epicenters, magnitudes
314 and peak accelerations at the surface are illustrated in Figure 1 and provided in table 1.
315 The site response computations were performed on 5 input motions at KSRH10 (TS-0-K,
316 TS-1-K, TS-2-K, TS-4-K and TS-9-K) and 4 at Sendai (TS-1-S, TS-2-S, TS-5-S and TS-8-S),
317 numbered from strongest to weakest. Only the results of these input motions are shown
318 in this article. Nevertheless, we provide the information for all available input motions as
319 they may be used for future validation exercises.

320 The PGA and the frequency content of a recording are two relevant parameters of the
321 input motion for describing the expected degree of non-linear soil behavior (Assimaki
322 and Li, 2012; Régnier et al., 2016b). The input motions for KSRH10 and Sendai sites
323 were selected with 3 different PGA levels (at the downhole sensor), respectively. The
324 PGA was calculated on the acceleration time histories of the geometrical mean of the EW
325 and NS components, filtered between 0.1 and 40 Hz. In each group of PGA level, we
326 quantified the frequency content using the central frequency following Eq 1 (statistical
327 moments order 2 and 0, Sato et al., 1996) but the values were not significantly variable
328 from one event to another. We therefore also considered several magnitudes and
329 epicentral distances couples.

330

$$F_c = \sqrt{\frac{\int f^2 A^2(f) df}{\int A^2(f) df}}$$

331

Eq 1

332 where F_c is the central frequency, f the frequency, $A(f)$ the amplitude of the Fourier
333 Spectrum of the accelerogram. The resulting values exhibit a significant but rather
334 erratic variability, without obvious link to magnitude, epicentral distance or depth. We
335 therefore also considered several magnitudes and epicentral distances couples.

336 The selected events for the KSRH10 and Sendai sites are listed in the Table 1 along with
337 their main characteristics (Mw, depth, epicentral distance, PGA at the down-hole and at
338 the surface, and central frequency at the down-hole recording). The frequency sampling
339 at KiK-net is between 100 and 200 Hz depending on the event and at Sendai it is 100 Hz.
340 For KSRH10, four input motions with PGA at the down-hole sensor higher than 50 cm/s²
341 were available and selected, whereas only 3 were available in Sendai site.

342

Table 1

343 **Signal to noise ratio**

344 We checked the quality of all events by assuring that their signal-to-noise ratios were
345 high enough ($S/N > 3$) over a broad frequency spectrum of 0.1 to 50 Hz, for all three
346 components.

347 **Orientation of the surface to down-hole sensors**

348 We checked that both surface and down-hole sensors are oriented in a similar way. We
349 rotated anti-clockwise the surface horizontal components with a 1° azimuth increment,
350 starting from the original EW orientation, and we calculated the correlation coefficient

351 with the down-hole EW component. Both signals were filtered between 0.1 and 1 Hz.
352 The angle characterized by the maximum correlation would approximately correspond
353 to the angle between the two EW components of the surface and the down-hole sensors.
354 Correlations are maximum without rotation angles at Sendai and at KSRH10. It is close
355 to the calculations performed by D. Kosaka (PARI) who found a deviation of 7.2°
356 counterclockwise at Sendai also using long period motions correlations. Results are
357 approximately similar to the results of Maeda et al. (2005) who found a deviation of 2.2°
358 clockwise at KSRH10. These values suggest that both surface and down-hole EW-
359 components are mostly oriented parallel one to each other, and even if slight deviations
360 of the order of 7° may occur, it would not impact significantly the soil response functions.

361 **Verification of the verticality of the incident waves**

362 Basic assumptions are made in most 1D simulation codes when propagating a wave
363 through a soil column. One of them is that the wavefield consists of vertically
364 propagating plane S waves; hence the input wave motion at the bottom of the soil
365 column is fully represented by the horizontal components and all vertically propagated
366 towards the surface. However, except for teleseismic (long-distance) events, the seismic
367 waves from local or regional events are very likely to have not only non-vertical
368 incidence (unless located directly underneath the sensor), but also multiple incidence
369 because of crustal scattering

370 Recording a non-vertical incident wavefield implies that the total seismic energy is
371 distributed all over the three components. Therefore, if only one component of the 3D
372 wavefield is used to represent one type of seismic phase (in our case, the shear wave),
373 then it is highly likely that the wave energy, PGA and strains are underestimated at the
374 down-hole sensor. However, depending on the thickness of the soil column and its

375 characteristics, the upward propagating body waves become increasingly vertical
376 towards the surface and therefore the surface sensor will give a more complete
377 representation of the entire shear wave energy on the horizontal components.
378 Therefore, two consequences can result from this observation:

379 (1) Although both the numerical and empirical input motions are the same, their
380 transfer functions would be different, since the energy on the horizontal components
381 at the surface will be greater in the empirical observation at KSRH10 than the
382 numerical simulations.

383 (2) The actual seismic loading at the base of the soil column is underestimated
384 compared to what the soil experiences, and therefore its possible non-linear
385 behavior can also be underestimated.

386 To determine the direction of propagation of an input motion, we used a polarization
387 analysis based on the 3-component covariance matrix. In the electronic supplement
388 (figure S1) we can see that at KSRH10, the polarization analysis indicates that the waves
389 mostly propagate with a vertical incidence (low incidence angle). At Sendai, except for
390 two recordings, the waves are not linearly polarized; therefore, the calculations of the
391 direction of propagations are not relevant.

392 **From in-situ and laboratory data to input parameters**

393 Identifying the most relevant parameters to be used for simulating the non-linear wave
394 propagation process in a soil deposit was one of the main challenges tackled during the
395 verification exercise. For the elastic and visco-elastic properties, V_s , V_p , density and low
396 strain attenuation profiles were used. For the non-linear soil properties, the modulus

397 reduction and damping with shear strain curves, with the soil shear strength profile
398 were found to be the key parameters to significantly reduce the code to code site
399 response variability (Régnier et al., 2016). For more complicated non-linear models such
400 as Hujoux (Aubry et al., 1982), more more laboratory measurements are required to
401 define its model parameters, however some of this parameters could be defined using
402 well known soil mechanics correlations.

403 The challenge for the validation phase was to determine the value of those parameters
404 for a real site. The specifications for the laboratory and in-situ measurements were
405 defined in accordance with the prescriptions coming from the organization team with a
406 few associated geotechnical experts and the participating teams, and bounded by the
407 available budget and the measurement capacity of the local company performing the
408 measurements, together with a few logistical issues linked with the exact location of the
409 vertical array and the surrounding environment.

410 **Site investigation**

411 *Measurements performed*

412 To obtain the linear and non-linear soil parameters, in-situ measurements and multiple
413 laboratory measurements were conducted on disturbed and undisturbed soil samples.

414 The in-situ measurements were subcontracted to Oyo company and consisted in: (1)
415 boring investigation to determine soil stratigraphy and to perform the soil sampling. The
416 diameter of the borehole was 116 mm up to a depth where tripled-tube samplings were
417 used (for sandy soil or relatively stiff clayey soil) then 86 mm; (2) Undisturbed soil
418 samples (80 cm long) were collected using the thin-wall sampler for the soft clay soil
419 and using the tripled-tube samplers for the sand and stiffer clayey soil; (3) Standard

420 Penetration Tests (SPT); (4) PS logging by suspension method for KSRH10 and down-
421 hole method for Sendai, and (5) multiple MASW (Multichannel Analysis of surface
422 Waves) at the investigated sites to characterize the spatial variability of the underground
423 structure at shallow depth, together with single point ambient vibrations recordings.
424 The laboratory soil tests were conducted on disturbed and undisturbed soil samples.
425 The tests on disturbed samples enable to determine physical characteristics such as
426 particle size distribution, liquid and Atterberg limits. The tests on undisturbed soil
427 samples aim at defining the density and to perform a wide range of laboratory tests such
428 as Undrained and drained tri-axial compressional test, oedometer tests by incremental
429 loading, cyclic undrained and drained tri-axial compression test (undrained for
430 investigating the liquefaction potential) and, for rock samples, unconfined
431 compressional tests. The methods used to perform the laboratory tests are defined by
432 Japanese normative specifications.

433 For each borehole, the number of undisturbed soil samples was defined according to the
434 expected soil stratigraphy (on the basis of pre-existing KiK-net or PARI information), to
435 ensure at least one sample in each homogeneous soil unit.

436 The number and location of soil samples are specified in Table 2 together with the
437 down-hole sensor depth and the maximum depth of the complementary drillings. The
438 details of the locations of the laboratory measurements are available in the electronic
439 supplement (Figure S2 to S5). Figure 3 shows the locations of the boreholes having the
440 accelerometers with respect to the boreholes performed for the laboratory
441 measurements and the MASW lines.

442 *Figure 3*

443 *Table 2*

444 *Uncertainties of soil parameter measurements*

445 Because of the inherent variability of the soil and the systems errors in the
446 measurements and sampling methods, a non-negligible level of uncertainty remains in
447 the soil parameters measured through the laboratory tests. Repeatability of the soil
448 samples and laboratory measurements are a possible way to ensure a reliable definition
449 of the soil parameters. This approach was not applied in this exercise due to budget
450 constraints. We therefore carefully analyzed the data and compared with literature data
451 for similar types of soil.

452 To minimize the impact of soil spatial variability, the new boreholes were performed as
453 close as possible to the instrumented ones. MASW lines performed between the two
454 boreholes indicate a low spatial variability of the soil parameters for KSRH10 and Sendai
455 (while they did indicate a significant variability at shallow depth for the third site in
456 Onahama, which was also one of the reasons to drop this site for the validation exercise).

457 **Interpretation of the laboratory and in-situ data**

458 *Elastic and visco-elastic properties*

459 For the elastic properties, several methods were used to determine the soil parameters.
460 We have preferred the methods that provide the direct in-situ evaluation of the soil
461 properties, yet we did compare the results with alternative techniques characterized by
462 indirect measurements. We used the PS logging to obtain the V_s profile and then we use
463 the earthquake recordings to adjust it. As shown in Figure 4, the V_s profile was adjusted

464 to improve the fit between the fundamental resonance frequency recorded and
465 predicted for the KSRH10 and Sendai sites.

466 For KSRH10, the initial V_s profile was based on the PS logging investigation down to 50
467 m depth; beyond this depth, we considered the values of the V_s coming from the KiK-net
468 database, where PS-logging method was used as well. In this project, it was decided to
469 adjust the linear transfer function from Thomson-Haskell predictions to the
470 instrumental observations of surface-borehole spectral ratios, to ensure that the
471 discrepancies between the prediction and the observations during the benchmark were
472 associated to non-linear soil behavior, and not to other causes.

473 To adjust the numerical linear transfer function to the observation, we modify mostly the
474 V_s profile coming from KiK-net for which no information was available on the
475 measurement.

476 For Sendai, to improve the fit between the weak motion site response calculated with
477 linear site response analysis and computed from weak motions, a gradient type V_s
478 profile (Eq 2) was chosen.

479
$$V_s = V_{s_1} + (V_{s_2} - V_{s_1}) \left[\frac{z - Z_1}{Z_2 - Z_1} \right]^\alpha$$

480 *Eq 2*

481 Where, $V_{s_1} = 140$ m/s, $V_{s_2} = 460$ m/s and $\alpha=0.7$, Z_1 is the depth at which begin the
482 gradient (0 m) and Z_2 (7 m) the depth where it finishes.

483 The Poisson coefficient (ν) was computed using the PS logging and rounded. To ensure
484 consistency between the values of V_s , V_p and ν , the V_p parameter was obtained from V_s
485 and the rounded ν . The density was obtained from the undisturbed soil sample and the

486 low strain attenuation was deduced from the un-drained cyclic tri-axial test, and when
487 not available by using the rule-of-thumb ($Q_s = V_s/10$) (Olsen et al., 2003).

488 *Figure 4*

489 *Non-linear soil properties*

490 The initial plan was to use only the measured non-linear parameters, i.e., the
491 degradation curves measured in the lab. It had however to be modified to ensure a
492 better fit to the strong motion data: the non-linear soil properties were actually updated
493 during the iterations of calculations, so that three sets of non-linear soil parameters
494 were used. The first one (called SC1) came simply from the use of non-linear
495 degradation parameters defined in the literature, and anchored to elastic soil properties.
496 Here the Darendeli formulation was adopted (Darendeli, 2001). The second (SC2) and
497 third (SC3) soil parameter sets are directly based on interpretations of the laboratory
498 data. One objective of the benchmark was to focus on routine practice with relatively
499 simple models. Furthermore, the participants were also free to build/use their own soil
500 model based on the raw experimental laboratory test. Yet, additional non-linear soil
501 parameters could have been tested as well, such as models that could handle both low
502 and high strain as detailed in Groholski et al. (2016) and Yee et al. (2013).

503 Darendeli formulation (Darendeli, 2001) was used to define the G/G_{\max} and damping
504 ratio curves as a function of shear strain for SC1 soil column. To compute such values,
505 the knowledge of the confining effective stress (σ'), the over consolidation ratio (OCR),
506 the plasticity index (PI) and the damping ratio at low strains (D_{min}) was required.

507 The SC2 non-linear curves were constructed from the cyclic tri-axial compression test
508 results. We normalized the Young's modulus decay curves (from the lab 5th cycle of

509 loading) by the low strain Young's modulus (E_0). E_0 is the value of the hyperbolic model
510 (Hardin and Drnevich, 1972) that mimics the lab results at 0.0001%. We assimilate this
511 E/E_0 decay curve to the shear modulus G/G_{max} decay curve, with G_{max} associated to the
512 in-situ velocity measurements, i.e., $G_{max} = \rho V_s^2$. The shear strain used, γ , was considered
513 equal to 3/2 of the axial strain directly measured during the triaxial test. Indeed, the
514 shear strain is the difference between the axial and radial strain $\gamma = \varepsilon_a - \varepsilon_r$. During the
515 cyclic triaxial test under undrained conditions volumetric changes are zero: therefore,
516 the volumetric strain is null $\varepsilon_v = \varepsilon_a + 2\varepsilon_r = 0$. From the previous two equations we can
517 deduce that: $\gamma = 3/2\varepsilon_a$ (Vucetic and Dobry, 1988).

518 The elastic shear modulus values from the laboratory tests (G_{max}^{lab}) are generally under-
519 estimated compared to the in-situ measurements (G_{max}^{insitu}), especially for cyclic tri-axial
520 tests (indeed cyclic tri-axial tests are not reliable at low strain, below 10^{-4} %). Tatsuoka
521 et al. (1995) showed that this could be due to sample disturbance where stronger
522 differences are observed depending on the type of shear strain measurement. When
523 local measurements of shear strain are performed using internal gauges (inside the soil
524 sample) compared to external measurements (usual measurement), the discrepancies
525 are much smaller.

526 When normalizing the shear modulus curve to obtain the G/G_{max}^{lab} curve, the G_{max}^{lab}
527 should be corrected. The coefficient of correction to be applied is not well defined but
528 lies between 1.2 and 4 (Lopez-Caballero personal communication, 2015). A correction
529 procedure was set up in this study to partially correct this value (Noguera, 2016). The
530 procedure accounts for the measurements errors when using external measurements
531 instead of local ones but does not consider error due to soil sample disturbance.
532 Considering that this procedure was defined during the project (after the calculations on

533 Sendai site) it was only applied to the laboratory data for KSRH10 site.

534 The above-mentioned procedure consists in three steps: (1) to find the maximum shear
535 modulus (G_{max}^{lab}) by fitting the logarithmic equation (Eq 3) proposed by (Nakagawa and
536 Soga, 1995) as measured for intermediate strain values; (2) to compare the G_{max}^{lab} values
537 found with those from other tests or in the literature. Note that this value should not be
538 more than twice the G_{max}^{lab} as it only accounts for the external-to-local strain
539 measurement error; (3) to normalize the fitted decay curve and multiply it by G_{max}^{insitu}
540 value.

$$G/G_{max}(\gamma) = \frac{1}{1 + \alpha|\gamma|^\beta}$$

541

Eq 3

542

543 The SC3 model was built using the hyperbolic model (Eq 4 and Eq 5) constrained by the
544 G_{max}^{insitu} and the shear strength (τ_{max}). The latter was estimated from the depth and the
545 cohesion and friction properties according to Eq 6. This formula was derived from the
546 Mohr circle for simple shear test (Hardin and Drnevich, 1972). The shear strength used
547 here is the maximum shear stress not the maximum lateral shear stress, with the
548 effective cohesion (c') and the friction angle (φ') coming from the monotonic
549 compressional test and the coefficient of soil at rest (K_0) coming from Jaky's formula ($1 -$
550 $\sin(\varphi')$, Jaky, 1944).

551

$$G/G_{max}(\gamma) = \frac{1}{1 + \gamma/\gamma_{ref}}$$

Eq 4

552
$$\gamma_{ref} = \frac{\tau_{max}}{G_{max}}$$

Eq 5

553
$$\tau_{max} = \frac{(1+K_0)\sigma'_0 \sin \varphi'}{2} + c' \cos \varphi'$$

554 Eq 6

555 The comparison of the non-linear curves is illustrated in Figure 5 and Figure 6 for
556 KSRH10 and Sendai, respectively. For both sites, the SC1 non-linear curves have
557 generally more shear modulus reduction for the same shear strain than those coming
558 from the laboratory data, even after the correction procedure was applied.

559 The mechanical properties of the KSRH10 and Sendai sites are synthesized in *Table 3*

560 *Table 4*

561 and *Table 4*, respectively. For KSRH10, three sets of non-linear parameters were tested,
562 whereas only the first two were tested on Sendai site. From in-situ surveys, the water
563 table is located respectively at 2.4 m and 1.45 m below the ground surface for KSRH10
564 and Sendai site.

565 *Table 3*

566 *Table 4*

567 *Figure 5*

568 *Figure 6*

569 **Validation results**

570 **Calculations performed**

571 Two iterations of calculations were performed at KSRH10 and Sendai sites. The first
572 iteration was completely blind (i.e. only input motions were given to the participants)
573 while during the second one the surface motions were also provided. Three soil column
574 models were tested for KSRH10 and two for Sendai. Both EW and NS components were
575 used. In addition, the rotated horizontal motion corresponding to the maximum peak
576 acceleration was considered; simulations using this rotated horizontal component were
577 performed. However, the results were not significantly different from those obtained
578 using the EW or NS components. Thus, these computations are not shown here.

579 All the participating teams were asked to provide the acceleration time histories and the
580 stress-strain curves at different depths in the soil columns. For KSRH10, the acceleration
581 time histories were computed at various ground levels from the surface (GL): 0, -6, -11,
582 -15, -20, -24, -28, -25, -39, -44, -84 and -255 m depth, corresponding to the main soil
583 layers interfaces. The stress-strain curves were computed at GL-3, -8.5, -13, -17.5, -22, -
584 26, -31.5, -37, -41.5, -64 and -169.5 m, which correspond to the middle of the soil layers.
585 For Sendai, the acceleration time history was provided from GL-0 to -8 m every 1 m,
586 while the stress-strain curves from GL-0 . 5 to -7.5 m also every 1 m.

587 **Analysis of results**

588 This article focuses on the analysis of the whole dataset returned from each team to
589 estimate the level of uncertainties associated to NL modelling.

590 Several sources of uncertainties are involved in 1-D non-linear site response analyses.
591 On one hand, there are epistemic uncertainties coming from the main assumption of the
592 method (1-D, vertical propagation of SH waves), soil parameters measurements (which
593 should however impact all the predictions in the same way), the numerical model and
594 the users. On the other hand, there are random uncertainties coming from the input
595 motions, which are influenced by both the seismic sources and soil heterogeneities. We
596 did use several input motions; however, the number of them is not sufficient to take into
597 consideration all the random uncertainty ranges. The previous verification phase
598 (Régnier et al., 2016) provided an estimation of the code-to-code variability linked to the
599 numerical method such as numerical integration schemes, implementations of damping,
600 constitutive models and users practice. Conversely, the validation phase involves
601 comparison with observations and therefore calculations of residuals. We assume that
602 the residual can be described as a random variable with normal distribution center
603 around a non-necessarily zero mean (models may over or under-predict), with
604 associated standard deviation.

605 We calculated and compared the misfit between the observations and the computations
606 with the code-to-code variability of the surface response spectra averaged over a period
607 band-width close to the resonance period of the site, namely $[0.7 f_0, 1.3 f_0]$. The misfit
608 reflects the total uncertainty (epistemic and random) of the results; whereas the code-
609 to-code variability illustrates the part of the epistemic uncertainty associated with the

610 choice of a numerical model. Then, this code-to-code variability is compared to the
611 previous results obtained in the verification exercise done on simplified soil profiles.

612 An additional analysis was performed to consider the soil column choice in the whole
613 uncertainty assessment. The misfit was calculated for each input motion and all soil
614 columns (SC1, SC2 and SC3) together.

615 Finally, the results at each site were analyzed, through the distribution of the computed
616 transfer functions and response spectra, using the 25th and 75th percentiles of all
617 computations, and comparing them to the observations. Concomitantly, we also
618 computed and analyzed the distribution of residuals on response spectra to quantify the
619 discrepancy and identify when the observations were under and over-estimated. This
620 operation was carried out at each oscillator period.

621 **Code-to-code variability versus misfit**

622 A first analysis of the code-to-code variability (called hereafter σ_{c2c}) relative to the
623 variability of the residuals between the recording and the simulations (called hereafter
624 *Misfit*) is provided.

625 To quantify the *Misfit*, we calculate the root mean square distance between each
626 prediction with the observation of the response spectra as proposed in equation Eq 7
627 and averaging it (geometric mean) over the periods of interest of the site.

$$628 \quad Misfit = \left(\prod_{i=1}^n RMSD_{obs-num}(T_i) \right)^{\frac{1}{n}}$$

629 *where*

630
$$RMSD_{obs-num}(T_i) = \sqrt{\frac{1}{Nc-1} \sum_{j=1}^{Nc} [LSA_{obs}(T_i) - LSA_{num,j}(T_i)]^2}$$

Eq 7

631 *Where n is the number period sample between $T_1=1/(1.3f_0)$ and $T_2=1/(0.7f_0)$ of the discrete*
 632 *response spectra SA; $\overline{LSA_{obs}}$ is the logarithmic (to base 10) transformation of the observed*
 633 *SA; $LSA_{num,j}$ is the logarithmic transformation of j^{th} surface predicted SA.*

634 The code-to-code variability (σ_{c2c}) is the standard deviation of the predictions as defined
 635 in equation Eq 8, averaged over the same period range as before.

636

637
$$\sigma_{c2c} = \left(\prod_{i=1}^n RMSD_{num}(T_i) \right)^{\frac{1}{n}}$$

638 *where*

639
$$RMSD_{num}(T_i) = \sqrt{\frac{1}{Nc-1} \sum_{j=1}^{Nc} [\overline{LSA_{num}}(T_i) - LSA_{num,j}(T_i)]^2}$$

640

Eq 8

641 *Where n is the number period sample between $T_1=1/(1.3f_0)$ and $T_2=1/(0.7f_0)$ of the discrete*
 642 *response spectra SA; $\overline{LSA_{num}}$ is the logarithmic (to base 10) transformation of the mean*
 643 *predicted SA; $LSA_{num,j}$ is the logarithmic transformation of j^{th} surface predicted SA.*

644 The considered period range spans an interval of $\pm 30\%$ around the fundamental
 645 resonance frequency of the sites (f_0) (8.2 and 1.7 Hz for Sendai and KSRH10,

646 respectively). For Sendai it corresponds to the frequency range from 5.47 to 10.66 Hz,
647 equivalent to periods between [0.09-0.18] s. For KSRH10, the adopted frequency interval
648 is [1.19-2.21] Hz, corresponding to periods between [0.45-0.84] s. The periods are log-
649 scale sampled.

650 Regarding the soil column, the SC1 soil model provided closer results to the observation
651 compared to the SC2 at Sendai. On the opposite, for KSRH10, SC2 and SC3 models led to
652 lower misfit values.

653 Figure 7 compares the *Misfit* on the East-West component for Sendai and North-South
654 component for KSRH10 (filled markers), with the code-to-code distance σ_{c2c} (empty
655 markers). The simulated component (EW or NS) with less discrepancy with the
656 observations was chosen.

657 For Sendai, we compared the results for four input motions (1, 2, 5 and 8, for which all
658 calculations were performed) and for the two soil models SC1 and SC2. For KSRH10, it is
659 illustrated for 5 input motions (0,1,2, 4 and 9) and for the 3 soil models (SC1, SC2 and
660 SC3). As expected, the misfit is systematically higher than the code-to-code variability
661 regardless the input motion or site considered: actually they could be equal only if the
662 predictions are unbiased in average, i.e., if $\overline{LSA_{num}(T_i)} = LSA_{obs}(T_i)$ for every period
663 T_i . – which actually never happens... It is also worth observing that the code-to-code
664 variability is quite the same regardless the input motion or the site or the soil columns
665 considered and has a minimum value of 0.06 and a maximum value of 0.15. This
666 suggests that for 1-D seismic response analyses, the epistemic uncertainty related to the
667 choice of the numerical method and soil constitutive model should be considered
668 between 0.06 and 0.15 (in log10 scale). Those values, when compared to well-known

669 uncertainty estimation such as in GMPEs (Ground Motion Prediction Equations), lying
670 between 0.15 to 0.35 (Strasser et al., 2009), are significant and should be taken into
671 account for seismic hazard assessment. One must also keep in mind that such values
672 correspond to a relatively narrow frequency range, and may not be representative of the
673 variabilities in other frequency ranges (as may be seen on Figure 8).

674 The misfits are generally lower for the weakest input motions regardless the site
675 considered, although slightly more pronounced for the KSHR10 site. This is expected
676 because the predictions are closer to one another and also closer to the observations
677 when the soil response is mainly in the linear range. An exception is observed at Sendai
678 for TS-5-S, for which the misfit is larger for a moderate PGA. The misfits between
679 observations and simulations are found significantly lower at Sendai than at KSRH10.
680 They lie between 0.1 and 0.25 at Sendai, while they are in the interval between 0.08 and
681 0.35 for KSRH10.

682 Regarding the soil column, the SC1 soil model provided closer results to the observation
683 compared to the SC2 at Sendai. On the opposite, for KSRH10, SC2 and SC3 models led to
684 lower misfit values.

685 *Figure 7*

686 **Comparison between verification and validation epistemic variability**

687 In this section, the variability of the predictions performed during (1) the verification
688 phase on canonical cases (3 profiles P1, P2 and P3 with fundamental resonance
689 frequencies of 3.75, 1.16, 1.58 Hz respectively) and (2) the validation phase on real sites
690 are compared in terms of standard deviation (log10 unit) of the PGA and spectral
691 accelerations at 0.1, 0.3 and 1s at the surface.

692 We provide the results in Figure 8. For the validation phase, the standard deviation is
693 calculated for KSRH10 for the input motions: TS-9-K, TS-4-K, TS2-K, TS-1-K and TS-0-K.
694 For Sendai it is calculated for the input motions TS-8-S, TS-5-S, TS-2-S and TS-1-S. As far
695 as the verification phase is concerned, we considered only the results for the first profile
696 P1, the rigid substratum case and the non-linear computations. The numerical results
697 depend on the input motion level and on the frequency content (HF stand for High
698 Frequency input motion and LF for Low frequency, see Régnier et al., 2016): the
699 variability increases with the strain level developed in the soil column. It is therefore
700 higher at high PGA and for the low frequency content input motion. The Low Frequency
701 (LF) waveform generates higher strains compared to the High Frequency (HF)
702 waveform, for the same PGA level (black empty triangles). This is because the frequency
703 content of the input motion is close to the resonance frequency of the canonical site.
704 Therefore, strong resonance effects are expected. In the validation phase, the variability
705 is generally larger for the stronger input motions except at KSRH10 site for periods
706 above 0.3s.

707 *Figure 8.*

708 **Propagation of the epistemic uncertainty**

709 We built a logic tree similarly to what is done in Probabilistic Seismic Hazard
710 Assessment, to propagate the uncertainty of the numerical simulation and interpretation
711 of the soil data from in-situ and laboratory measurements to the site response and
712 surface response spectra assessment. For each site (Sendai or KSRH10) and each input
713 motion this logic tree is composed of two nodes (as shown in Figure 9). The first node is
714 the soil column (SC1 and SC2 for Sendai, SC1, SC2 and SC3 for KSRH10) and the second
715 node is relative to the team and code couple (from EA-0 - team A with his first code - to

716 EZ-1 - team Z with his second code). All branches of the tree have the same weight. The
717 uncertainty is quantified by the standard deviation of residuals of the logarithm (log10
718 unit) of the results (here PGA and response spectra at the surface at 3 periods 0.1, 0.3
719 and 1s) as defined in Eq 7.

720 Table 5 synthesizes the standard deviation of the results obtained in the present
721 PENOLIN exercise. It might be noted that the root mean square of residuals (RMSD) are
722 in most cases lower for Sendai compared to KSRH10, except for longer periods (1s).
723 (period close to the KSRH10 fundamental resonance frequency where the fit is good).
724 The fit is generally better for weak input motions, except at Sendai for the response
725 spectra above 0.1s.

Figure 9

726

Table 5

727

728 **Comparison of transfer function and response spectra between soil columns**

729 Let us analyze more precisely for each period (frequency) the differences between
730 predictions and observations. The 25% and 75% percentiles of the surface response
731 spectra and the borehole transfer functions are compared to the observations, for a
732 strong and a weak input motion. We selected TS-1-S and TS-8-S for Sendai and TS-1-K
733 and TS-9-K for KSRH10.

734 Besides, to quantify the discrepancy between observations and predictions the average
735 residuals (R) per period was calculated according to as shown in Eq 9.

736
$$R(T) = \frac{\sum_{j=1}^{Nc} [LSA_{obs}(T) - LSA_{num,j}(T)]}{Nc}$$

Eq 9

737 Where Nc is the number of computations; $\overline{LSA_{obs}}$ is the logarithmic (base 10) of the
 738 observed SA; $LSA_{num,j}$ is the logarithmic of the j th surface predicted SA.

739 *Sendai*

740 In Sendai, the results of the computations are closer to the observations when using soil
 741 model 1 (SC1), which was defined using literature parameters. In Figure 10, the transfer
 742 functions are compared, the fundamental resonance frequency (f_0) of the observations
 743 for a weak input motion (TS-8-S) is equal to 8.5 Hz, which is well reproduced by the
 744 numerical computations using either SC1 or SC2 soil parameters. For the strongest input
 745 motion (TS-1-S) f_0 is equal to 7.3Hz in the observations. In the computations, f_0 is similar
 746 when using SC1 soil parameters while for SC2, f_0 is slightly above (7.8 Hz), indicating a
 747 lower level of non-linearity when using SC2 soil parameters compared to SC1. Similarly,
 748 as illustrated in Figure 11, the surface response spectrum is well reproduced by the
 749 computations using the two soil columns for weak motion (TS-8-S) while for the strong
 750 motion (TS-1-S) the prediction using SC1 is closer to the observation as compared to the
 751 SC2 soil column. Those observations are also highlighted in Figure 12, the residuals are
 752 close to 0 for the weakest input motion (TS-8-S) for which the two soil columns provide
 753 similar estimations. For the strongest input motion we observe an over-estimation
 754 below 0.2 s. For TS-5, the under-estimation is observed for both soil columns while for
 755 TS-1-S and TS-2-S it is mainly observed for SC2. It shows that the discrepancy between
 756 the observations and the predictions for TS-5-S does not depend on the soil column
 757 characteristics and may be associated with the input motion specificity.

758 These first results were somehow disappointing, since site-specific measurements failed
759 in predicting the observations where generic parameters succeeded. We investigate the
760 source of this discrepancy that could come either from a measurement error or a mis-
761 interpretation of the laboratory tests. For Sendai site, there is a large variability between
762 the measured laboratory shear modulus and the in-situ measurement. The shear
763 modulus from the laboratory measurement is equal to 25 MPa at 3.3 m depth, compared
764 to 100 MPa from the *in situ* measurement of V_s (230 m/s) and density values (1890
765 kg/m³). This observation suggest that the correction of the laboratory data should have
766 been apply to Sendai site as well.

767 The procedure to correct the G/G_{max} curves, as indicated previously, has not been applied
768 to the laboratory at Sendai data before the calculations, but it was performed a
769 posteriori.

770 The comparison of the G/G_{max} curves of SC2 model with G/G_{max} curves from laboratory
771 data did not indicate modifications that could explain the large misfit for SC2 model. We
772 recall that this procedure is supposed to correct only for measurement errors between
773 external and local shear strain devices. Considering the large uncertainty that can lie in
774 the value of the G_{max}^{lab} it is highly recommended that low strain measurements, such as
775 resonant column or bender element should be used in addition to cyclic tri-axial test to
776 define these parameters.

777 *Figure 10*

778 *Figure 11*

779 *Figure 12*

780 *KSRH10*

781 KSRH10 is a deep sedimentary site with down-hole station at GL-255 m. We can observe
782 that the site response (Fourier transfer function) is variable depending on the
783 component of motion and hard to reproduce above the fundamental resonance peak.

784 In Figure 13, the recorded transfer function is variable from one component of motion to
785 another especially for TS-1-K, where the amplitude of the fundamental resonance peak
786 is equal to 25 for the NS component and only 16 for the EW component. The frequency
787 peaks between 2 to 5 Hz are variable from component to component and event to event
788 and could not be predicted by the 1D assumptions made in this study. For TS-1-K we
789 observe a second and third peaks at 2.3 and 3.3 Hz for the EW component and at 2.7 and
790 3.2 Hz for the NS component while only one peak is predicted by the numerical
791 simulation with a very high amplitude at 2.7 Hz (high amplitude in the surface Fourier
792 spectrum). For TS-9-K, we observe 3 peaks at 2.3, 3.2 and 4 Hz and only one is predicted
793 by numerical simulations at 2.6 Hz. The fourth peak, close to 7 Hz, is more stable from
794 one component to another, but the frequency is slightly over-estimated and the
795 corresponding amplitude is under-estimated when using the SC1 column.

796 At high frequencies (above 12 Hz), a de-amplification is observed in the empirical
797 borehole transfer function that is not reproduced by the simulations. One possible
798 explanation is the existence of a noticeable soil-structure interaction at the
799 accelerometer sites: this was proposed by DPRI based on their own experience at several

800 sites and many events. This may also add to some side effects of the low-pass filtering of
801 all KiK-net recordings below 25 Hz. Other possible contributions to this high-frequency
802 reduction may be larger damping (especially for low strains) or scattering from shallow,
803 small size heterogeneities.

804 For the fundamental resonance peak, we found that SC2 and SC3 soil columns coming
805 from in-situ measurements provided closer results to the observations than the SC1
806 defined using literature G/G_{max} curves (Darendeli, 2001). As shown in Figure 13, for TS-
807 1-K input motion, the amplitude of the observed resonance frequency peak at 1.4 Hz is
808 around 25 for the NS component, while SC1 column predicted amplitudes (in the 25-75
809 percentiles envelope) between 12 and 14 only.

810 As seen in Figure 14, the amplitude of the surface response spectra for the NS
811 component is relatively well reproduced for the weak input motion TS-9-K, but the
812 periods of maximal amplitudes are shifted, creating an over-estimation at 0.13 s and
813 0.34 s and an under-estimation at 0.18 and 0.25 s. These discrepancies are related to the
814 differences between the observed and computed frequency peaks in the transfer
815 function. For TS-1-K, the amplitude is well reproduced except for SC1 soil column for
816 which the amplitude is significantly under-estimated between 0.1 and 0.34 s. The
817 surface response spectra from the computations using SC2 and SC3 soil columns are
818 closer to the observations.

819 In Figure 15 we observe the residuals of the response spectra; the recordings are under
820 and over-estimated especially for periods close to 0.35 s for TS-1-K to TS-9-K input
821 motions. The under-estimation amplitude increases with the input motion intensity and
822 is more important for the soil column SC1.

823 At KSRH10, the site-specific measurements on non-linear properties provide more
824 satisfactory results than the generic curves. The type of soil of KSRH10 was analyzed in
825 detail by one of the participant (Lanzo, personal communication). The non-linear
826 parameters (normalized shear modulus reduction and damping curves) defined in SC2
827 and SC3 are less non-linear compare to classical literature curves even for similar type of
828 soil (i.e SC1). This observation is consistent with the fact that KSRH10 is composed of
829 volcanic sand, as indicated by site geology. Several authors have shown that volcanic
830 sand exhibits a lower non-linear behavior as compared to classical sand. For example,
831 laboratory experimental tests conducted by Senetakis et al., (2013) show that pumice
832 sands exhibit a slower normalized stiffness decay and a lower dissipative behaviour than
833 classic gravel curves (Rollins et al., 1998). Similar experimental results have been
834 obtained in Italy on volcanic materials such as Colle Palatino tuff in Rome (Pagliaroli et
835 al., 2014), Naples Pozzolana (Papa et al., 1988) and Orvieto (Central Italy) pyroclastic
836 materials (Verrucci et al., 2015). Thus, Darendeli's curves built on "classical" sand data
837 could not necessarily reproduce the non-linear soil behavior at this site. This exercise
838 suggests that one should be careful when using generic soil curves, such as Darendeli
839 (2001) or others: the soil nature is important to evaluate their relevancy in site response
840 analyses.

841 *Figure 13*

842 *Figure 14*

843 *Figure 15*

844 **Discussion and conclusions**

845 **Applicability of the calculations**

846 The computations performed in this benchmark are limited by three main assumptions:
847 (1) 1-D wave propagation in horizontally layered media (2) SH waves (only one
848 component of motion) with vertical incidence and (3) total stress analysis.

849 *1-D structure*

850 We succeed to reproduce at both sites the fundamental resonance frequency (for weak
851 and strong motions) but the higher modes remain difficult to reproduce. The sites were
852 chosen (over 688 sites in KiK-net) to fulfill specific criteria warranting limited deviations
853 from a 1-D site configuration. We observe at KSRH10 site that 1-D numerical simulation
854 could not reproduce the observed site response over the whole frequency range, even
855 for weak motions: this is likely to indicate that the site has more complex geometry. The
856 1-D structure assumption is a very strong one which may not be realistic. However,
857 moving forward for more complex geometries requires more detailed site
858 characterization over a broader area, adequate interpretation of the data and application
859 of 2-D and 3-D numerical simulations (Amorosi et al., 2016; Dupros et al., 2010; Taborda
860 et al., 2010). Benchmarking non-linear numerical codes for 2D or 3D geometries is a real
861 challenge, which should start with a carefully designed verification exercise.

862 *Vertically incident SH waves*

863 Vertically incident SH waves loading implies two distinct assumptions: a) vertically
864 incident plane waves, and b) a uni-directional motion in the whole soil column.

865 The former has been partially tested through a polarization analysis and has been found
866 only partially fulfilled. In any case, there is not enough information from the two-sensor
867 recordings to constrain the complexity of the incident wavefield, which is an unknown
868 mixture of body waves with varying incidence angles and backazimuths, and surface
869 waves with varying back-azimuths.

870 Concerning the second assumption, one participant tested a code with an
871 implementation of a 3 Components (3C) non-linear constitutive relation. Using a 3C non-
872 linear constitutive model has been shown to be relevant for strong ground motion
873 prediction with 1D wave propagation models for a large event such as Tohoku 2011
874 (Santisi d'Avila and Semblat, 2014). The 3D loading path due to the 3C-polarization leads
875 to multiaxial stress interaction that reduces soil strength and increases nonlinear effects.

876 Therefore, for Sendai site, results of 1D analysis performed using 3 component codes
877 (1D, 3-components) were compared to those obtained by 1D analysis with only one
878 component of motion (1D, 1-component, vertical incidence) see figure S6 in the
879 electronic supplement. Simulations were carried out with reference to the SC2 soil
880 column, which is less non-linear than the SC1, and considering the strongest input
881 motion (TS-1-S).

882 As illustrated in the electronic supplement figure S6 no significant differences between
883 the two results were observed and cannot explain the discrepancy between the

884 predictions and the observation. Additional research is needed to further explore the
885 impact of 3C motions versus 1C assumption.

886 *Total stress versus effective stress analysis*

887 Even though the exercise was limited to a total stress analysis, and designed accordingly,
888 we thought useful to benefit from the willingness of some volunteer participants to
889 investigate whether the type of analysis (effective or total stress) or the input soil model
890 used could improve the fit. Two teams (W-0 and H-0) performed those calculations at
891 Sendai site. In the electronic supplement, figure S7 presents the borehole transfer
892 function computed for soil columns SC1 and SC2 sorted according to the type of analysis
893 (Total stress analysis, Equivalent linear or effective stress analysis), as compared to the
894 observations for two different input motions (TS-1-S and TS-8-S). We observe that the
895 weak motion effective stress analysis provides results close to total stress analysis, as
896 expected. This is also the case for the strongest input motion when dealing with SC2 soil
897 parameters. However, one team (W-0) succeeds to reproduce the observations even with
898 SC2 soil parameters, when using an effective stress-analysis. That team indicated that
899 the non-linear input data used in this analysis were calibrated directly from the
900 laboratory tests and adjusted to the in-situ measurements of elastic properties. The
901 G/G_{max} curves obtained were closer to the curves used in SC1 rather than SC2. Therefore,
902 no evidence of efficiency of effective stress analysis compared to total stress analysis is
903 available for Sendai site. Additional research is required to further evaluate the
904 conditions under which an effective stress analysis is needed.

905 *Equivalent linear method*

906 In addition to the time domain nonlinear site response analyses limited by these three
907 assumptions, the equivalent linear method (EQL) was also tested. This approach

908 involves a linear computation, coupled to an iterative process that adjusts at each
909 iteration the value of the shear modulus and damping, according to the maximum shear
910 strain calculated at the middle of each soil layer. This method is largely used in
911 earthquake engineering practice since the pioneering work of Schnabel et al., 1972.
912 Three teams used an equivalent linear method (J-1 and Z-0). Team J-1 performed all the
913 calculations, whereas Z-0 provided the results of the equivalent linear method only for
914 the weakest input motions. In the electronic supplement, the figure S7 depicts the
915 results obtained from the equivalent linear method. The EQL results are close to the total
916 stress analysis for the weakest input motion and for the strongest input motion when
917 SC2 soil parameters are considered. However, for the SC1 soil column it should be noted
918 that the shift of the fundamental resonance frequency towards lower values is much
919 higher for the EQL methods and that the high frequencies are largely de-amplified. The
920 strain levels for TS-1-S using SC1 reach 0.3 % and up to 0.7 % for some computations,
921 while for SC2 maximum shear strain values are below 0.2%. For SC1 such high shear
922 strain level implies a decay of shear modulus to 0.1 times the maximum shear modulus.
923 Such results confirm that the EQL approach should not be used beyond strain levels
924 around 0.2 %, consistently with the results presented in Kim et al., (2016) after a
925 comprehensive set of numerical simulations for many different sites, and those also
926 obtained earlier by Ishihara (1996) and Yoshida and Iai (1998).

927 **Main outcomes on NL prediction uncertainties**

928 The present benchmarking exercise allowed to provide some quantitative estimates on
929 the epistemic uncertainty associated to 1D non-linear modeling, which should be
930 considered as lower bound estimates as it is rather rare for practical engineering studies
931 to have as many information as in the present case. Figures 7, 8 11 and 15 indicate that:

- 932 • The code-to-code variability is generally in the range 0.05-0.25 (log10 scale), with
933 a slight trend to decrease with increasing period.
- 934 • The smaller code-to-code variabilities are found to correspond to the "SC1 case",
935 i.e. here to the Darendeli model, while higher variabilities are found for NL
936 models based on in-situ sampling and dedicated laboratory characterization. We
937 interpret this finding as related to the higher non-linearity level implied by the
938 Darendeli model, resulting in generally weaker motion. The decrease of the
939 uncertainties due to an increase of non-linear soil behavior has been notify in
940 previous studies (Bazzurro and Cornell, 2004; Stewart et al., 2017).
- 941 • The misfit (i.e. root mean square average distance to the actual motion) is larger
942 than the code-to-code variability because of model errors (soil parameters,
943 improper 1D assumption, total stress, etc.), and misfit increases with increasing
944 loading level (Figure 7). It may reach values from 0.25 to 0.35 (log10 scale)
945 around the site fundamental frequency where the variability is the highest
- 946 • This misfit exhibits a strong frequency dependence, with the lowest values below
947 the fundamental frequency, and largest around f_0 and above. Models may over-
948 predict the site response at some frequency, and under-predict it at other
949 frequencies
- 950 • The prediction of non-linear site response seems easier for shallow soil deposits
951 than for deeper deposits: the first obvious reason is that the code-to-code
952 variability is mainly visible beyond the site fundamental frequency, which is
953 higher for shallow deposits. In addition, deep deposits not only imply a larger
954 number of sample measurements corresponding to varying depths, but the

955 wavefield is likely to be more complex, as well as the perturbations due to non 1D
956 layering.

957 • The widely used, average models such as the Darendeli's ones (SC1), are found to
958 perform rather well for one site (better than the models based on in-situ
959 sampling and laboratory measurements (SC2 and SC3), and less well for the other
960 site. It is impossible to generalize from only two sites, but it is worth mentioning
961 that the first case corresponds to very shallow (depth smaller than 10 m), mainly
962 sandy materials, while the second corresponds to deeper, more clayey material,
963 exhibiting less non-linearity than predicted by Darendeli's model

964 Finally, one should keep in mind that the results were obtained for rigid base conditions
965 only since they correspond to an input motion recorded at a down-hole sensor. In most
966 practical engineering studies, the "reference motion" corresponds to outcropping rock
967 conditions. The epistemic uncertainty and misfit are then likely to increase especially
968 when the base of the soil column corresponds to much harder bedrock than the
969 "standard" conditions corresponding to a shear wave velocity around 800 m/s: the need
970 for host-to-target adjustments (Campbell, 2003; Van Houtte et al., 2011; Al Atik et al.,
971 2014) then results in increased epistemic uncertainty as recently emphasized by
972 Ktenidou and Abrahamson (2016), Aristizabal et al. (2017) and Laurendeau et al.
973 (2017),

974 **From lessons learnt to tentative recommendations for further benchmarking exercises and**
975 **NL modelling**

976 This last section intends to provide advices for users of 1-D non-linear site response
977 codes and for next benchmarking exercises, since there is still need for further works,

978 regarding effective stress analysis, NL effect for 2D or 3D media and for more complex
979 incident wavefield as well.

980 We try to provide an overview of the issues one can encounter when applying those
981 methods and the adapted solutions we found. They are built only partly on the results of
982 this benchmark and refers to several other studies, among which previous recent
983 benchmarks on similar methods (Stewart and Kwok, 2009; Stewart, 2008).

984 We formulate the following recommendations for applying 1-D nonlinear site response
985 in absence of pore pressure effects.

986 *Preliminary checks*

987 Whatever the numerical method, it is necessary to verify and, if possible, to validate the
988 code used. In particular, if the method used or developed has not been already verified
989 or validated, canonical cases have been uploaded on the Internet for online
990 verification/validation (See Data Resources section).

991 A verification and validation study, coupled with a documentation of the theory and
992 implementation of a site response method or software, is highly desirable prior to any
993 analyses.

994 The decision of applying a non-linear analysis rather than a linear or equivalent linear
995 method can follow recommendations for a priori evaluation of differences between EQL
996 and nonlinear site response simulations such as those presented in Kim et al. (2016).
997 EQL results are considered unreliable when the peak strains – or some associated
998 proxies such as PGV/VS30 - exceed some thresholds – which may be frequency
999 dependent (Assimaki and Li, 2012, Kim et al., 2016).

1000 If only one numerical method is used, consider that the variability on the results
1001 (standard deviation on pseudo-response spectra) due to the choice of the numerical
1002 method is around 0.1 (in log10 scale unit) in average, but may reach values up to 0.2 at
1003 short periods or around the site fundamental frequency (Régnier et al., 2016a).

1004 **Input data**

1005 *Input motion*

1006 The definition and the processing of the input motion coming from recorded motions
1007 (outcrop or within) requires careful attention.

1008 In this study, the input waveforms were processed according to the procedures proposed
1009 by Boore and Bommer, (2005), which include the following steps: (1) removing the
1010 mean, (2) finding the first and last zero-crossing and then adding zeroes before and after
1011 these points over a specific time as a function of the number of poles of the high pass
1012 filter to be used (here we added 20 s before and after) and (3) applying a Butterworth
1013 high pass filter at 0.1 Hz. This kind of pre-processing is very important when using codes
1014 that integrate different input motions (for example, from acceleration, from velocity or
1015 from displacement, respectively), in order to ensure having compatible acceleration,
1016 velocity and displacement time histories depending of the code's input. In addition, the
1017 so prepared input motion has no energy below and above the frequency resolution of
1018 the numerical method, which avoids a possible overestimation of permanent surface
1019 displacements.

1020 As recommended by Kwok et al., (2007), in linear/equivalent and linear/non-linear site
1021 response analyses, two cases can be distinguished: (1) if the reference motion is an
1022 outcrop recording, then one should use an elastic base condition with an up-going wave

1023 carrying a signal equal to exactly half the outcropping motion; (2) if the reference
1024 motion is a within motion recorded by a down-hole sensor, then one should use a rigid
1025 base condition without modifying the reference motion or should deconvolve the down-
1026 going wave from the within motion and input the up-going wave with elastic base
1027 condition.

1028 *Soil characterization*

1029 It is recommended that a linear analysis be conducted prior to any nonlinear simulations
1030 to check that the elastic and visco-elastic properties have been well defined and
1031 implemented (check of the expected fundamental resonance frequency if available).

1032 If the site is suspected to have significant lateral variability (Matsushima et al., 2014),
1033 then the characterization should involve measurements of the spatial variability of the
1034 soil layer (depth and soil properties) and 2D or 3D site response may be needed to
1035 capture site effects.

1036 Non-linear parameters, should be defined as a function of depth. The shear modulus
1037 reduction and damping curves as functions of shear strain should be associated and
1038 compatible with the shear strength and V_s profiles. To find the values of the non-linear
1039 parameters, it is recommended to use site specific measurements (e.g. drilling, sampling
1040 and laboratory measurements) with comparisons to literature data and relationships for
1041 similar materials (e.g. Darendeli, 2001; Ishibashi and Zhang, 1993; Menq, 2003; Roblee
1042 and Chiou, 2004; Zhang, 2006).

1043 In this study, it was found that the SC1 model provided good results for one site, but not
1044 the other, which was better captured with the SC2 and SC3 soil curves. This was
1045 attributed to the unique nature of the geology of the second site. Pre-defined literature

1046 curves can produce acceptable estimations of site response, but need to be evaluated
1047 based on the site geology. In this study, cyclic-triaxial tests were found to be not always
1048 reliable at low strains. Resonant column or blender element tests are useful and can
1049 provide complementary measurements to constrain the normalized stiffness decay
1050 curves at low strains. Further investigation in future studies, for a larger set of sites and
1051 simulations, would greatly help in establishing consensual procedures for bridging in-
1052 situ, low-strain and laboratory high-strain measurements. Elastic properties measured
1053 in the laboratory should be compared with in-situ measurements; the soil sample size,
1054 the soil disturbance and the measurement errors can lead to discrepancies between the
1055 measurement in the laboratory and in-situ. The way to adapt the nonlinear curves and
1056 elastic properties measured in the lab to elastic properties measured in situ should be
1057 detailed and uncertainties on these parameters should be accounted for: the lack of a
1058 common, widely accepted procedure is a source of large epistemic uncertainty in the
1059 assessment of NL soil properties, and thus in the prediction of site response under
1060 strong motion.

1061 **Conclusion**

1062 This benchmark was limited to 1-D non-linear total stress analysis. This simple case was
1063 chosen to ensure an, as clear as possible, identification of the impact of various
1064 approaches to implement the non-linearity and the associated parameters. We
1065 calculated the variability between predictions and the misfit with observations. The
1066 variability between codes indicate that the choice of a non-linear model must be coupled
1067 with an uncertainty from 0.05-0.25 (in log₁₀ scale) to reflect the variability from the
1068 code, the numerical method, the constitutive model and the user. This uncertainty is
1069 generally not considered in any site-specific response analysis. The misfit is even greater

1070 than the variability between codes, and is associated to the definition of the soil
1071 parameters and intrinsic assumptions of the method (1-D site and vertical propagation
1072 of SH waves without pore water pressure effects). The misfit increases with increasing
1073 loading level and may reach values from 0.25 to 0.35 (log10 scale) around the site
1074 fundamental frequency. It is frequency dependent and can be an over-prediction and an
1075 under-prediction depending of the frequency bandwidth.

1076 Further investigations are needed to propose recommendations as for the method to
1077 obtain non-linear parameters. Indeed, at Sendai site pre-defined literature curves
1078 provided better results, whereas for KSRH10, site specific curves from laboratory tests
1079 were closer to the observations.

1080 The experience gained from this thorough benchmarking exercise allows to propose
1081 some recommendations for either operational studies or future, more advanced
1082 benchmarks. The latter are definitely needed as some issues, in relation to the main
1083 assumptions behind the widely used 1D approach, were clearly identified, as potentially
1084 impacting the misfit between numerical predictions and instrumental recordings:
1085 complexity of the geometry, dimensionality of the input motion and complexity of the
1086 wavefield, or constitutive model with or without water pressure. Addressing those
1087 issues was much beyond the scope of the present project, but each of them would
1088 deserve a dedicated benchmark. We hope that sharing the PRENOLIN experience will
1089 contribute to the design of such future studies.

1090 **Data and Resources**

1091 **Time histories used in this study** were collected from the KiK-net website
1092 www.kik.bosai.go.jp and <http://www.kik.bosai.go.jp/kik/> (last accessed November
1093 2011) and from PARI, Port and Airport Institute in Japan .

1094 **Some codes used in this work have the following URL links:**

1095 ASTER, <http://www.code-aster.org> (last accessed October 2015);

1096 EPISPEC1D, <http://efispec.free.fr> (last accessed October 2015);

1097 Real ESSI simulator, <http://sokocalo.engr>.

1098 ucdavis.edu/~jeremic/Real_ESSI_Simulator/ (last accessed October 2015);

1099 OpenSees, <http://opensees.berkeley.edu/> (last accessed October 2015);

1100 DEEPSOIL, <http://deepsoil.cee.illinois.edu/> (last accessed October 2015);

1101 SeismoSoil, <http://asimaki.caltech.edu/resources/index.html#software> (last accessed
1102 October 2015). The unpublished manuscript by

1103 **Verification and validation exercises :**

1104 - For 2D/3D linear methods: <http://www.sismowine.org> (last accessed July 2017)

1105 - for 1-D non-linear (PRENOLIN): <http://prenolin.org> (last accessed July 2017)

1106 **References**

1107

1108 Amorosi, A., Boldini, D., di Lernia, A., 2016. Seismic ground response at Lotung: Hysteretic

- 1109 elasto-plastic-based 3D analyses. *Soil Dyn. Earthq. Eng.* 85, 44–61.
- 1110 Assimaki, D., Li, W., 2012. Site and ground motion-dependent nonlinear effects in
1111 seismological model predictions. *Soil Dyn. Earthq. Eng.* 143–151.
- 1112 Aubry, D., Hujeux, J.C., Lassoudiere, F., Meimon, Y., 1982. A double memory model with
1113 multiple mechanisms for cyclic soil behaviour, in: *Proceedings of the Int. Symp. Num. Mod.*
1114 *Geomech.* pp. 3–13.
- 1115 Bazzurro, P., Cornell, allin, 2004. Ground-motion amplification in nonlinear soil sites with
1116 uncertain properties. *Bull. Seismol. Soc. Am.* 94, 2090–2109.
- 1117 Bonilla, L.F., Archuleta, R.J., Lavallée, D., 2005. Hysteretic and Dilatant Behavior of
1118 Cohesionless Soils and Their Effects on Nonlinear Site Response: Field Data Observations
1119 and Modeling. *Bull. Seismol. Soc. Am.* 95, 2373–2395.
- 1120 Bonilla, L.F., Steidl, J.H., Gariel, J., Archuleta, R.J., 2002. Borehole response studies at the
1121 Garner Valley downhole array southern California. *Bull. Seismol. Soc. Am.* 92, 3165–3279.
- 1122 Boore, D.M., Bommer, J.J., 2005. Processing of strong-motion accelerograms: needs, options
1123 and consequences. *Soil Dyn. Earthq. Eng.* 25, 93–115.
- 1124 Darendeli, M.B., 2001. Development of a new family of normalized modulus reduction and
1125 material damping curves.
- 1126 De Martin, F., Matsushima, S., Kawase, H., 2013. Impact of geometric effects on near-surface
1127 Green's functions. *Bull. Seismol. Soc. Am.*
- 1128 Dupros, F., De Martin, F., Foerster, E., Komatitsch, D., Roman, J., 2010. High-performance
1129 finite-element simulations of seismic wave propagation in three-dimensional nonlinear
1130 inelastic geological media. *Parallel Comput.* 36, 308–325.

- 1131 Elgamal, A.-W., Zeghal, M., Parra, E., 1996. Liquefaction of reclaimed island in Kobe, Japan.
1132 J. Geotech. Eng. 122, 39–49.
- 1133 Elgamal, A.-W., Zeghal, M., Tang, H.T., Stepp, J.C., 1995. Lotung downhole array. I:
1134 Evaluation of site dynamic properties. J. Geotech. Eng. 121, 350–362.
- 1135 Groholski, D.R., Hashash, Y.M., Kim, B., Musgrove, M., Harmon, J., Stewart, J.P., 2016.
1136 Simplified model for small-strain nonlinearity and strength in 1D seismic site response
1137 analysis. J. Geotech. Geoenvironmental Eng. 142, 4016042.
- 1138 Gunturi, V.R., Elgamal, A.-W., Tang, H.T., 1998. Hualien seismic downhole data analysis.
1139 Eng. Geol. 50, 9–29.
- 1140 Hardin, B.O., Drnevich, V.P., 1972. Shear Modulus and Damping in Soils. J. Soil Mech.
1141 Found. Div. 98, 667–692.
- 1142 Haskell, N.H., 1953. The dispersion of surface waves in multilayered media. Bull. Seismol.
1143 Soc. Am. 43, 17–34.
- 1144 Ishibashi, I., Zhang, X., 1993. Unified Dynamic shear moduli and damping ratio of sand and
1145 clay. Soils Found. 33, 182–191.
- 1146 Ishihara, K., 1996. Soil Behaviour in Earthquake Geotechnics. Clarenton Press, Oxford.
- 1147 Jaky, J., 1944. The coefficient of earth pressure at rest. J. Soc. Hung. Archit. Eng. 78, 355–
1148 358.
- 1149 Kim, B., Hashash, Y.M., Stewart, J.P., Rathje, E.M., Harmon, J.A., Musgrove, M.I.,
1150 Campbell, K.W., Silva, W.J., 2016. Relative Differences between Nonlinear and Equivalent-
1151 Linear 1-D Site Response Analyses. Earthq. Spectra 32, 1845–1865.

- 1152 Kwok, A.O., Stewart, J.P., Hashash, Y.M., 2008. Nonlinear ground-response analysis of
1153 Turkey Flat shallow stiff-soil site to strong ground motion. *Bull. Seismol. Soc. Am.* 98, 331–
1154 343.
- 1155 Kwok, A.O., Stewart, J.P., Hashash, Y.M., Matasovic, N., Pyke, R., Wang, Z., Yang, Z., 2007.
1156 Use of exact solutions of wave propagation problems to guide implementation of nonlinear
1157 seismic ground response analysis procedures. *J. Geotech. Geoenvironmental Eng.* 133, 1385–
1158 1398.
- 1159 Maeda, T., Sasatani, T., Takai, N., Shimizu, G., 2005. Azimuth estimation of KiK-net surface
1160 seismometers deployed in Hokkaido, Japan. *Geophys Bull Hokkaido Univ* 68, 141–152.
- 1161 Matsushima, S., Hirokawa, T., De Martin, F., Kawase, H., Sánchez-Sesma, F.J., 2014. The
1162 effect of lateral heterogeneity on horizontal-to-vertical spectral ratio of microtremors inferred
1163 from observation and synthetics. *Bull. Seismol. Soc. Am.*
- 1164 Menq, F., 2003. Dynamic properties of sandy and gravelly soils.
- 1165 Nakagawa, K., Soga, K., 1995. Nonlinear Cyclic Stress-Strain Relations of Soils. *Int. Conf.*
1166 *Recent Adv. Geotech. Earthq. Eng. Soil Dyn.* Paper 13.
- 1167 Noguera, S.M., 2016. Assessment and mitigation of liquefaction seismic risk: numerical
1168 modeling of their effects on SSI. *Université Paris-Saclay.*
- 1169 Olsen, K., Day, S., Bradley, C., 2003. Estimation of Q for long-period (> 2 sec) waves in the
1170 Los Angeles basin. *Bull. Seismol. Soc. Am.* 93, 627–638.
- 1171 Pagliaroli, A., Lanzo, G., Tommasi, P., Di Fiore, V., 2014. Dynamic characterization of soils
1172 and soft rocks of the Central Archeological Area of Rome. *Bull. Earthq. Eng.* 12, 1365–1381.
- 1173 Papa, V., Silvestri, F., Vinale, F., 1988. Analisi delle proprietà di un tipico terreno piroclastico

- 1174 mediante prove dinamiche di taglio semplice, in: I National Symposium on Research in
1175 Geotechnical Engineering. pp. 265–286.
- 1176 Régnier, J., Bonilla, L.-F., Bard, P.-Y., Bertrand, E., Hollender, F., Kawase, H., Sicilia, D.,
1177 Arduino, P., Amorosi, A., Asimaki, D., 2016a. International Benchmark on Numerical
1178 Simulations for 1D, Nonlinear Site Response (PRENOLIN): Verification Phase Based on
1179 Canonical Cases. *Bull. Seismol. Soc. Am.* 106, 2112–2135.
- 1180 Régnier, J., Bonilla, L.F., Bertrand, E., Semblat, J.-F., 2014. Influence of the VS Profiles
1181 beyond 30 m Depth on Linear Site Effects: Assessment from the KiK-net Data. *Bull. Seismol.*
1182 *Soc. Am.* 104, 2337–2348.
- 1183 Régnier, J., Cadet, H., Bard, P.-Y., 2016b. Empirical Quantification of the Impact of Nonlinear
1184 Soil Behavior on Site Response. *Bull. Seismol. Soc. Am.* 106, 1710–1719.
- 1185 Régnier, J., Cadet, H., Bonilla, L.F., Bertrand, E., Semblat, J.-F., 2013. Assessing Nonlinear
1186 Behavior of Soils in Seismic Site Response: Statistical Analysis on KiK-net Strong-Motion
1187 Data. *Bull. Seismol. Soc. Am.* 103, 1750–1770.
- 1188 Roblee, C., Chiou, B., 2004. A proposed Geindex model for design selection of non-linear
1189 properties for site response analysis, in: International Workshop on Uncertainties in Nonlinear
1190 Soil Properties and Their Impact on Modeling Dynamic Soil Response. PEER Headquarters,
1191 UC Berkeley. pp. 18–19.
- 1192 Rollins, K.M., Evans, M.D., Diehl, N.B., III, W.D.D., 1998. Shear modulus and damping
1193 relationships for gravels. *J. Geotech. Geoenvironmental Eng.* 124, 396–405.
- 1194 Roten, D., Fäh, D., Bonilla, L.F., 2013. High-frequency ground motion amplification during
1195 the 2011 Tohoku earthquake explained by soil dilatancy. *Geophys. J. Int.* 193, 898–904.

- 1196 Santisi d'Avila, M.P., Semblat, J.-F., 2014. Nonlinear seismic response for the 2011 Tohoku
1197 earthquake: borehole records versus one-directional three-component propagation models.
1198 *Geophys. J. Int.* 197, 566–580.
- 1199 Sato, K., Kokusho, T., Matsumoto, M., Yamada, E., 1996. Nonlinear seismic response and soil
1200 property during strong motion. *Soils Found.* 41–52.
- 1201 Seed, H., 1969. 1. M. Idriss, Influence of soil conditions on ground motions during
1202 earthquakes, *J. Soil Mech Found Div Amer Soc Civ Eng* 95.
- 1203 Senetakis, K., Anastasiadis, A., Ptilakis, K., Coop, M.R., 2013. The dynamics of a pumice
1204 granular soil in dry state under isotropic resonant column testing. *Soil Dyn. Earthq. Eng.* 45,
1205 70–79.
- 1206 Stewart, J., Kwok, A., 2009. Nonlinear Seismic Ground Response Analysis: Protocols and
1207 Verification Against Array Data. *PEER Annu. Meet. San Franc.-Present.* 84.
- 1208 Stewart, J.P., 2008. Benchmarking of nonlinear geotechnical ground response analysis
1209 procedures. Pacific Earthquake Engineering Research Center.
- 1210 Stewart, J.P., Afshari, K., Goulet, C.A., 2017. Non-Ergodic Site Response in Seismic Hazard
1211 Analysis. *Earthq. Spectra.* doi:10.1193/081716EQS135M
- 1212 Strasser, F.O., Abrahamson, N.A., Bommer, J.J., 2009. Sigma: Issues, insights, and
1213 challenges. *Seismol. Res. Lett.* 80, 40–56.
- 1214 Taborda, R., López, J., Karaoglu, H., Urbanic, J., Bielak, J., 2010. Speeding up finite element
1215 wave propagation for large-scale earthquake simulations. *Parallel Data Lab. Tech Rept*
1216 *CMUPDL-10 109.*
- 1217 Tatsuoka, F., Kohata, Y., Pesti, D.L., 1995. Deformation characteristics of soils and soft rocks

1218 under monotonic and cyclic loads and their relationships.

1219 Thompson, E.M., Baise, L.G., Tanaka, Y., Kayen, R.E., 2012. A taxonomy of site response
1220 complexity. *Soil Dyn. Earthq. Eng.* 41, 32–43.

1221 Thomson, W.T., 1950. Transmission of elastic waves through a stratified solid. *J. Appl. Phys.*
1222 21, 89–93.

1223 Verrucci, L., Lanzo, G., Tommasi, P., Rotonda, T., 2015. Cyclic and dynamic behaviour of a
1224 soft pyroclastic rock. *Géotechnique* 65, 359–373.

1225 Vucetic, M., Dobry, R., 1991. Effect of soil plasticity on cyclic response. *J. Geotech. Eng.*
1226 117.

1227 Vucetic, M., Dobry, R., 1988. Cyclic triaxial strain-controlled testing of liquefiable sands, in:
1228 *Advanced Triaxial Testing of Soil and Rock*. ASTM International.

1229 Yee, E., Stewart, J.P., Tokimatsu, K., 2013. Elastic and large-strain nonlinear seismic site
1230 response from analysis of vertical array recordings. *J. Geotech. Geoenvironmental Eng.* 139,
1231 1789–1801.

1232 Yoshida, N., Iai, S., 1998. Nonlinear site response and its evaluation and prediction, in: *Proc.*
1233 *2nd International Symposium on the Effect of Surface Geology on Seismic Motion*. pp. 71–
1234 90.

1235 Yu, G., Anderson, J.G., Siddharthan, R., 1993. On the characteristics of nonlinear soil
1236 response. *Bull. Seismol. Soc. Am.* 83, 218–244.

1237 Zeghal, M., Elgamal, A.-W., Tang, H.T., Srepp, J.C., 1995. Lotung downhole array. II:
1238 Evaluation of soil nonlinear properties. *J. Geotech. Eng.* 121, 363–378.

- 1239 Zhang, R.R., 2006. Characterizing and quantifying earthquake-induced site nonlinearity. *Soil*
1240 *Dyn. Earthq. Eng.* 26, 799–812.
- 1241
- 1242

1243 **List of captions**

1244 Figure 1: Location of the two selected sites for the validation phase with location of the
1245 epicenter of the selected events at each site according to their magnitude and surface
1246 PGA (cm/s^2 at the station)

1247 Figure 2: The graphs (a) and (d) show the initial Vs profile available at the selected sites
1248 for KSRH10 and Sendai. Graphs (b) and (e) illustrates the comparison between 1-D
1249 linear site response computed with empirical site response (surface to within motion
1250 spectral ratio) calculated with weak motion (PGA at the surface lower than 25 cm/s^2) for
1251 KSRH10 and Sendai sites. Graphs (c) and (f) compares the empirical transfer function of
1252 weak motions with the strongest ones recoded at KSRH10 and Sendai respectively.

1253 Figure 3: Location of the vertical arrays with respect to the borings for soil parameter
1254 measurements and MASW lines (a) for KSRH10 site and (b) for Sendai site.

1255 Figure 4: Modification of the Vs profile with improvements of the surface to within
1256 spectral ratio with 1-D linear site response analysis. Graphs (a) and (c): the dashed lines
1257 represent the initial Vs profile and the plain line the final Vs profile at KSRH10 and
1258 Sendai. Graphs (b) and (d): The dashed lines represent the 1-D linear numerical surface
1259 to within spectral ratio with the initial Vs profile and the plain line with the final.

1260 Figure 5: Input parameters for the numerical simulations at KSRH10 site. (a) Vs and
1261 elastic attenuation (ξ_0) profiles. The graph (b) illustrates, in the soil layer down to the
1262 depth where non-linear soil behavior is defined, the location of the shear modulus decay
1263 and attenuation ($G/G_{\max}(Y)$ and $\xi(Y)$) curves for the soil column 1 (SC1), for the soil
1264 column 2 (SC2) and for soil column 3 (SC3) shown in graph (d). For SC3, the locations of

1265 G/G_{\max} and damping curves in the soil layers are similar as for SC2. Graph (c) indicates
1266 the shear strength profile down to 40m.

1267 Figure 6: Input parameters for the numerical simulations at Sendai site. (a) V_s and
1268 elastic attenuation (ξ_0) profiles. The graph (b) illustrates, in the soil layer down to the
1269 depth where non-linear soil behavior is defined, the location of the shear modulus decay
1270 and attenuation ($G/G_{\max}(Y)$ and $\xi(Y)$) curves for the soil column 1 (SC1) and for the soil
1271 column 2 (SC2) shown in graph (c).

1272 Figure 7: Distance between the recorded and computed surface pseudo-response
1273 spectra (Misfit) compared to the code-to-code variability (σ_{c2c}) at Sendai site, using the
1274 soil columns SC1 and SC2 for the input motions TS-1-S, TS-3-S, TS-5-S and TS-9-S and at
1275 KSRH10 using the soil columns SC1, SC2 and SC3 for the input motions TS-0-K, TS-1-K,
1276 TS-2-K, TS-4-K and TS-8-K.

1277 Figure 8: Standard deviation values of the logarithm results (PGA, spectra acceleration
1278 at 3 periods) for the verification phase on canonical cases and for the validation phase of
1279 PRENOLIN project.

1280 Figure 9: Logic tree for propagation of the epistemic uncertainty.

1281 Figure 10: Comparison of the empirical surface to within spectral ratio of the East-West
1282 of the input motion TS-1-S and TS-8-S recorded at Sendai with the envelope of the
1283 results represented by the 25 and 75 percentiles of all numerical computations using
1284 SC1 or SC2 and only the EW component.

1285 Figure 11: Comparison of the surface response spectra of the East-West components of
1286 the input motion TS-1-S and TS-8-S recorded at Sendai with the envelope represented of
1287 the 25 and 75 percentiles of all numerical computations using SC1, and SC2.

1288 Figure 12 Comparison of the residuals and associated standard deviation of the surface
1289 response spectra of the East-West component of the input motion TS-1-S, TS-2-S, TS-5-S
1290 and TS-8-S recorded at Sendai with the envelope represented by the 25 and 75
1291 percentiles of all numerical computations using SC1, and SC2.

1292 Figure 12: Idem Figure 10. For KSRH10, for the input motions TS-1-K and TS-9-K and
1293 using the soil columns SC1, SC2 and SC3 for the north-south components.

1294 Figure 13: Idem Figure 11. For KSRH10, for the North-South component of the input
1295 motions TS-1-K and TS-9-K and using the soil columns SC1, SC2 and SC3.

1296 Figure 14: Idem Figure 12. For KSRH10, for the North-South component of the input
1297 motions TS-0-K, TS-1-K, TS-2-K, TS-4-K and TS-9-K and using the soil columns SC1, SC2
1298 and SC3.

1299 Figure 15 Idem Figure 12. For KSRH10, for the North-South component of the input
1300 motions TS-0-K, TS-1-K, TS-2-K, TS-4-K and TS-9-K and using the soil columns SC1, SC2
1301 and SC3.

1302

1303 **TABLES**

1304

Table 1: Selected event characteristics (PGA for EW components)

	EQ	CodeName	Fs* (Hz)	Mw†	Depth‡ (km)	Depi§ (km)	PGA _{borhole} ** (cm/s ²)	PGA _{surface} †† (cm/s ²)	Fc‡‡ (Hz)
KSRH10	KSRH100309260450	TS-0-K	200	8	42	180	110	558	6,6
	KSRH100411290332	TS-1-K	200	7,1	48	32	81	319	4,8
	KSRH100412062315	TS-2-K	200	6,9	46	44	69	386	4,2
	KSRH100411290336	TS-3-K	200	6	46	37	64	199	6,0
	KSRH100404120306	TS-4-K	200	5,8	47	43	27	162	5,3
	KSRH100904282021	TS-5-K	100	5,4	38	69	25	163	4,0
	KSRH100501182309	TS-6-K	200	6,4	50	38	25	125	6,7
	KSRH100912280913	TS-7-K	100	5	85	39	9	58	6,5
	KSRH100805110324	TS-8-K	100	5,1	88	63	8	46	6,2
	KSRH100309291137	TS-9-K	200	6,5	43	105	7	54	4,6
Sendai	F-2958	TS-1-S	100	9	23,7	163	252	481	6,9
	F-1889	TS-2-S	100	7,1	72	81	62	244	9,0
	F-1932	TS-3-S	100	6,4	11,9	19	61	208	10,3
	F-2691	TS-4-S	100	6,8	108,1	169	25	89	7,1
	F-3012	TS-5-S	100	5,9	30,7	96	25	72	7,5
	F-2659	TS-6-S	100	7.2	7.8	83	35	82	7.7
	F-1856	TS-7-S	100	5.9	41.2	95	12	32	7.8
	F-2862	TS-8-S	100	6.4	34.5	208	5	7	3.4
	F-2730	TS-9-S	100	5.8	47	176	3	12	6.2

1305

* Fs : Sampling frequency

† Moment Magnitude

‡ Hypocentral depth

§ Epicentral distance

** Peak Ground Acceleration at the down-hole station

†† Peak Ground Acceleration at surface station

‡‡ Central Frequency

1306

Table 2: Geological characteristics of the 2 selected sites with locations of the undisturbed soil samples.

Site	Down-hole sensor depth (m)	Max. complementary drilling depth (m)	Type of soil	Number of samples (location)
Sendai	8	10	Sand	2 (3.3 & 5.4 m)
KSRH10	250	50	Sand /clay	6 (3.5, 7.5, 14.5, 22.5, 29,7 & 34 m)

1307

1308

1309

1310

Table 3: Soil properties from the KSRH10 site

Z^* (m)	V_s^\dagger (m/s)	V_p (m/s)	ρ^\ddagger (kg/m ³)	Q_s^\S	ξ^{**}	Set of G/G_{max} and damping curves	$\tau_{max}^{\dagger\dagger}$ (kPa)
6	140	1520	1800	25	0.02	SC1-1,SC2-1,SC3-1	Calculated every 1m. according to Eq 6
11	180	1650	1800	25	0.02	SC1-2,SC2-2,SC3-2	
15	230	1650	1500	25	0.02	SC1-3,SC2-3,SC3-3	
20	300	1650	1500	25	0.02	SC1-4,SC2-3,SC3-3	
24	250	1650	1600	25	0.02	SC1-5,SC2-4,SC3-4	
28	370	1650	1600	25	0.02	SC1-6,SC2-5,SC3-5	
35	270	1650	1800	35	0.0142	SC1-7,SC2-5,SC3-5	
39	460	1650	1800	25	0.02	SC1-8,SC2-6,SC3-6	
44	750	1800	2500	75	0.0066	Linear	
84	1400	3400	2500	140	0.0035	Linear	
255	2400	5900	2500	240	0.0020	Linear	

1311

* Depth of the soil layer

† Shear wave velocity of the soil layer

‡ Density of the soil layer

§ Elastic Damping ratio

** Elastic attenuation

†† Shear strength

1312

1313

1314

Table 4: Soil properties from the Sendai site

Z (m)	V_s (m/s)	V_p (m/s)	ρ (kg/m ³)	Q_s	ξ	Set of G/G_{max} and damping curves
1	120	610	1850	25	0.02	SC1-1, SC2-1
2	170	870	1850	25	0.02	SC1-2, SC2-1
3	200	1040	1850	7.14	0.07	SC1-3, SC2-1
4	230	1180	1890	7.14	0.07	SC1-4, SC2-2
5	260	1300	1890	7.14	0.07	SC1-5, SC2-2
6	280	1420	1890	7.14	0.07	SC1-6, SC2-2
7	300	1530	1890	7.14	0.07	SC1-7, SC2-2
10.4	550	2800	2480	50	0.01	Linear

1315

1316

1317

1318 *Table 5: Standard deviation values of the residuals of the logarithm results for all teams and soil columns (PGA,*
1319 *spectra acceleration at 3 periods).*

	Sendai				KSRH10				
	TS-1-S	TS-2-S	TS-5-S	TS-8-S	TS-0-K	TS-1-K	TS-2-K	TS-4-K	TS-9
PGA	0.16	0.11	0.11	0.09	0.20	0.17	0.17	0.17	0.10
SA(0.1s)	0.10	0.10	0.12	0.10	0.23	0.22	0.23	0.20	0.15
SA(0.3s)	0.11	0.09	0.09	0.09	0.17	0.14	0.15	0.09	0.07
SA(1s)	0.10	0.08	0.09	0.09	0.11	0.06	0.07	0.07	0.11

1320

1321

1322 Mailing address:

1323

1324 • Julie Régnier, CEREMA, Julie Régnier, Cerema, Equipe-Projet MOUVGS, 500 routes des
1325 Lucioles, Sophia-Antipolis, F-06903, France.

1326 • Luis-Fabian Bonilla, IFSTTAR, 14-20 Boulevard Newton - Champs-sur-Marne - 77447
1327 Marne-la-Vallée Cedex 2, France

1328 • Pierre-Yves Bard, IFSTTAR and Université Grenoble Alpes ISTERre, CS 40700, 38058
1329 GRENOBLE Cedex 9, France

1330 • Etienne Bertrand, CEREMA, DTer Méditerranée, 56 Bd Stalingrad 06300 Nice, France

1331 • Fabrice Hollender, CEA, DEN, 13108 St Paul lez Durance, France

1332 • Hiroshi Kawase, DPRI, Gokasho,Uji,Kyoto 611-0011 Japan

1333 • Deborah Sicilia, EDF - DPI-CEIDRE, TEGG, 905 av du Camp Menthe,13097 Aix-en-
1334 Provence Cedex 2, France

1335 • Pedro Arduino, Department of Civil & Environmental Engineering, University of
1336 Washington, Seattle, WA, USA

1337 • Angelo Amorosi, Sapienza, University of Rome, Via Eudossiana 18, 00184 Roma, Italy

1338 • Domniki Asimaki, California Institute of Technology, Campus Address: 1200 E California
1339 blvd, Pasadena CA 91125, US

1340 • Daniela Boldini, University of Bologna, Dipartimento di Ingegneria Civile, Chimica,
1341 Ambientale e dei Materiali , Via Terracini 28, 40131 Bologna, Italy

1342 • Long Chen, Department of Civil & Environmental Engineering, University of Washington,
1343 Seattle, WA, USA

- 1344 • Anna Chiaradonna, Department of Civil, Architectural and Environmental Engineering,
1345 University of Napoli Federico II, via Claudio 21, 80125 Napoli, Italy
- 1346 • Florent DeMartin, BRGM (French Geological Survey), Direction of Risks and Prevention, 3
1347 Avenue Claude Guillemin, 45100 Orléans, France
- 1348 • Ahmed Elgamal, University of California, San Diego, Dept. of Structural Engineering, La
1349 Jolla, CA 92093-0085, USA
- 1350 • Gaetano Falcone, Technical University of Bari, Via Amendola 126, 70126 Bari, Italy
- 1351 • Evelyne Foerster, CEA, DEN/DM2S/SEMT/EMSI and SEISM Institute Paris-Saclay, 91191
1352 Gif-sur-Yvette Cedex, France
- 1353 • Sebastiano Foti, Politecnico di Torino, Corso Duca degli Abruzzi, 24 - 10129 Torino, Italy
- 1354 • Evangelia Garini, NTUA National Technical University of Athens, Faculty of Civil
1355 Engineering , Geotechnical Department, Iroon Polytechniou 9,Zografou 157 80, GREECE
- 1356 • George Gazetas, NTUA National Technical University of Athens, Faculty of Civil
1357 Engineering , Geotechnical Department, Iroon Polytechniou 9,Zografou 157 80, GREECE
- 1358 • Céline Gélis, IRSN, 31 Avenue de la Division Leclerc, 92260 Fontenay-aux-Roses, France
- 1359 • Alborz Ghofrani, Department of Civil & Environmental Engineering, University of
1360 Washington, Seattle, WA, USA
- 1361 • Amalia Giannakou, Fugro Sial, Esentepe mah. Yazarlar sok. No.16 34394 Gayrettepe,
1362 Şişli-İstanbul / Turkey
- 1363 • James R. Gingery, Hayward Baker Inc, 1870 Cordell Ct #201 El Cajon, CA 92020, US.
- 1364 • Nathalie Glinsky, CEREMA, DTer Méditerranée, 56 Bd Stalingrad 06300 Nice, France

- 1365 • Joseph Harmon, University of Illinois at Urbana-Champaign, 2230c Newmark Lab, 205 N
1366 Mathews, M/C 250, Urbana, IL 61801 , US
- 1367 • Youssef Hashash, University of Illinois at Urbana-Champaign, 2230c Newmark Lab, 205 N
1368 Mathews, M/C 250, Urbana, IL 61801 , US
- 1369 • Susumu Iai, Flip consortium, Jiji-Press Bld. 5th floor, 185 Nakahori-cho Nakagyo-ku,
1370 Kyoto 604-0844, Japan
- 1371 • Steve Kramer, 132 I More Hall, Department of Civil & Environmental Engineering,
1372 University of Washington, Seattle, WA, 98195-2700, US
- 1373 • Stavroula Kontoe, Imperial College, South Kensington Campus, London SW7 2AZ, UK.
- 1374 • Jozef Kristek, Comenius University Bratislava Faculty of Mathematics, Physics and
1375 Informatics Mlynská dolina F1 84248 Bratislava, Slovakia.
- 1376 • Giuseppe Lanzo, Sapienza University of Rome, Via A. Gramsci 53, 00197 Rome, Italy
- 1377 • Annamaria di Lernia, Politecnico of Bari, Via Amendola 126, Bari, Italy Italy
- 1378 • Fernando Lopez-Caballero, MSSMat, CNRS, CentraleSupélec, Paris-Saclay University,
1379 91190 Gif-Sur-Yvette, France.
- 1380 • Marianne Marot, CEREMA, DTer Méditerranée, 56 Bd Stalingrad 06300 Nice, France
- 1381 • Graeme McAllister, Department of Civil Engineering, University of British Columbia,
1382 Vancouver, BC, Canada.
- 1383 • E. Diego Mercerat, CEREMA, DTer Méditerranée, 56 Bd Stalingrad 06300 Nice, France
- 1384 • Peter Moczo Comenius University Bratislava Faculty of Mathematics, Physics and
1385 Informatics Mlynská dolina F1 84248 Bratislava, Slovakia.

- 1386 • Silvana Montoya-Noguera, MSSMat, CNRS, CentraleSupélec, Paris-Saclay University,
 1387 91190 Gif-Sur-Yvette, France. Current institution: Department of Civil Engineering,
 1388 Universidad EAFIT, Medellín, Colombia
- 1389 • Michael Musgrove, University of Illinois at Urbana-Champaign, 2230c Newmark Lab, 205
 1390 N Mathews, M/C 250, Urbana, IL 61801 , US
- 1391 • Alex Nieto-Ferro, Dépt. Analyses en Mécanique Avancée, EDF Lab Paris-Saclay, 7
 1392 boulevard Gaspard Monge, 91120 PALAISEAU
- 1393 • Alessandro Pagliaroli, University of Chieti-Pescara, viale Pindaro 42, 65129 Pescara, Italy.
- 1394 • Federico Passeri, Politecnico di Torino, Corso Duca degli Abruzzi, 24 - 10129 Torino, Italy
- 1395 • Aneta Richterova, Comenius University Bratislava Faculty of Mathematics, Physics and
 1396 Informatics Mlynská dolina F1 84248 Bratislava, Slovakia.
- 1397 • Suwal Sajana, Sapienza University of Rome, Via A. Gramsci 53, 00197 Rome, Italy
- 1398 • Maria Paola Santisi d'Avila, UNS, Nice, Campus Valrose, 28 avenue Valrose, 06108 Nice
 1399 cedex 2, France
- 1400 • Jian Shi, California Institute of Technology, Campus Address: 1200 E California blvd,
 1401 Pasadena CA 91125, US
- 1402 • Francesco Silvestri, Department of Civil, Architectural and Environmental Engineering,
 1403 University of Napoli Federico II, via Claudio 21, 80125 Napoli, Italy.
- 1404 • Mahdi Taiebat: Department of Civil Engineering, University of British Columbia,
 1405 Vancouver, BC, Canada
- 1406 • Giuseppe Tropeano, Department of Civil, Environmental Engineering and Architecture,
 1407 University of Cagliari, Piazza d'Armi 09123, Cagliari, Italy.

- 1408 • Didrik Vandeputte, EDF, A EDF – DIN CEIDRE / TEGG 905, avenue du Camp de
1409 Menthe 13097 AIX EN PROVENCE CEDEX 02
- 1410 • Luca Verrucci, Dipartimento di Ingegneria Strutturale e Geotecnica, University of Rome,
1411 via Eudossiana 18, 00184, Rome, Italy.

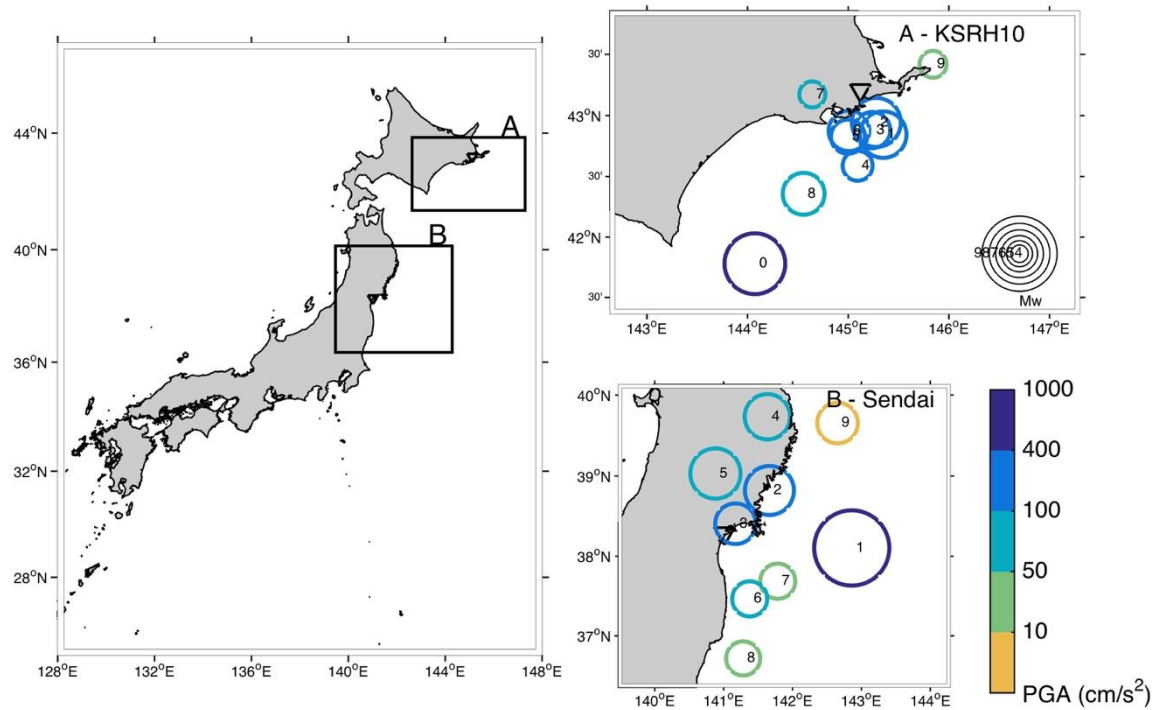


Figure 1: Location of the two selected sites for the validation phase with location of the epicenter of the selected events at each site according to their magnitude and surface PGA (cm/s² at the station)

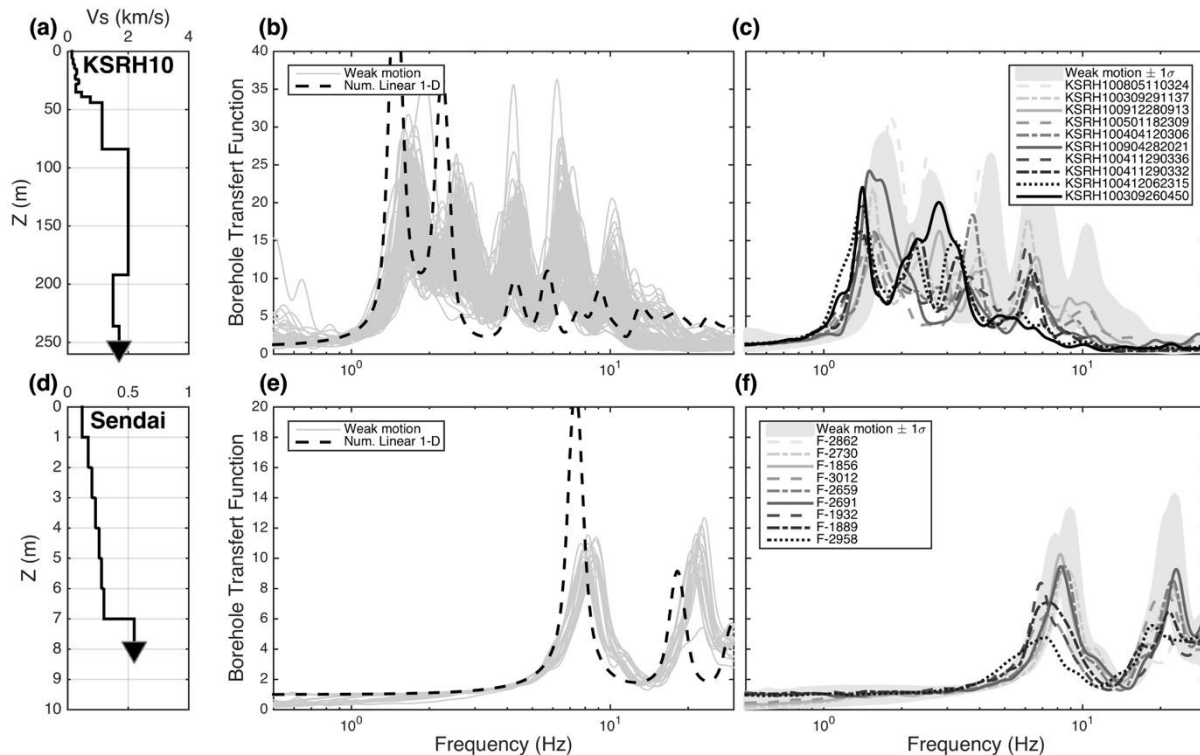


Figure 2: The graphs (a) and (d) show the initial Vs profile available at the selected sites for KSRH10 and Sendai. Graphs (b) and (e) illustrates the comparison between 1-D linear site response computed with empirical site response (surface to within motion spectral ratio) calculated with weak motion (PGA at the surface lower than 25 cm/s²) for KSRH10 and Sendai sites. Graphs (c) and (f) compares the empirical transfer function of weak motions with the strongest ones recorded at KSRH10 and Sendai respectively.

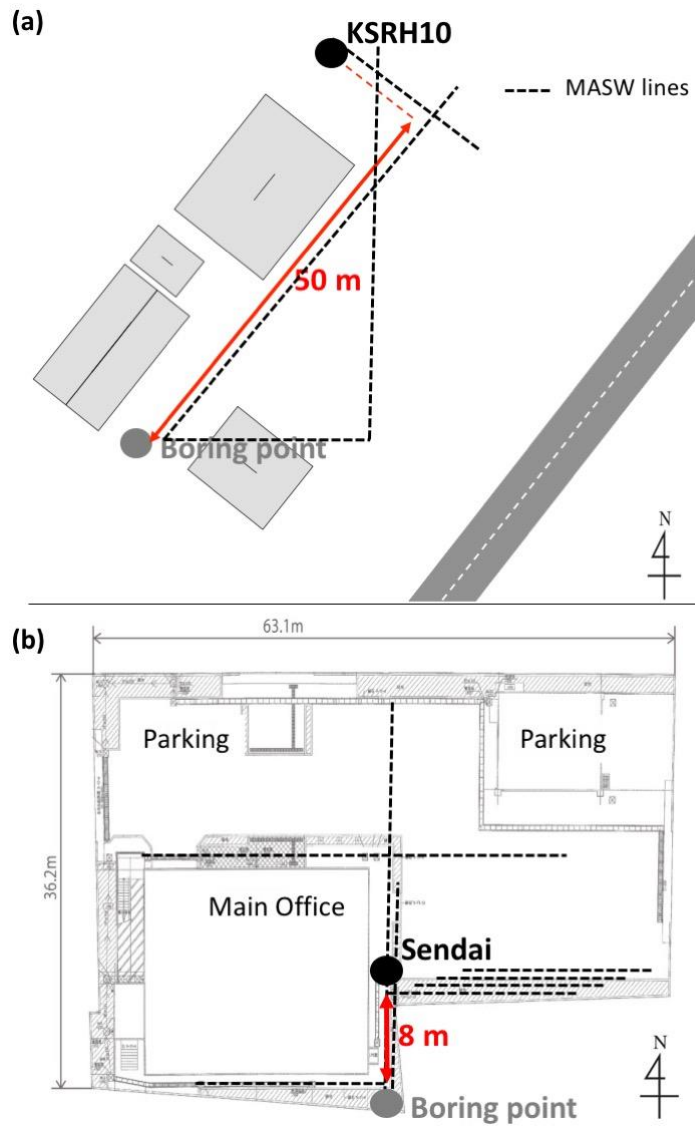


Figure 3: Location of the vertical arrays with respect to the borings for soil parameter measurements and MASW lines (a) for KSRH10 site and (b) for Sendai site.

Figure 4: Modification of the V_s profile with improvements of the surface to within spectral ratio with 1-D linear site response analysis. Graphs (a) and (c): the dashed lines represent the initial V_s profile and the plain line the final V_s profile at KSRH10 and Sendai. Graphs (b) and (d): The dashed lines represent the 1-D linear numerical surface to within spectral ratio with the initial V_s profile and the plain line with the final.

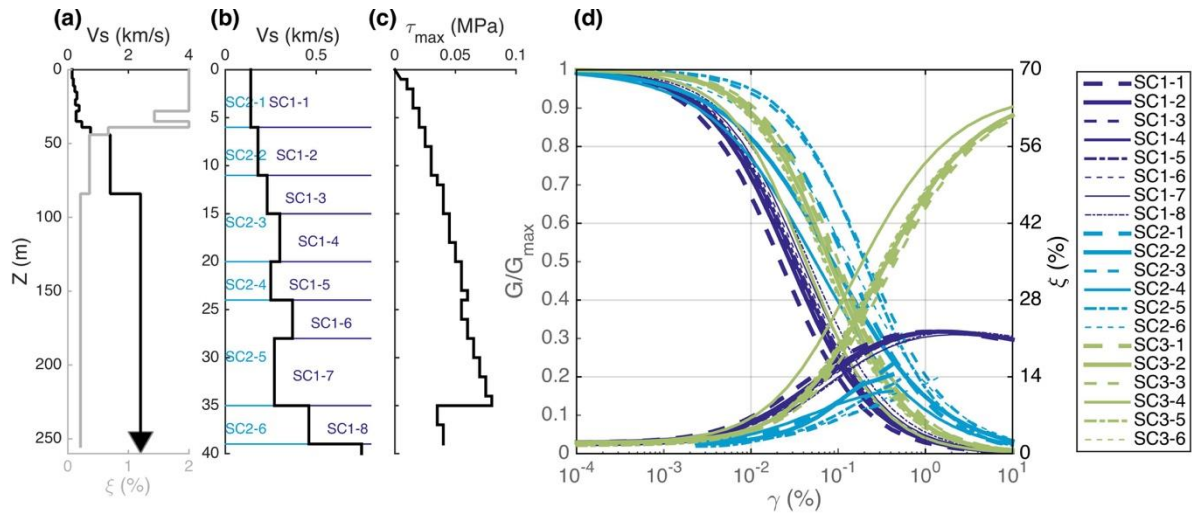


Figure 5: Input parameters for the numerical simulations at KSRH10 site. (a) Vs and elastic attenuation (ξ_0) profiles. The graph (b) illustrates, in the soil layer down to the depth where non-linear soil behavior is defined, the location of the shear modulus decay and attenuation ($G/G_{max}(\gamma)$ and $\xi(\gamma)$) curves for the soil column 1 (SC1), for the soil column 2 (SC2) and for soil column 3 (SC3) shown in graph (d). For SC3, the locations of G/G_{max} and damping curves in the soil layers are similar as for SC2. Graph (c) indicates the shear strength profile down to 40m.

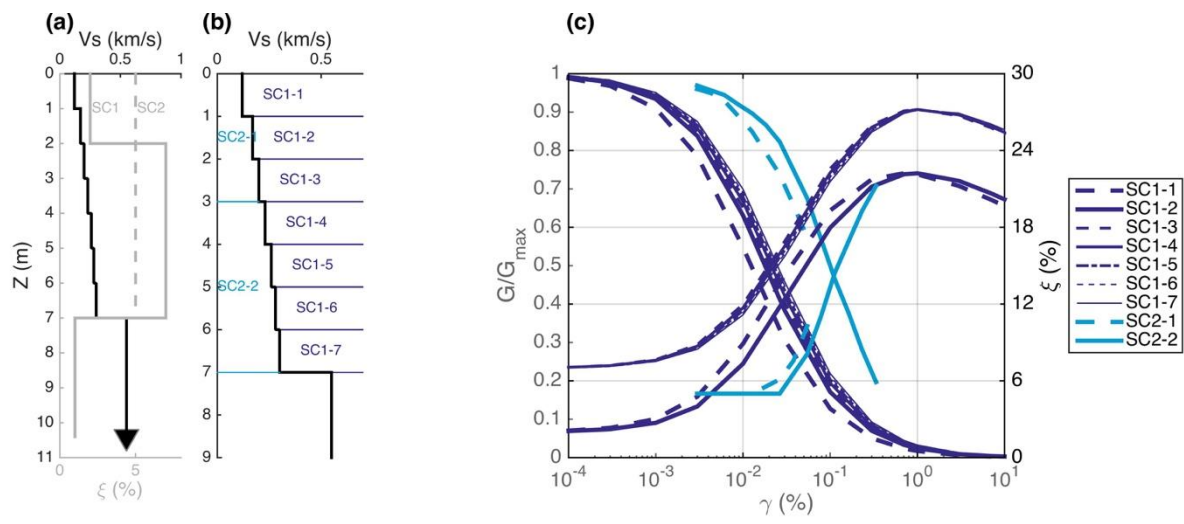


Figure 6: Input parameters for the numerical simulations at Sendai site. (a) Vs and elastic attenuation (ξ_0) profiles. The graph (b) illustrates, in the soil layer down to the depth where non-linear soil behavior is defined, the location of the shear modulus decay and attenuation ($G/G_{max}(\gamma)$ and $\xi(\gamma)$) curves for the soil column 1 (SC1) and for the soil column 2 (SC2) shown in graph (c).

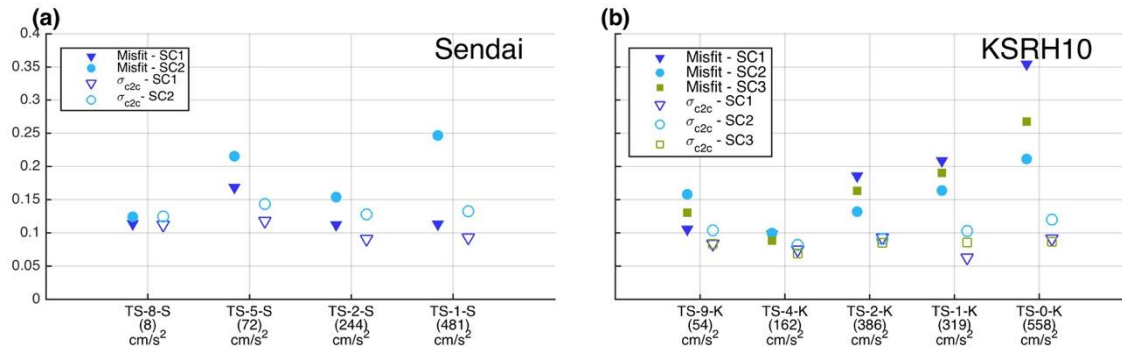


Figure 7: Distance between the recorded and computed surface pseudo-response spectra (Misfit) compare to the code-to-code variability (σ_{c2c}) at Sendai site, using the soil columns SC1 and SC2 for the input motions TS-1-S, TS-3-S, TS-5-S and TS-9-S and at KSRH10 using the soil columns SC1, SC2 and SC3 for the input motions TS-0-K, TS-1-K, TS-2-K, TS-4-K and TS-8-K.

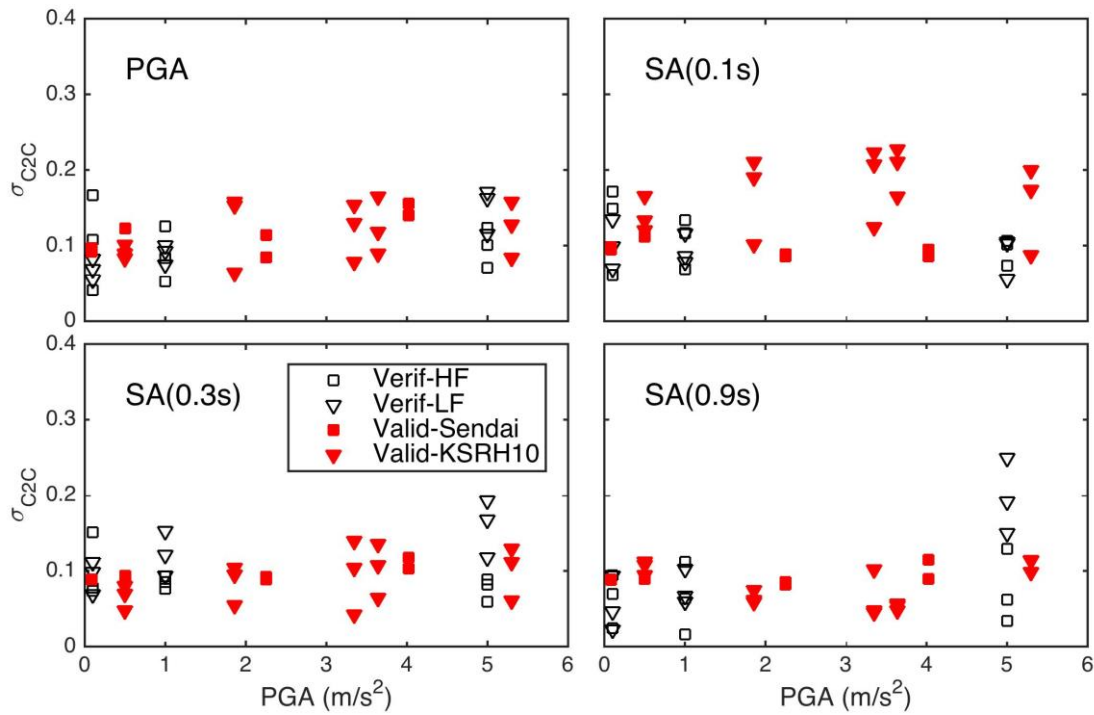


Figure 8: Standard deviation values of the logarithm results (PGA, spectra acceleration at 3 periods) for the verification phase on canonical cases and for the validation phase of PRENOLIN project.

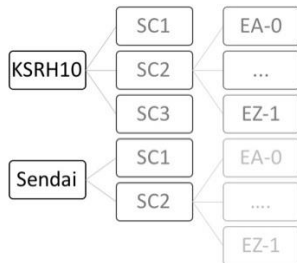


Figure 9: Logic tree for propagation of the epistemic uncertainty.

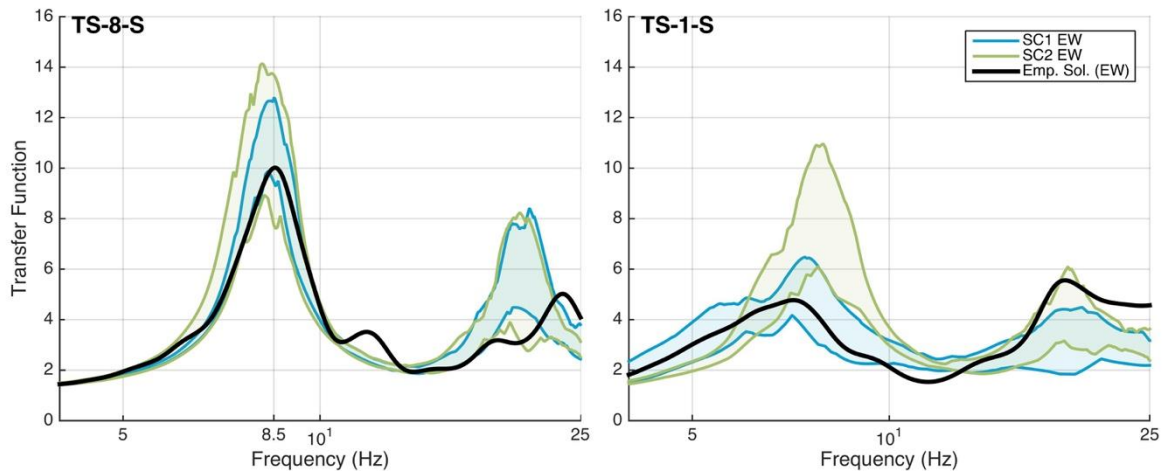


Figure 10: Comparison of the empirical surface to within spectral ratio of the East-West of the input motion TS-1-S and TS-8-S recorded at Sendai with the envelope of the results represented by the 25 and 75 percentiles of all numerical computations using SC1 or SC2 and only the EW component.

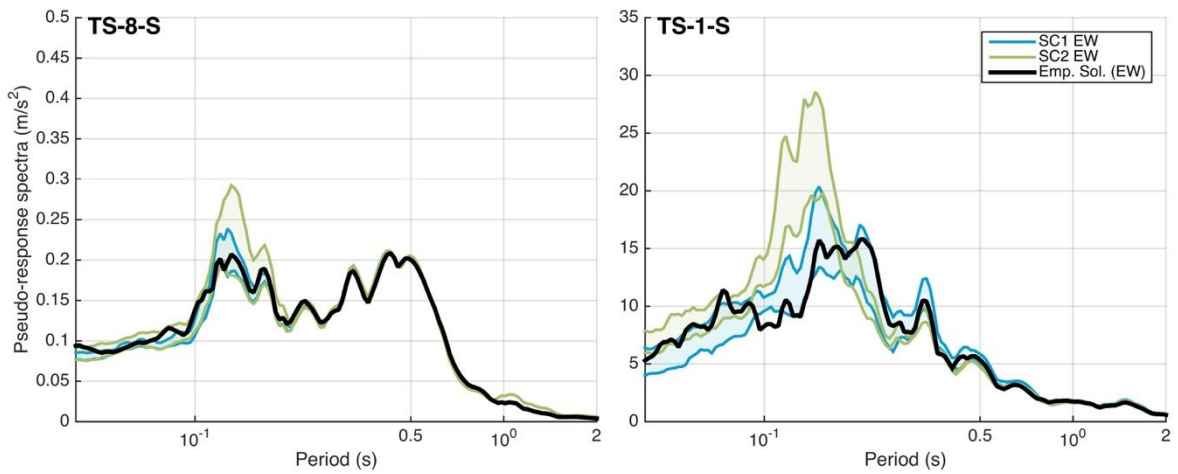


Figure 11: Comparison of the surface response spectra of the East-West components of the input motion TS-1-S and TS-8-S recorded at Sendai with the envelope represented of the 25 and 75 percentiles of all numerical computations using SC1, and SC2

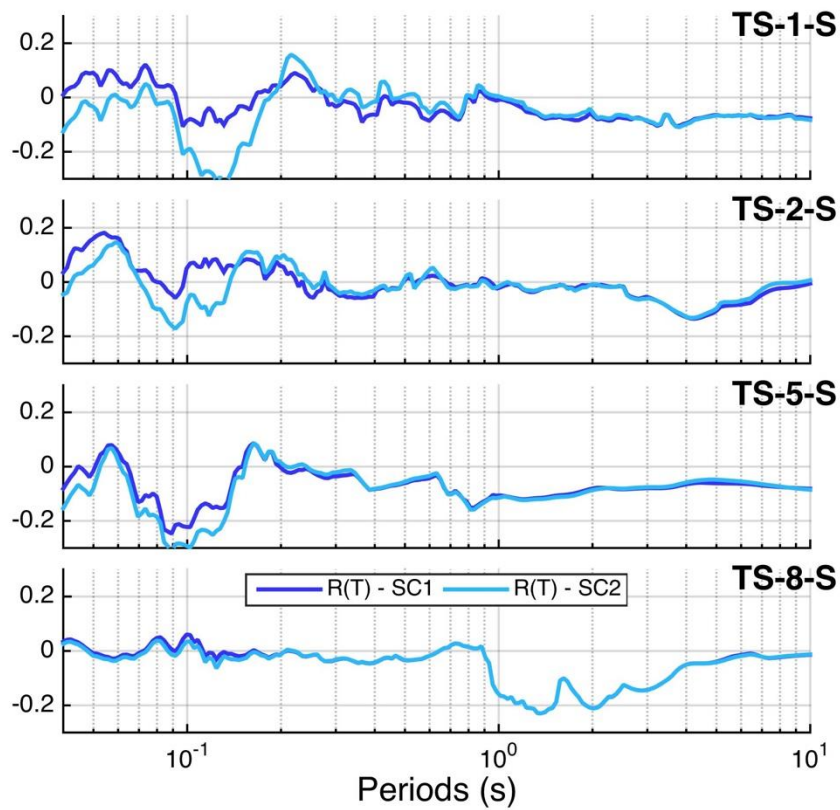


Figure 12: Comparison of the residuals and associated standard deviation of the surface response spectra of the East-West component of the input motion TS-1-S, TS-2-S, TS-5-S and TS-8-S recorded at Sendai with the envelope represented by the 25 and 75 percentiles of all numerical computations using SC1, and SC2.

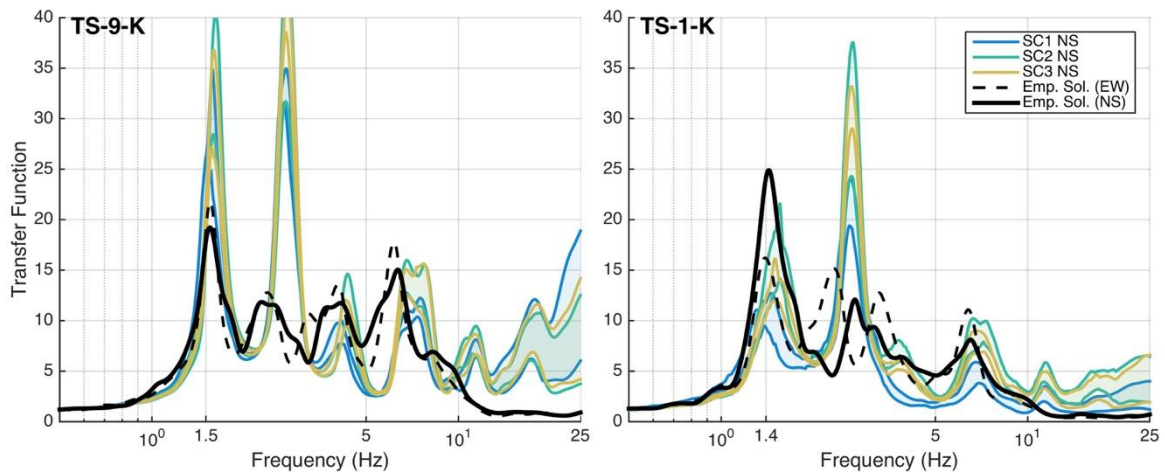


Figure 13: Idem Figure 10. For KSRH10, for the input motions TS-1-K and TS-9-K and using the soil columns SC1, SC2 and SC3 for the north-south and east-west components.

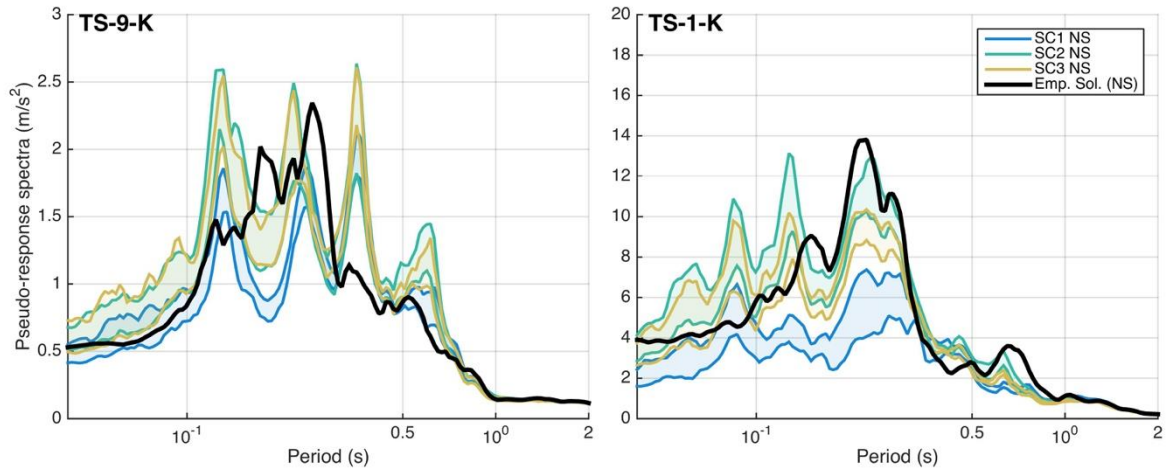


Figure 14 Idem Figure 11. For KSRH10, for the North-South component of the input motions TS-1-K and TS-9-K and using the soil columns SC1, SC2 and SC3.

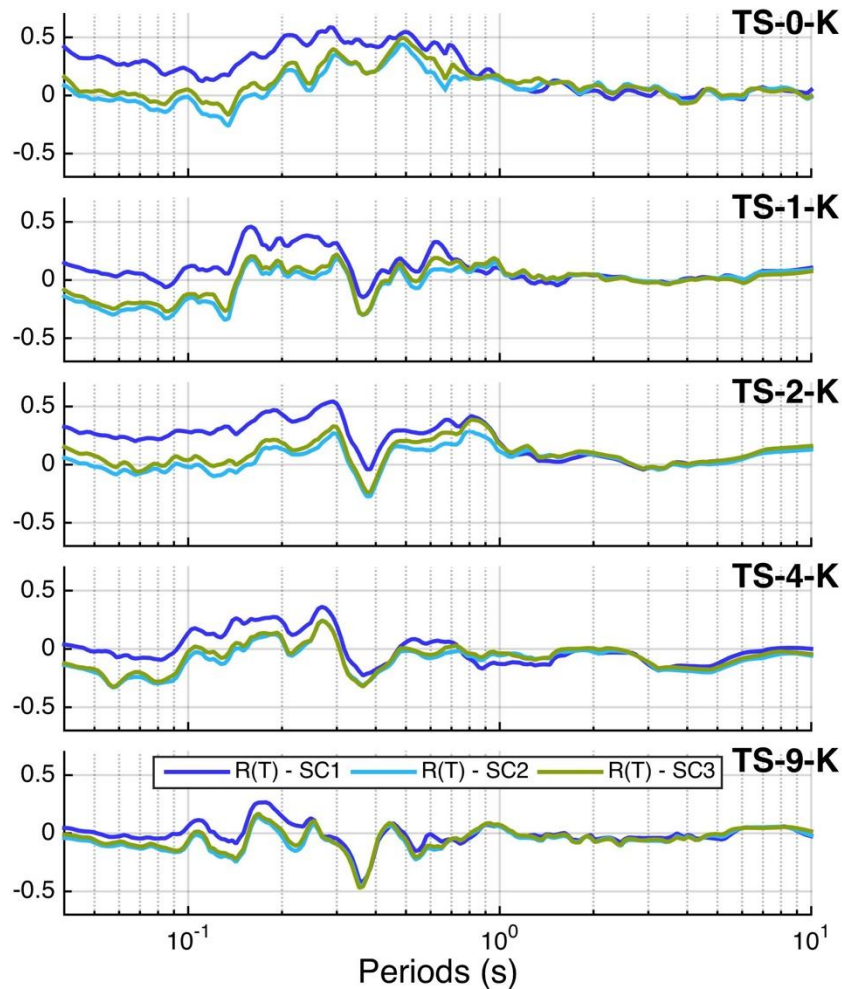
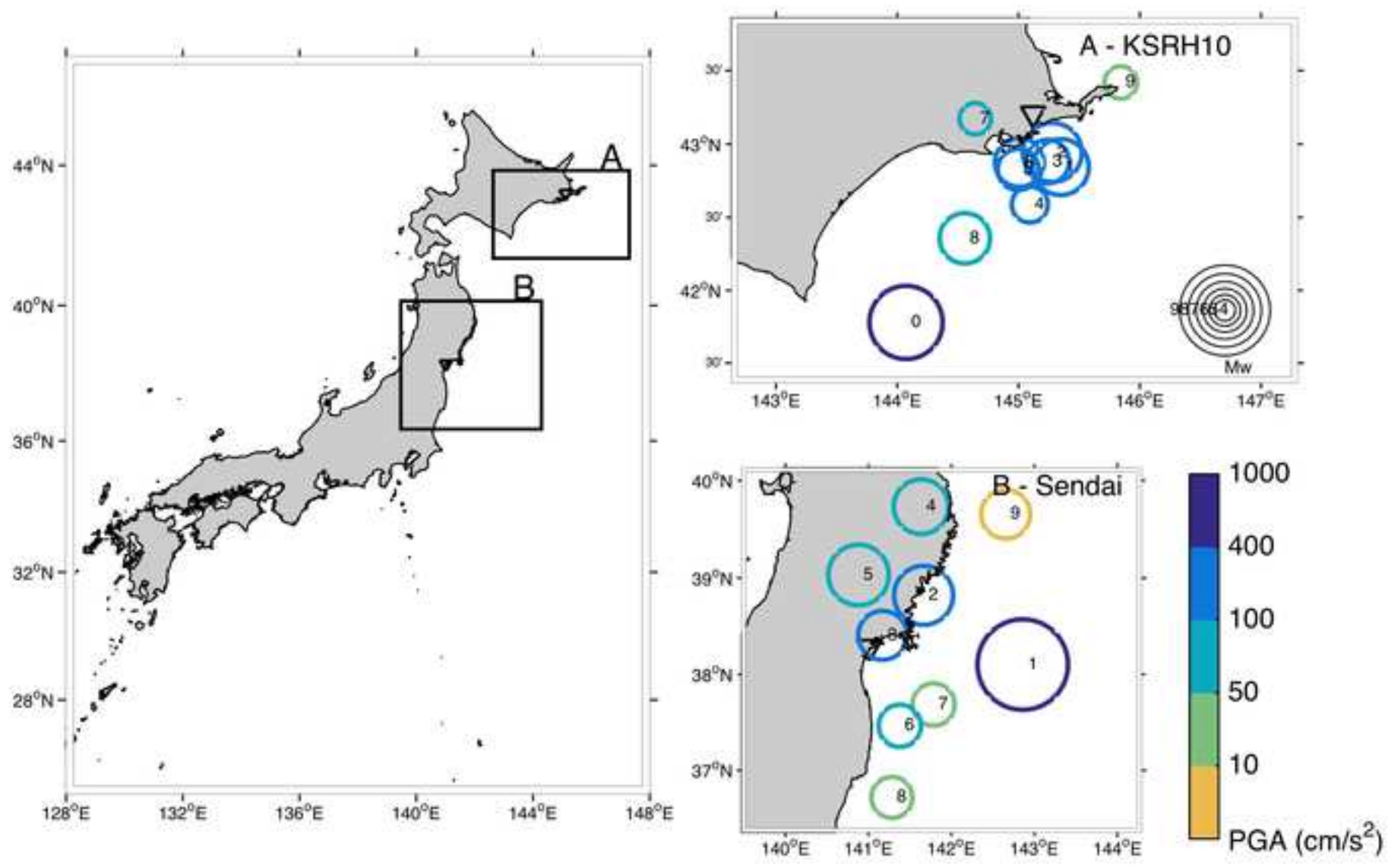
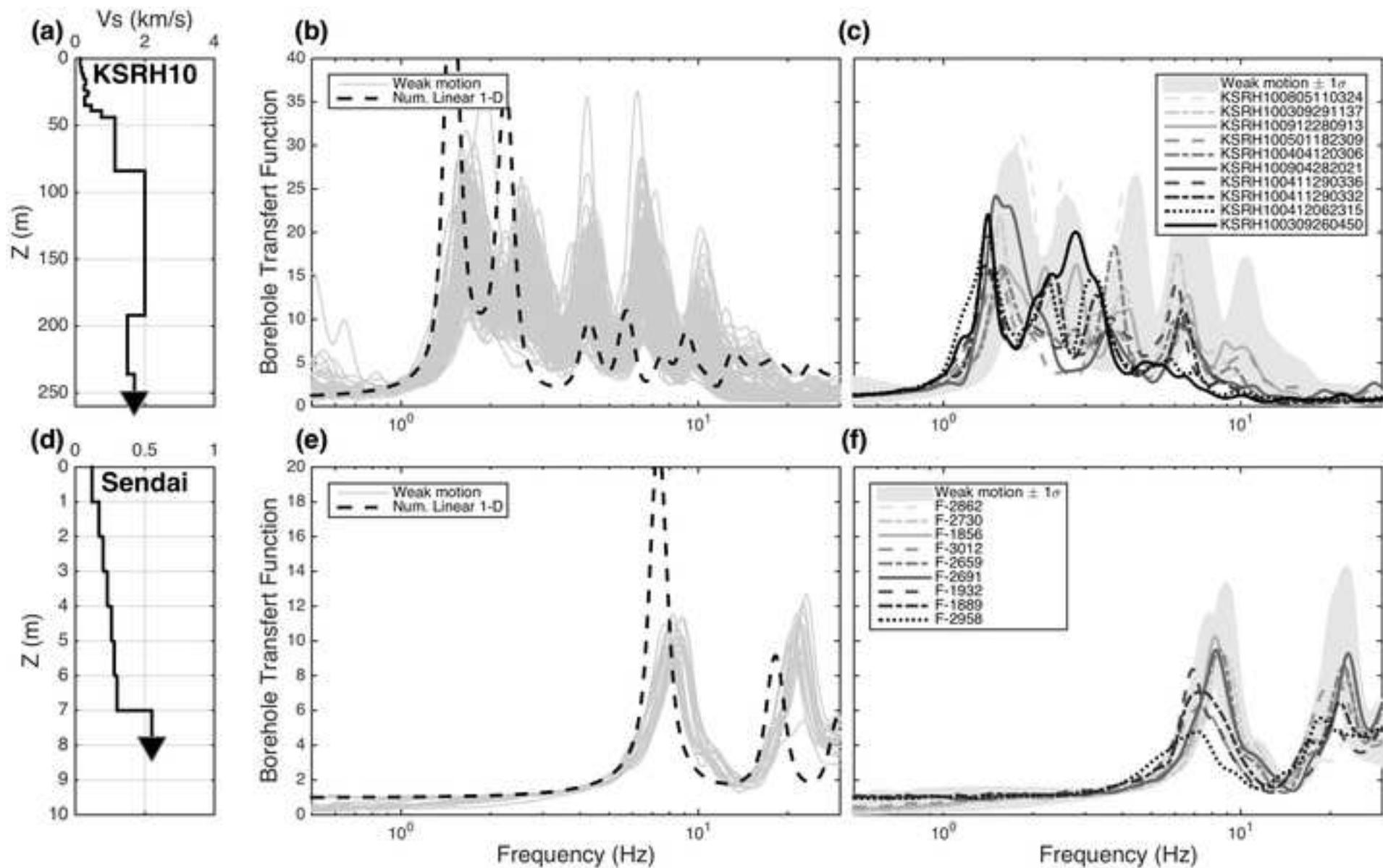


Figure 15 Idem Figure 12. For KSRH10, for the North-South component of the input motions TS-0-K, TS-1-K, TS-2-K, TS-4-K and TS-9-K and using the soil columns SC1, SC2 and SC3.

Figure 1





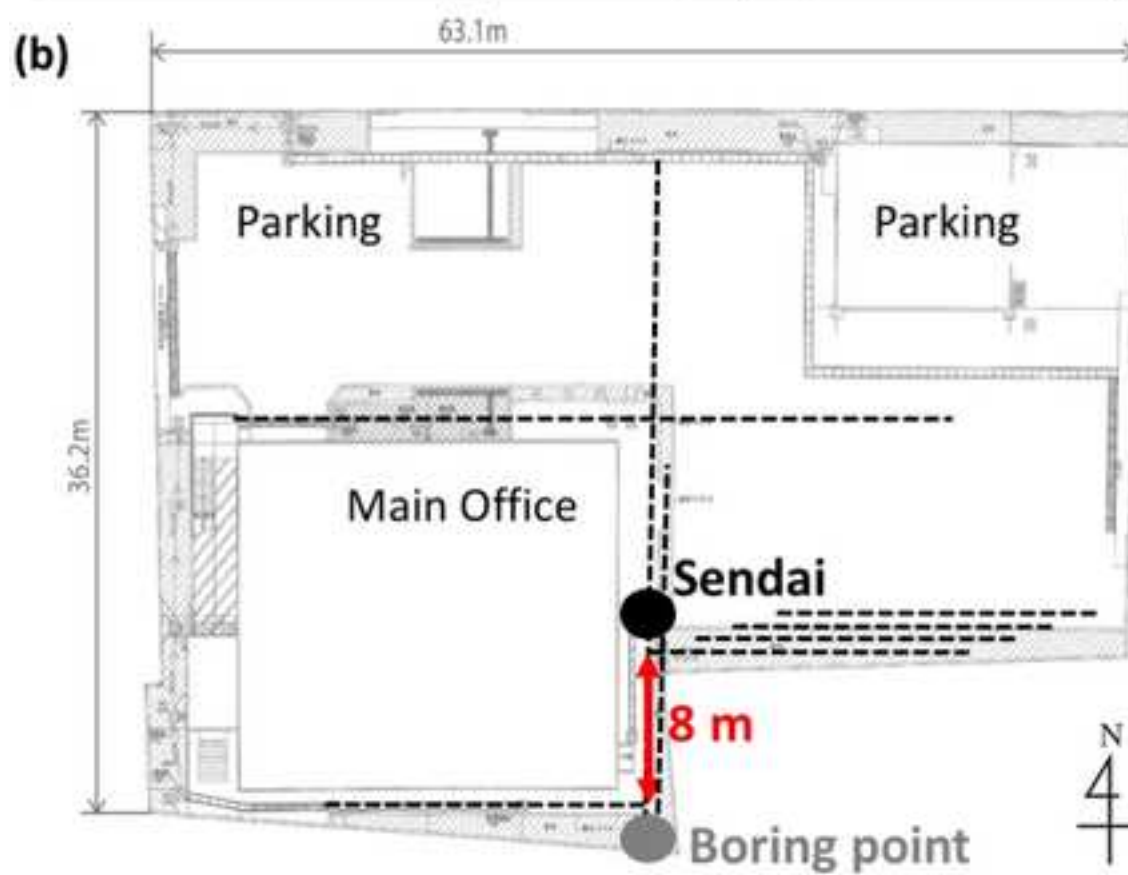
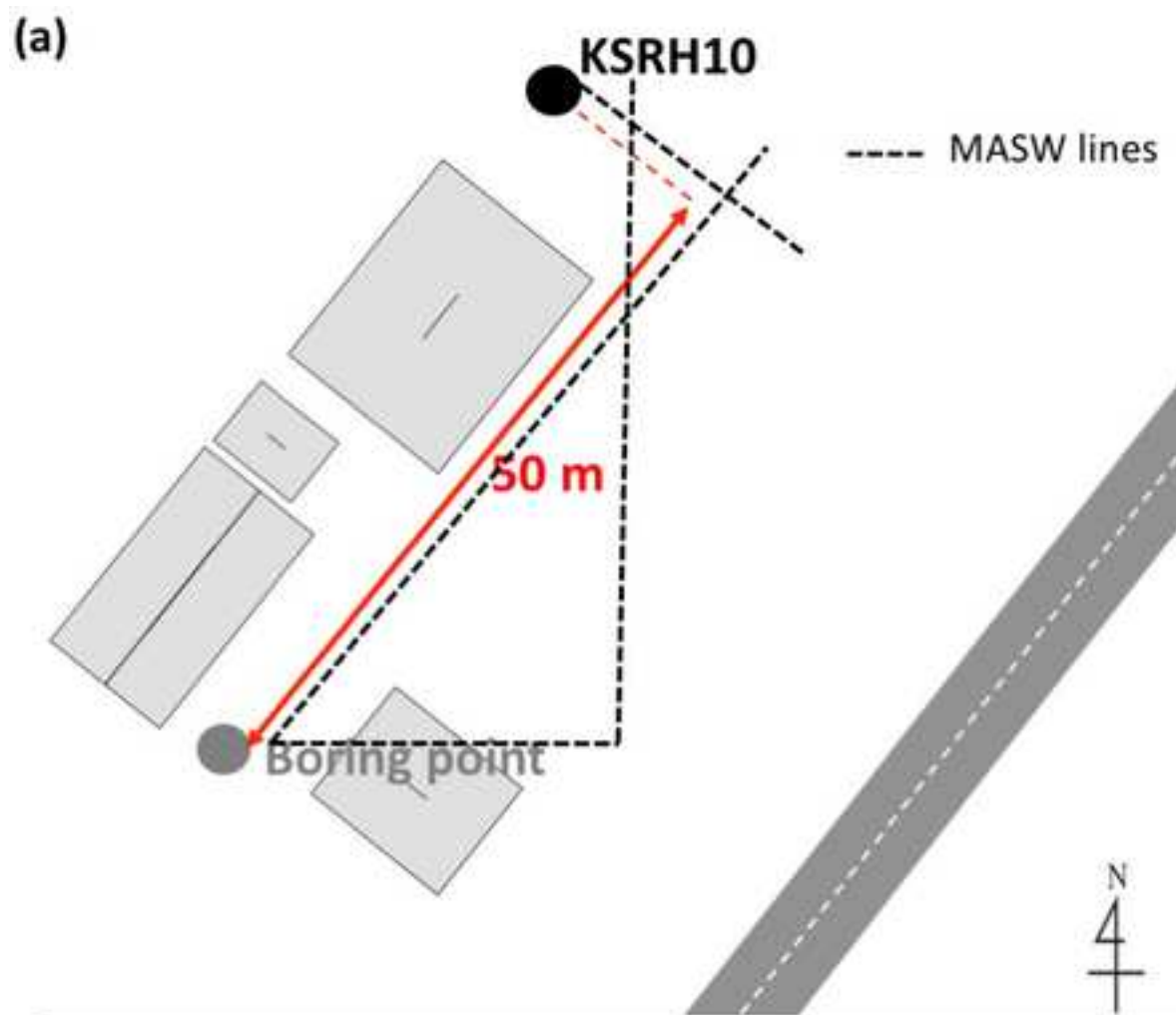


Figure 4

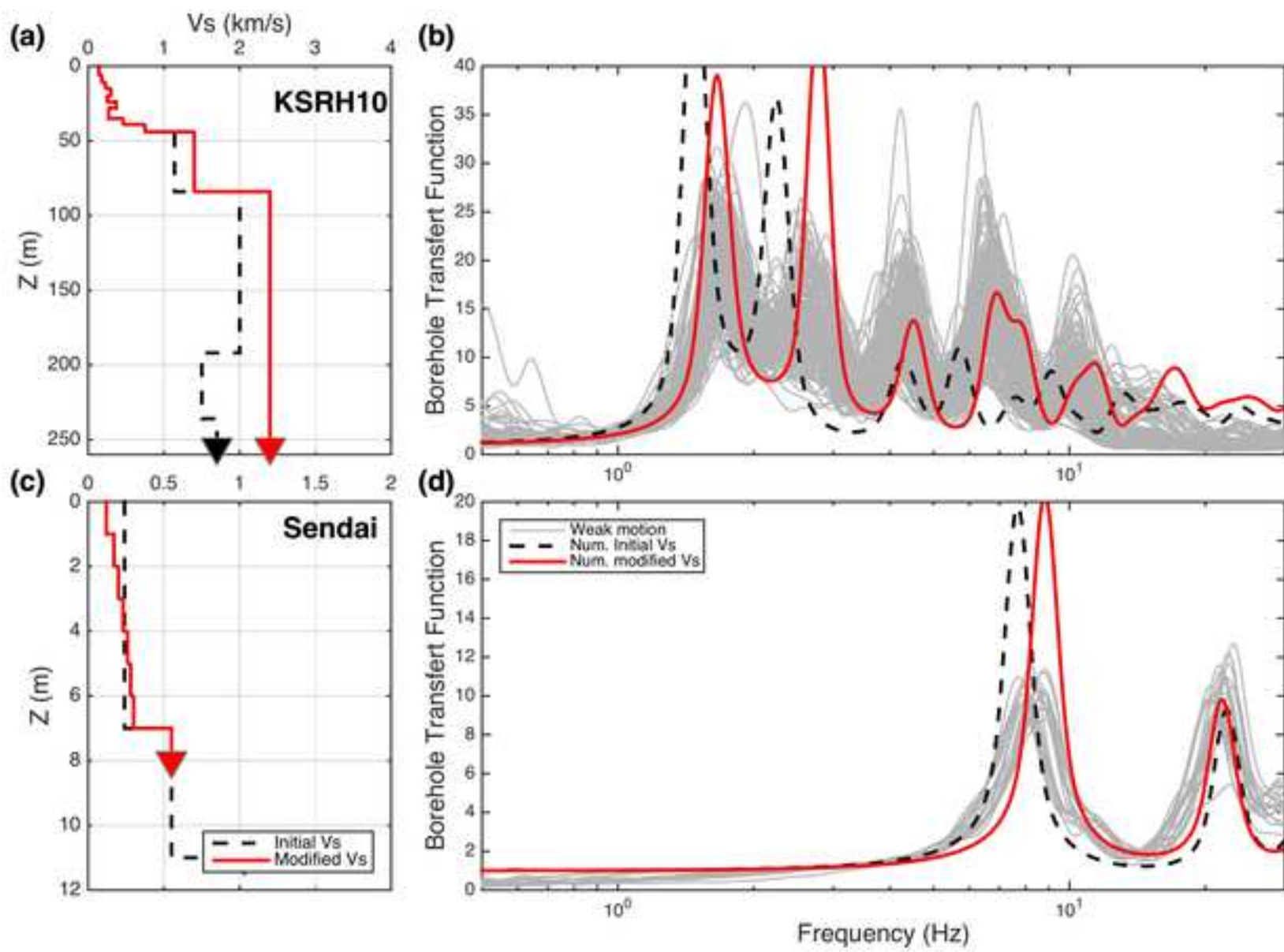
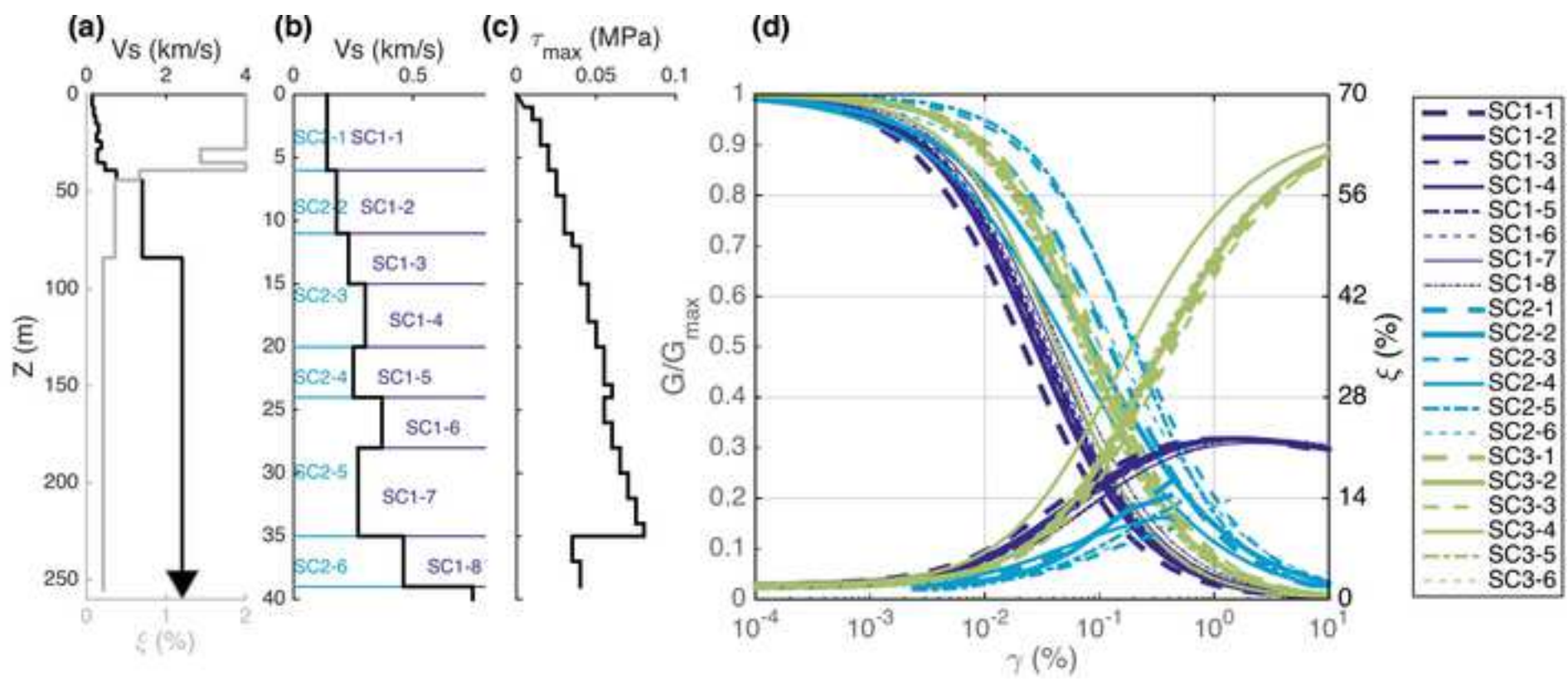
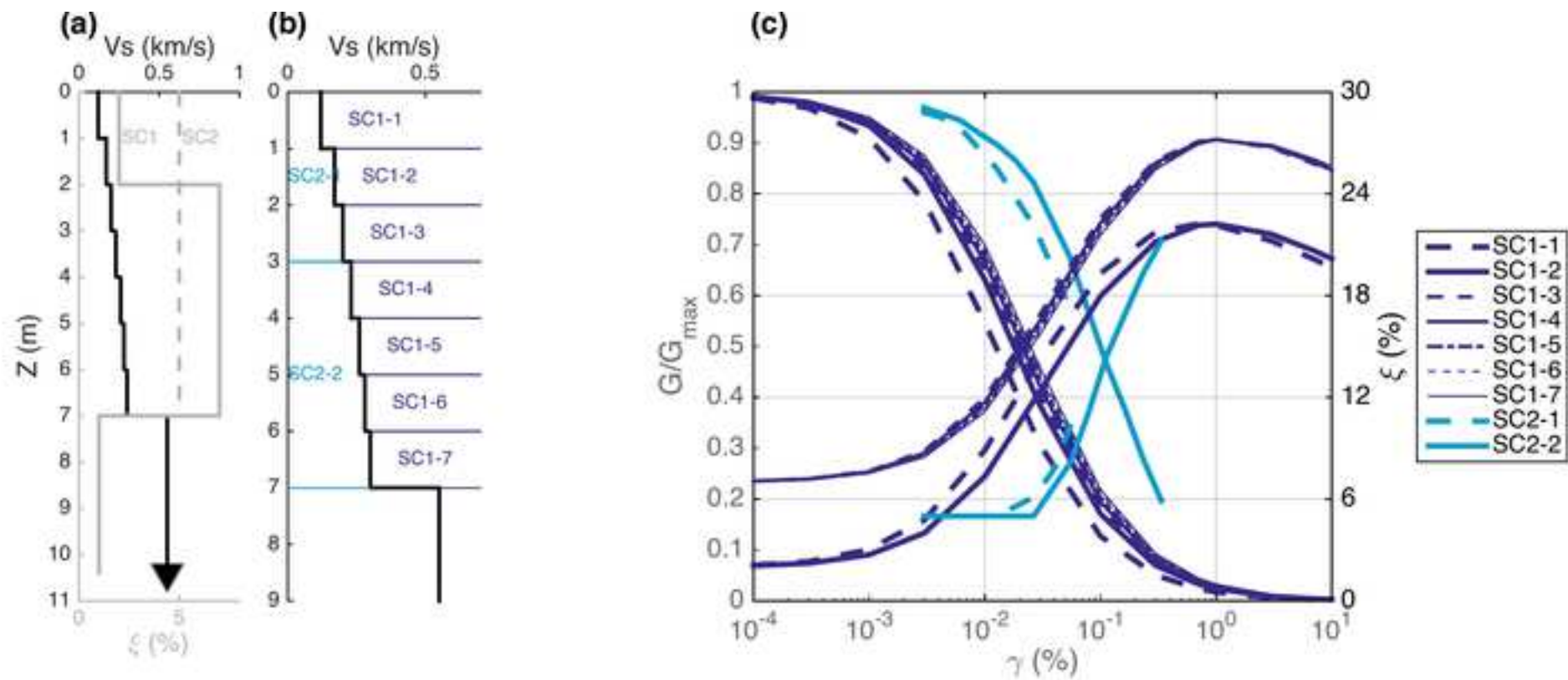
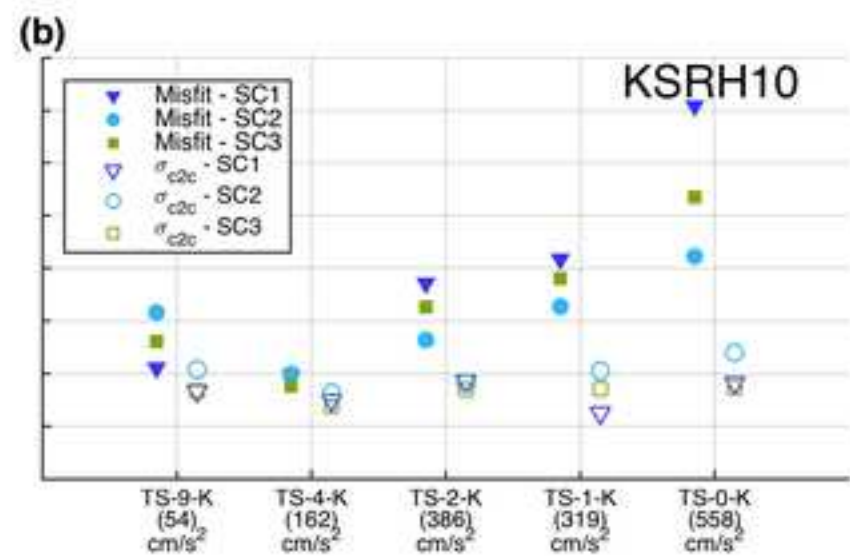
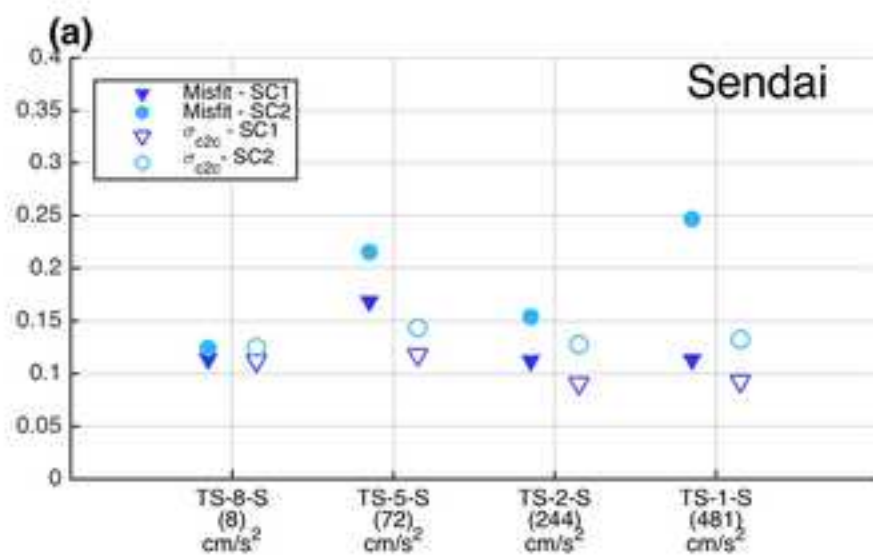
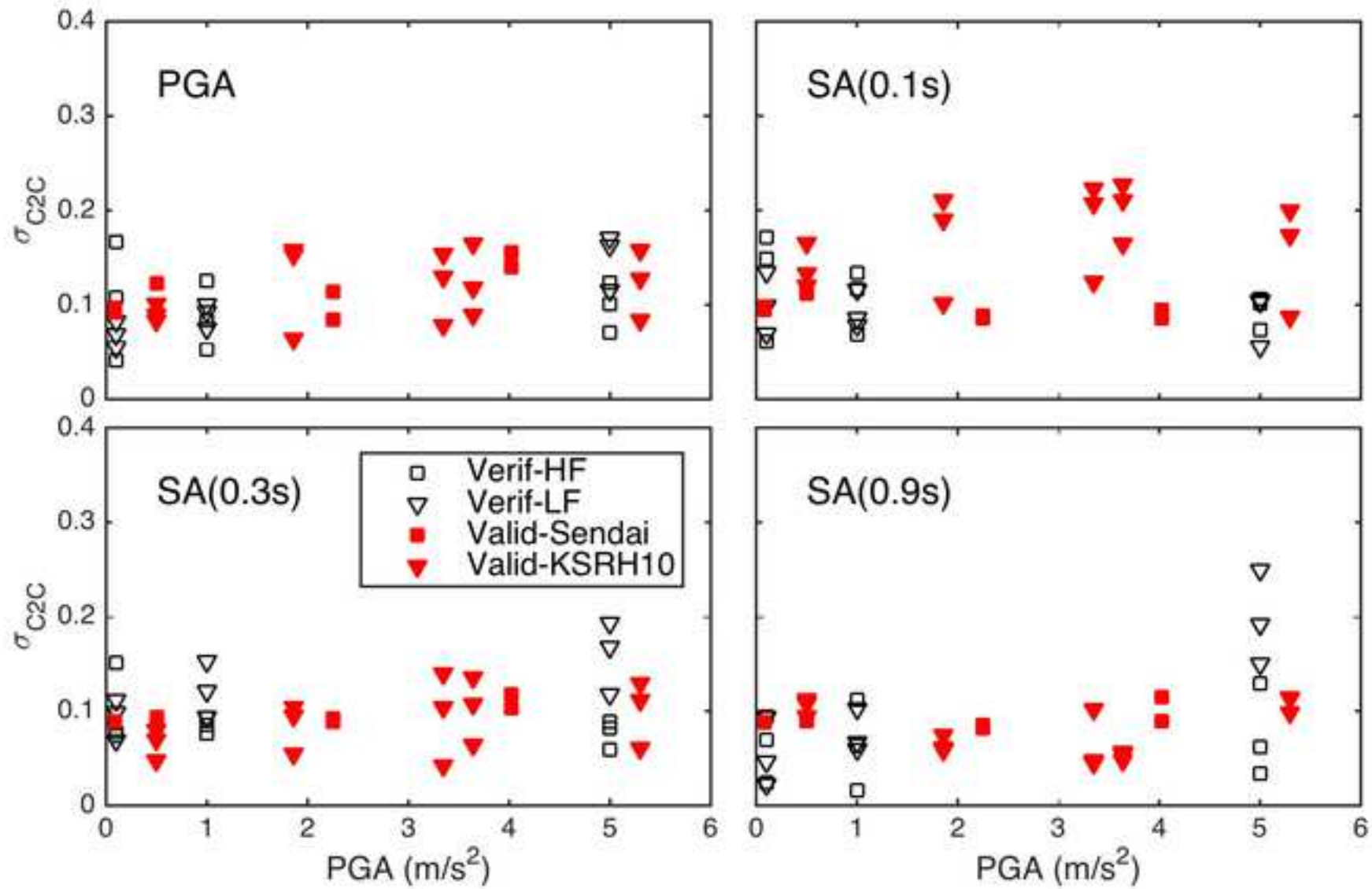


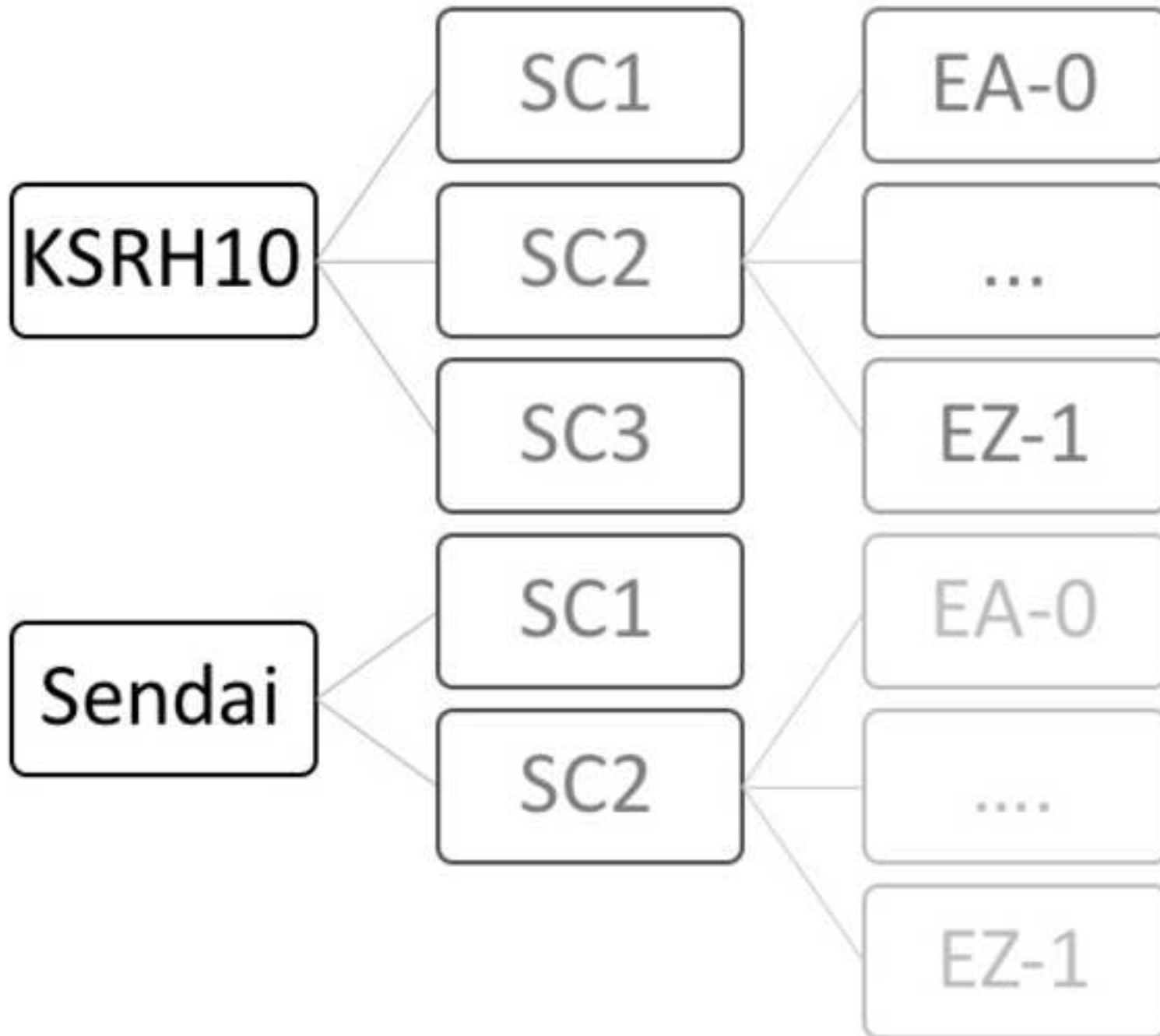
Figure 5

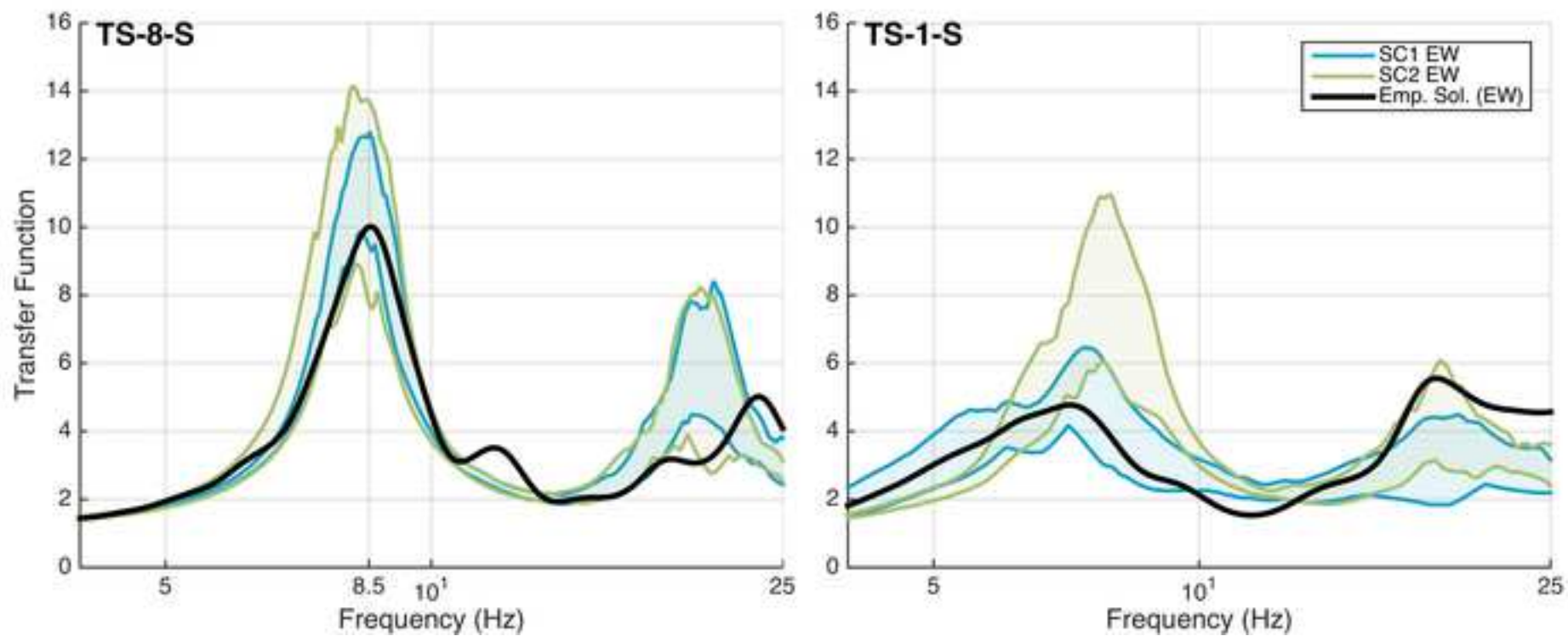


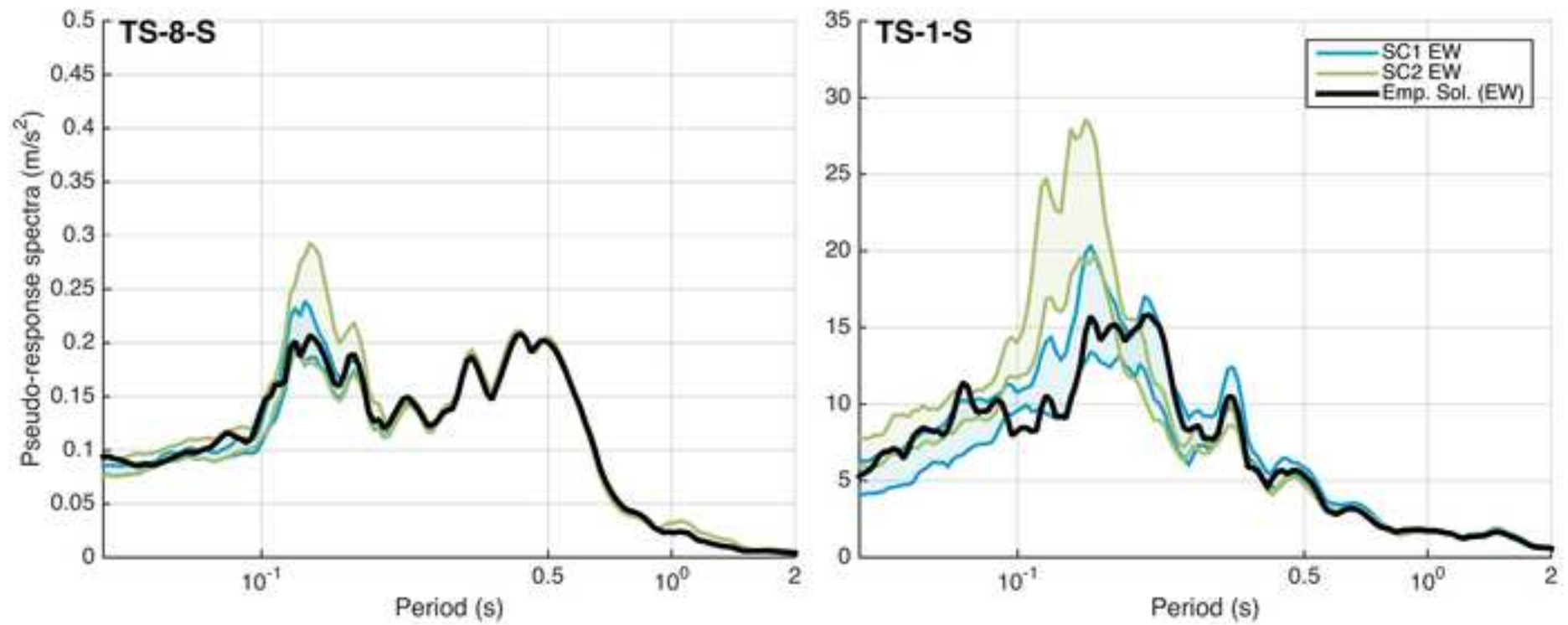


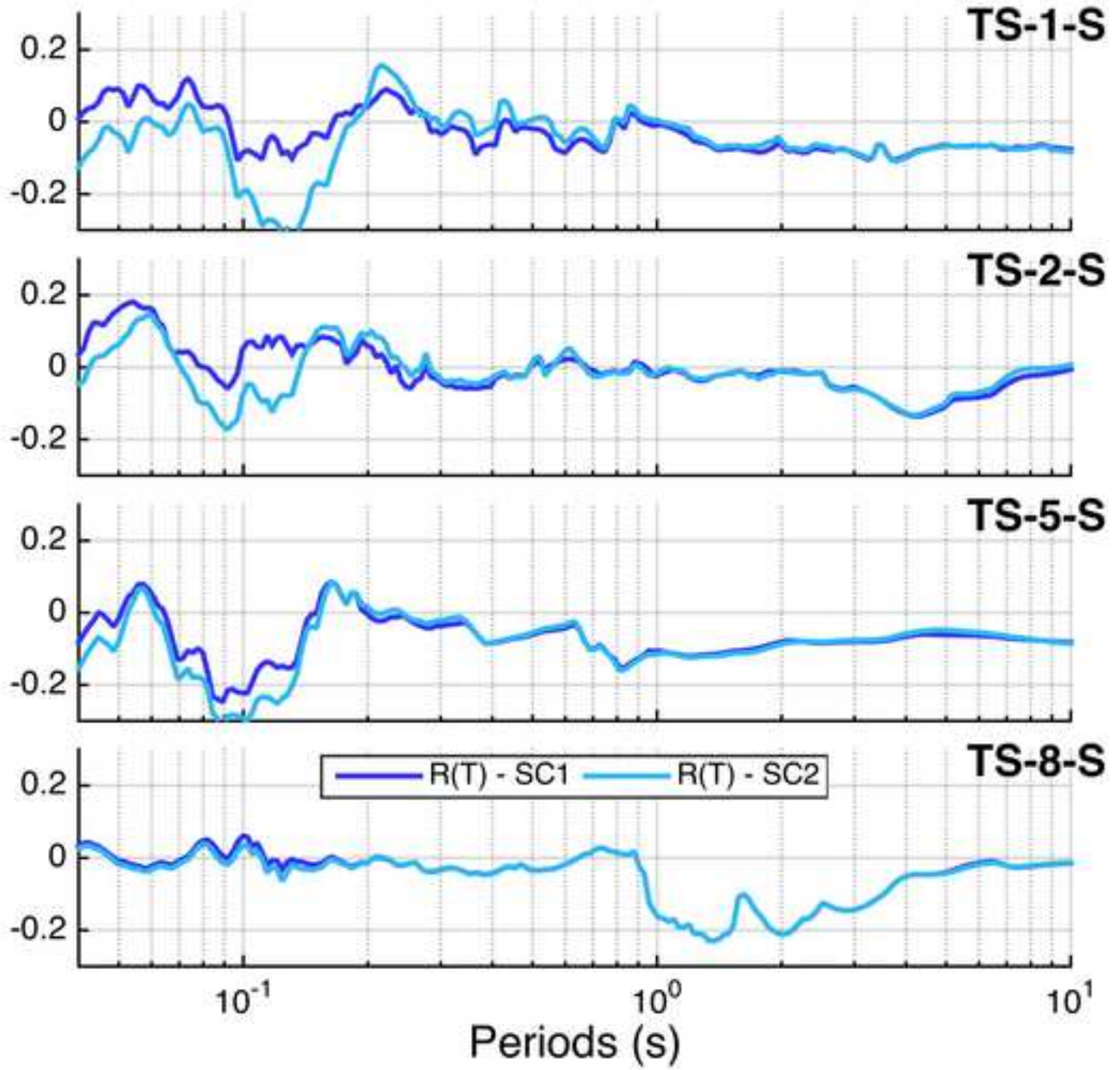


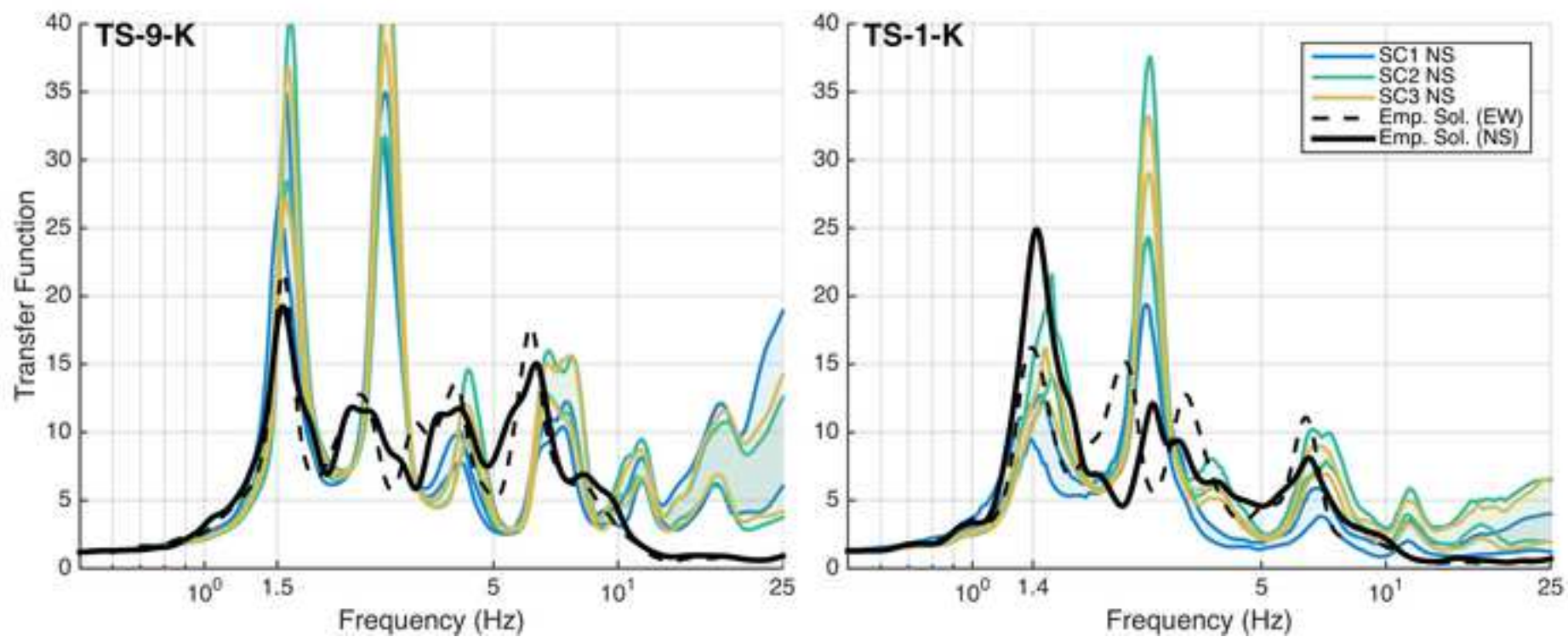


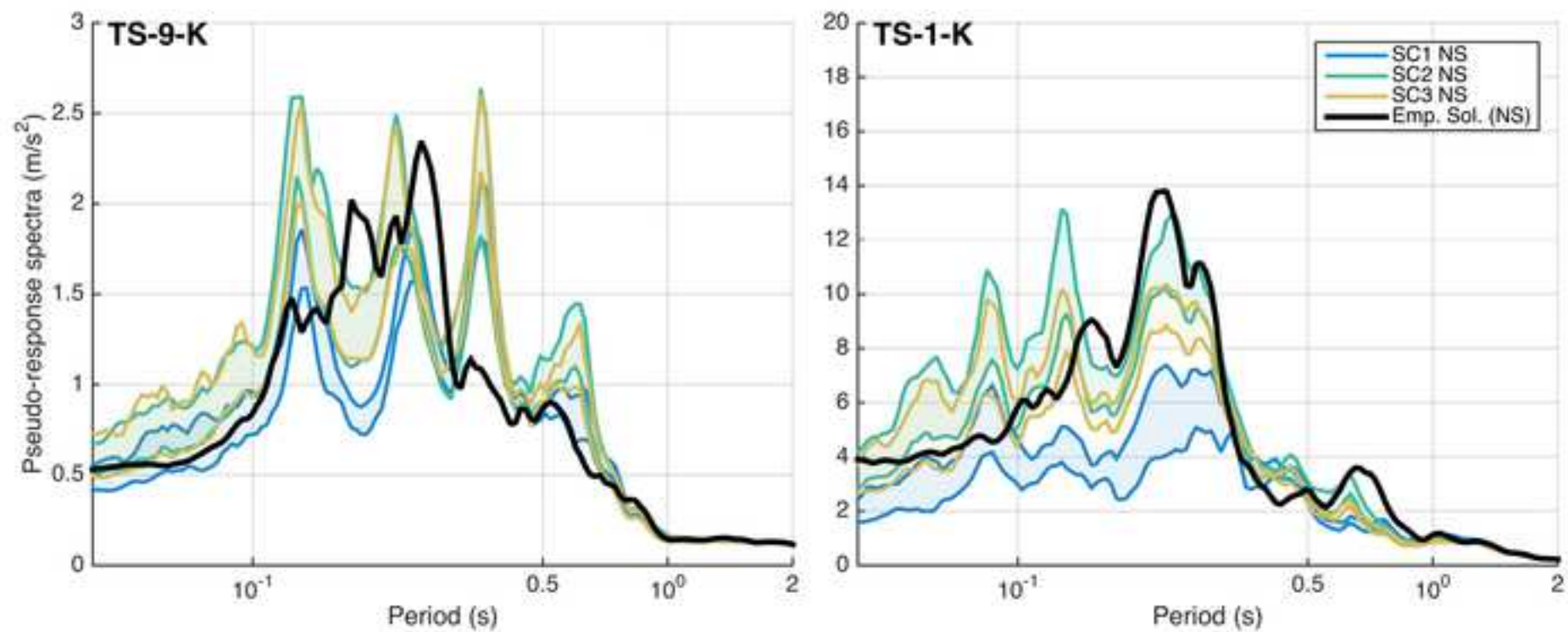


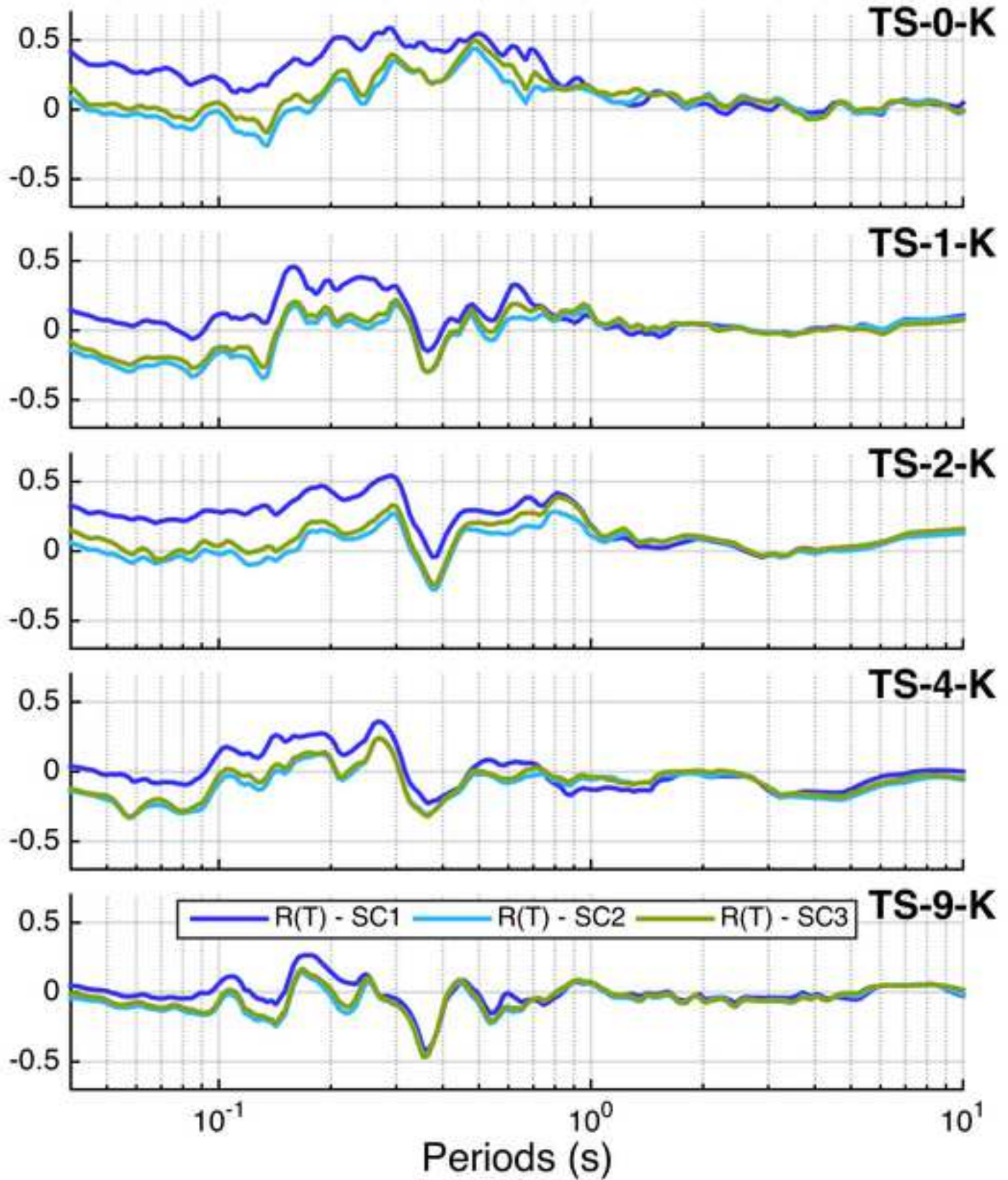












PRENOLIN: international benchmark on 1D nonlinear site response analysis – Validation phase exercise

Julie Régnier, Luis-Fabian Bonilla, Pierre-Yves Bard, Etienne Bertrand, Fabrice Hollender, Hiroshi Kawase, Deborah Sicilia, Pedro Arduino, Angelo Amorosi, Dominiki Asimaki, Daniela Boldini, Long Chen, Anna Chiaradonna, Florent DeMartin, Ahmed Elgamal, Gaetano Falcone, Evelyne Foerster, Sebastiano Foti, Evangelia Garini, George Gazetas, Céline Gélis, Alborz Ghofrani, Amalia Giannakou, Jim Gingery, Nathalie Glinsky, Joseph Harmon, Youssef Hashash, Susumu Iai, Steve Kramer, Stavroula Kontoe, Jozef Kristek, Giuseppe Lanzo, Annamaria di Lernia, Fernando Lopez-Caballero, Marianne Marot, Graeme McAllister, E.Diego Mercerat, Peter Moczo, Silvana Montoya-Noguera, Michael Musgrove, Alex Nieto-Ferro, Alessandro Pagliaroli, Federico Passeri, Aneta Richterova, Suwal Sajana, Maria Paola Santisi d'Avila, Jian Shi, Francesco Silvestri, Mahdi Taiebat, Giuseppe Tropeano, Didrik Vandeputte and Luca Verrucci.

Electronic supplement

The electronic supplement contains elements that provide details on: (1) the codes used during the benchmark with the table of the participants and codes used (Table S1) (2) the analysis performed on the accelerometric data to determine the angle of incidence of seismic waves at KSRH10 and Sendai site (Figure S1). (3) A figure that indicate the location of the soil sampling performed to characterize Sendai and KSRH10 sites (Figure S2 from S5) and (4) Figures on applicability of the numerical methods (Figure S6 and Figure S7).

A detailed presentation of the Polarization analysis for verification of the verticality of the incident propagating input motions is given below:

Since P- and S-waves show a high degree of linear polarization (contrary to Rayleigh waves which are generally elliptically polarized (i.e. Montalbetti and Kanasevich, 1970), the direction of propagation for P-waves is parallel to the particle motion trajectory (hodograph) and perpendicular to the direction of propagation for S-waves. Rayleigh wave particle motion is within the vertical-radial plane, and Love waves are polarized in a horizontal plane perpendicular to the propagation direction. Due to reflections and scattering, a rather a complex particle motion trajectory is observed in real seismograms instead of pure polarization states. The hodograph can therefore be fitted to an ellipsoid in a least-squares sense by means of a covariance analysis (Flinn, 1965; Jurkevics, 1988).

The 3x3 covariance matrix is symmetric, has real non-negative eigenvalues, and its eigenvectors are the principal axes of an ellipsoid that represents the best fit to the data in a least-squares sense. The eigenvector associated with the largest eigenvalue points into the main polarization direction, i.e. the long axis of the ellipsoid. The direction of polarization is calculated from the components (direction cosines) of this eigenvector. The direction can be described by a horizontal azimuth angle ϕ and by the deviation from the vertical direction or apparent incidence angle θ as (Maercklin, 1999):

$$\theta = \arctan\left(\frac{\sqrt{x^2 + y^2}}{z}\right)$$

Eq S1

$$\varphi = \arctan\left(\frac{x}{y}\right)$$

Eq S2

Here, x and y denote the two horizontal components of the principal eigenvector V and z its vertical component.

The choice of the time window length and the frequency bandwidth are subject to trade-offs between resolution and variance (e.g. Wang & Teng, 1997). A short time window and a narrow bandwidth avoid averaging over different phases allow for the resolution of frequency-dependent polarization, whereas a longer window and a wider frequency band yield more stable polarization estimates. Besides that, any filtering before the polarization analysis has to be applied in the same way to all three components and should not distort the signal significantly. In our analysis we chose a time window of 1s and we filtered the data using a low-pass filter with a cut-off frequency of 2Hz.

After the main polarization direction is determined, the degree of linear or planar polarization is evaluated. The rectilinearity RL is a measure of the degree of linear polarization of an event (Flinn, 1965). Montalbetti & Kanasevich (1970) and Kanasevich (1981) define RL as:

$$RL = 1 - \left(\frac{\lambda_2}{\lambda_1}\right)$$

Eq S3

with the two largest eigenvalues λ_1 and λ_2 . With this definition the range of values is between RL = 0 for elliptical or undetermined polarization, and RL = 1 for exactly linear polarization. In **Error! Reference source not found.**, we plotted the incidence in stereographic projection for the two sites (left KSRH10 and right Sendai) of the wave at the borehole station (bottom stereonet) and at the surface (top stereonet).

References

- Aubry, D., Modaressi, A., 1996. GEFDYN, Manuel scientifique. Éc. Cent. Paris LMSS-Mat.
- Bardet, J.P., Ichii, K., Lin, C.H., 2000. EERA: a computer program for equivalent-linear earthquake site response analyses of layered soil deposits. University of Southern California, Department of Civil Engineering.
- Benz, T., 2006. Small strain stiffness of soils and its consequences. Dr. Thesis IGS Univ. Stuttg.
- Benz, T., Vermeer, P.A., Schwab, R., 2009. A small-strain overlay model. Int. J. Numer. Anal. Methods Geomech. 33, 25–44.

- Flinn, E.A., 1965. Signal analysis using rectilinearity and direction of particle motion. *Proc. IEEE* 53, 1874–1876.
- Gerolymos, N., Gazetas, G., 2006. Winkler model for lateral response of rigid caisson foundations in linear soil. *Soil Dyn. Earthq. Eng.* 26, 347–361.
- Gerolymos, N., Gazetas, G., 2005. Constitutive model for 1-D cyclic soil behaviour applied to seismic analysis of layered deposits. *Soils Found.* 45, 147–159.
- Hashash, Y.M.A., Groholski, D.R., Phillips, C.A., Park, D., Musgrove, M., 2012. DEEPSOIL 5.1. User Man. Tutor. 107.
- ITASCA, F., 2011. 7.0: User Manual. Licence Number 213-039-0127-18973. Sapienza—Univ Rome Earth Sci. Dep.
- Jurkevics, A., 1988. Polarization analysis of three-component array data. *Bull. Seismol. Soc. Am.* 78, 1725–1743.
- Kontoe, S., 2006. Development of time integration schemes and advanced boundary conditions for dynamic geotechnical analysis. Imperial College London (University of London).
- Li, W., Assimaki, D., 2010. Site-and motion-dependent parametric uncertainty of site-response analyses in earthquake simulations. *Bull. Seismol. Soc. Am.* 100, 954–968.
- Maercklin, N., 1999. Polarisationsanalyse refraktionsseismischer Daten vom Vulkan Merapi, Indonesien.
- Matasović, N., Ordóñez, G., 2007. D-MOD2000. GeoMotions, LLC, Computer Software.
- Matasovic, N., vucetic, M., 1993. Analysis of seismic records obtained on november 24, 1987 at the Wildlife liquefaction array. University of California, Los Angeles.
- Mercerat, E.D., Glinsky, N., 2015. A nodal discontinuous Galerkin method for non-linear soil dynamics. 6th Int. Conf. Earthq. Geotech. Eng.
- Modaresi, H., Foerster, E., 2000. CyberQuake. User's Man. BRGM Fr.
- Montalbetti, J.F., Kanasewich, E.R., 1970. Enhancement of teleseismic body phases with a polarization filter. *Geophys. J. Int.* 21, 119–129.
- Potts, D.M., Zdravkovic, L., 1999. Finite element analysis in geotechnical engineering: theory. Imperial College of Science, Technology and Medicine. Thomas Telford Publishing, Thomas Telford Ltd, ISBN 0-7277-2783-4.
- Santisi d'Avila, M.P., Lenti, L., Semblat, J.-F., 2012. Modelling strong seismic ground motion: three-dimensional loading path versus wavefield polarization. *Geophys. J. Int.* 190, 1607–1624.
- Santisi d'Avila, M.P., Semblat, J.-F., 2014. Nonlinear seismic response for the 2011 Tohoku earthquake: borehole records versus one-directional three-component propagation models. *Geophys. J. Int.* 197, 566–580.

Santisi d'Avila, M.P., Semblat, J.-F., Lenti, L., 2013. Strong Ground Motion in the 2011 Tohoku Earthquake: A One-Directional Three-Component Modeling. *Bull. Seismol. Soc. Am.* 103, 1394–1410.

Shi, J., Asimaki, D., 2017. From Stiffness to Strength: Formulation and Validation of a Hybrid Hyperbolic Nonlinear Soil Model for Site-Response Analyses. *Bull. Seismol. Soc. Am.*

Susumu Iai, T.K., Yoasuo Matsunaga, 1990. Strain space plasticity model for cyclic mobility (No. 4). port and harbour reasearch insitute.

Taborda, D.M., Zdravkovic, L., Kontoe, L., Potts, D.M., 2010. Alternative formulations for cyclic nonlinear models: parametric study and comparative analyses. *Numer. Methods Geotech. Eng. NUMGE 2010 Benz Nord*. Eds CRC Press, 423–428.

Tropeano, G., Chiaradonna, A., d'onofrio, A., Silvestri, F., 2016. An innovative computer code for 1D seismic response analysis including shear strength of soils. 101680geotSIP 15-P-017.

List of table caption

Table S1: List of the teams that participate to the PRENOLIN benchmark with references on the code used.

List of Figure caption

Figure S1: Stereonet of the incident waves recorded at KSRH10 (left graphs) and Sendai (right graphs) at the surface sensor (upper graphs) and at the borehole station (bottom graphs).

Figure S2: Localization of the soil sampling at Sendai site 1/2

Figure S 3: Localization of the soil sampling at Sendai site 2/2

Figure S4: Localization of the soil sampling at KSRH10 site 1/2

Figure S5: Localization of the soil sampling at KSRH10 site 2/2

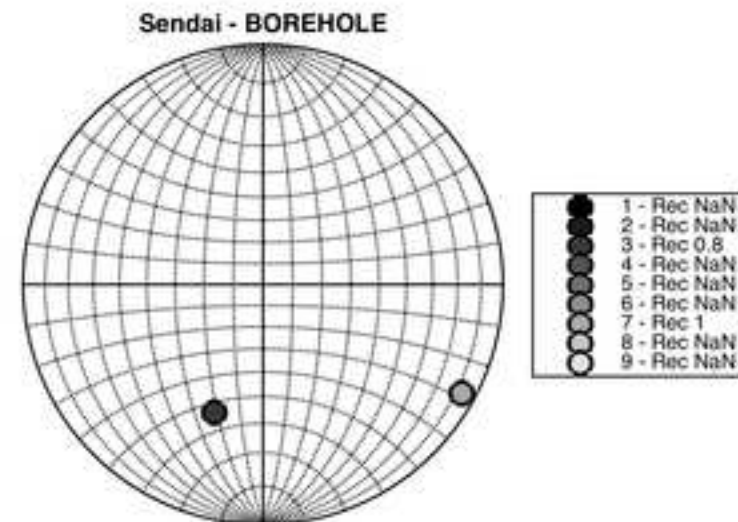
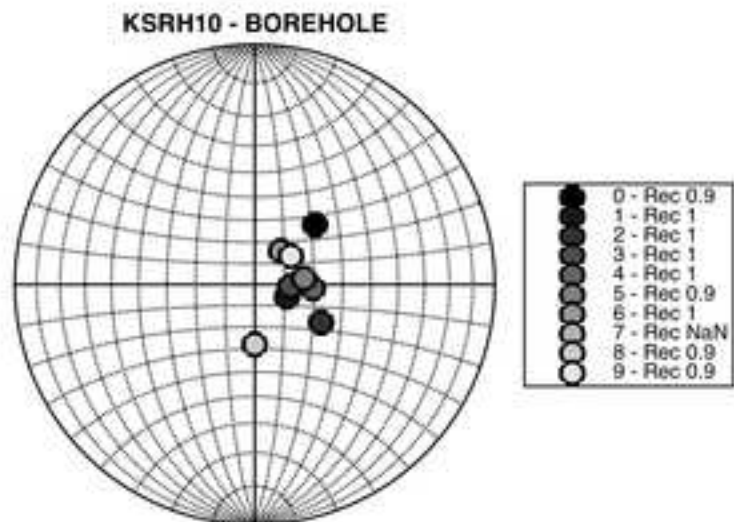
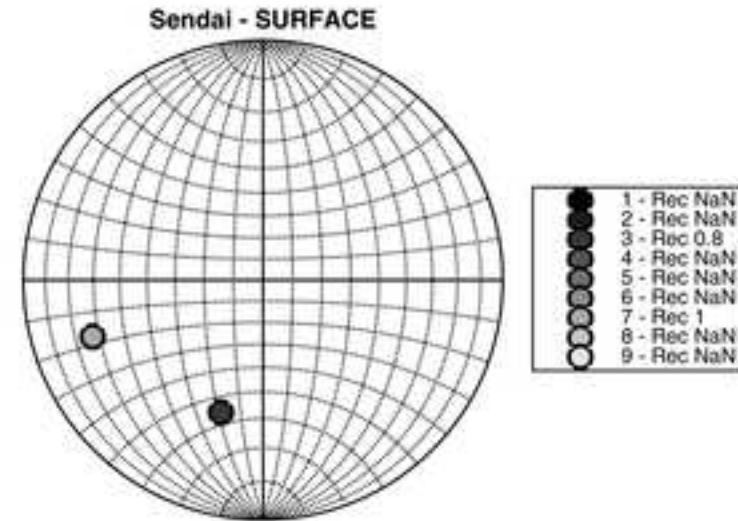
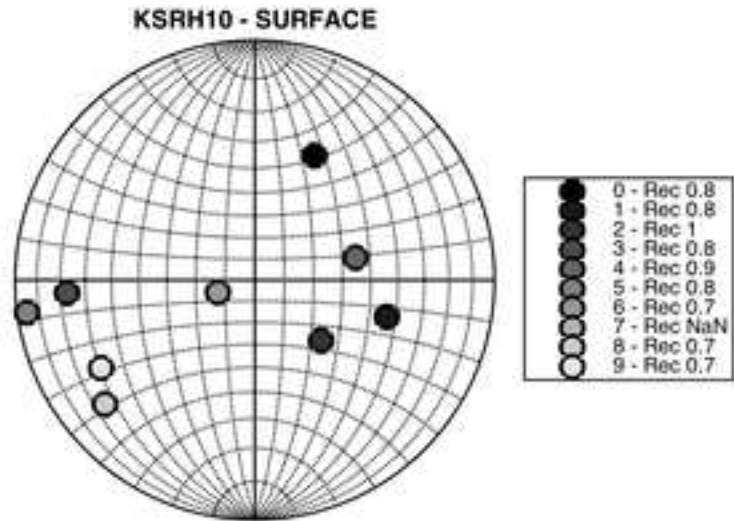
Figure S6: Comparison of the surface response spectra of the EW component of the input motion TS-1-S recorded at Sendai with the computed ones using SC2. The results of the computations using 1 component of motion and using the three components of motions simultaneously are individually plotted. The rest of the simulations are plotted using the average ± 1 standard deviation.

Figure S7: Comparison of the empirical surface to within spectral ratio of the EW component of the input motions TS-1-S and TS-8-S at Sendai with the computed ones. The Equivalent linear methods and the effective stress analysis are individually plotted while the rest of the results are plotted using the average ± 1 standard deviation.

Table S1: List of the teams that participate to the PRENOLIN benchmark with references on the code used.

Team Name	Affiliation	Team Index	Code Name	Code Reference
D. Asimaki & J. Shi	Caltech, Pasadena, California	A 0	SeismoSoil	(Li and Assimaki, 2010; Matasovic and vucetic, 1993; Shi and Asimaki, 2017)
S. Iai	DPRI, Kyoto University, Kyoto, Japan	B 0	FLIP	(Iai, 1990)
S. Kramer	University of Washington, Seattle, Washington	C 0	PSNL	(In development)
E. Foerster	CEA, France	D 0	CYBERQUAKE	(Modaressi and Foerster, 2000)
C. Gelis	IRSN, France	E 0	NOAH-2D	(Iai, 1990)
A. Giannakou	Fugro, Nanterre Cedex, France	F 0	DEEPSOIL 5.1	(Hashash et al., 2012)
G. Gazetas, E. Garini & N. Gerolymos	NTUA, Greece	G 0	NL-DYAS	(Gerolymos and Gazetas, 2006, 2005)5)
J. Gingery & A. Elgamal	UCSD, La Jolla, California	H 0	OPENSEES-UCSD-SOIL-MODEL	See Data and Resources
Y. Hashash & J. Harmon	Univ, Illinois, US	J 0	DEEPSOIL-NL 5.1	(Hashash et al., 2012)
		J 1	DEEPSOIL-EL 5.1	(Hashash et al., 2012)
P. Moczo, J. Kristek & A. Richterova	CUB, Comenius University, Bratislava, Slovakia	K 0	1DFD-NL-IM	
S. Foti & S. Kontoe	Politecnico di Torino, Torino, Italy and Imperial College, United Kingdom	L 1	ICFEP	(Kontoe, 2006; Potts and Zdravkovic, 1999; Taborda et al., 2010)
		L 2	DEEPSOIL-NL 5.1	(Hashash et al., 2012)
G. Lanzo, S. Suwal, A. Pagliaroli & L. Verrucci	University of Rome La Sapienza and University of Chieti-Pescara, Italy	M 0	FLAC_7,00	(ITASCA, 2011)
		M 1	DMOD2000	(Matasović and Ordóñez, 2007)
		M 2	DEEPSOIL 5.1	(Hashash et al., 2012)
F. Lopez-Caballero & S. Montoya-Noguera	CentraleSupélec, Paris-Saclay University, Châtenay-Malabry, France	N 0	GEFDyn	(Aubry and Modaressi, 1996)
F. De-Martin	BRGM, France	Q 0	EPISPEC1D	(Iai, 1990) See Data and Resources
B. Jeremić, F. Pisanò & K. Watanabe	UCD, LBLN, TU Delft & Shimizu Corp	R 0	real ESSI Simulator	See Data and Resources
A. Nieto-Ferro, D. Vandeputte	EDF, Paris & Aix-en-Provence, France	S 0	ASTER	See Data and Resources
A. Chiaradonna, F. Silvestri & G. Tropeano	UNICA and University of Naples, Naples, Italy	T 0	SCOSSA_1,2	(Tropeano et al., 2016)
		T 1	STRATA	
M.P. Santisi d'Avila	University of Nice Sophia Antipolis, Nice, France	U 0	SWAP_3C	(Santisi d'Avila et al., 2012, 2013; Santisi d'Avila and Semblat, 2014)
D. Mercerat and N. Glinsky	CEREMA, France	Y 0	DGNL	(Mercerat and Glinsky, 2015)
D. Boldini, A. Amorosi, A. di Lernia & G. Falcone	University of Bologna, Sapienza University of Rome, and Politecnico di Bari, Italy	Z 0	EERA	(Bardet et al., 2000)
		Z 1	PLAXIS	(Benz, 2006; Benz et al., 2009)
M. Taiebat & P. Arduino	UBC, British Columbia, Canada and University of Washington, Seattle, Washington	W 0	Opensees	See Data and Resources

DPRI, Disaster Prevention Research Institute; CEA, Commissariat à l'Energie Atomique; IRSN, Institut de Radioprotection et de Sécurité Nucléaire; NTUA, National Technical University of Athens; UCSD, University of California, San Diego; ECP, Ecole Centrale Paris-Supelec; BRGM, Bureau De Recherches Géologiques et Minières; UCD, University of California, Davis; LBLN, Lawrence Berkeley National Laboratory; EDF, Electricité de France; UNICA, University of Cagliari; CEREMA, centre d'études et d'expertise sur les risques, l'environnement, la mobilité et l'aménagement; UBC, University of British Columbia.



Measurements quantities (Kushiro)

Depth (m)	Assumption stratum Soil property classification	Drilling Pore size(mm)	Tests in-site				Method for obtaining soil samples	Test Labo																																	
			SPT (Method for standard penetration test) Drilling Core(0.5m)	PSSL (Suspension) K0Self Drilling LLT	PSSL (Downhaul)	Physical test				soil			rock																												
						density		water content	particle size distribution	liquid limit and plastic limit	consolidation properties	compression triaxial test CD	compression triaxial test CU	liquefaction test (sand)	triaxial cyclique test (sand)	triaxial cyclique test (clay)	triaxial cyclique test (rock)	unconfined compression test																							
0	Va (kn/a) 																																								
5																			Additional drilling																						
10																																									
15																																									
20																																									
25																																									
30																																									
35																																									
40																																									
45																																									
50																																									
55																																									
60																																									
合計																				55m	49	39	0	48	0	0	9	1	15	16	15	15	1	0	0	3	0	0	3	1	1

